

BRAIN-be

**Belgian Research Action
through Interdisciplinary
Networks**

2012-2017

CCSOM

Constraining CMEs and shocks by Observations and Modelling

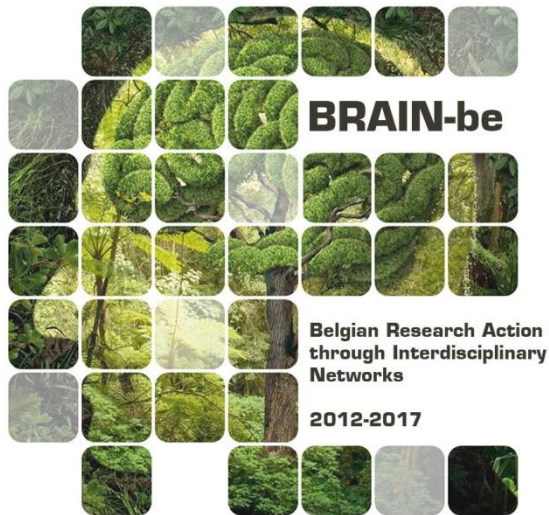
Dr. Jasmina Magdalenic, SIDC – Royal Observatory of Belgium, Belgium

Prof. Dr. Stefaan Poedts, CmPA – KULeuven, Belgium

Dr. Jens Pomoell, University of Helsinki (Finland) – international partner

Dr. Manuela Temmer, University of Graz – international partner

Axis 2: Geosystems, universe and climate



NETWORK PROJECT

CCSOM

Constraining CMEs and shocks by Observations and Modelling

Contract – BR/165/A2/CCSOM

FINAL REPORT

PROMOTORS:

1. Dr. Jasmina Magdalenić, SIDC – Royal Observatory of Belgium, Belgium
2. Prof. Dr. Stefaan Poedts, CmPA – KULeuven, Belgium
3. Dr. Jens Pomoell, University of Helsinki (Finland) – international partner
4. Dr. Manuela Temmer, University of Graz – international partner

AUTHORS:

1. Dr. Jasmina Magdalenić, Dr Luciano Rodriguez, Evangelia Samara, Immanuel Jebaraj, (SIDC – Royal Observatory of Belgium, Belgium)
2. Prof. Dr. Stefaan Poedts, Dr. Camila Scolini, Anwasha Maharana (CmPA – KULeuven, Belgium)
3. Dr. Jens Pomoell, Dr. Emilia Kilpua, Dr. Eleanna Asvestari (University of Helsinki, Finland) – international partner
4. Dr. Manuela Temmer, Juergen Hinterreiter, Andreas Wagner, Veronika Jercic (University of Graz) – international partner





Published in 2022 by the Belgian Science Policy Office
WTCIII
Simon Bolivarlaan 30 Boulevard Simon Bolivar
B-1000 Brussels
Belgium
Tel: +32 (0)2 238 34 11
<http://www.belspo.be>
<http://www.belspo.be/brain-be>

Contact person: Koen LEFEVER
Tel: +32 (0)2 238 35 51

Neither the Belgian Science Policy Office nor any person acting on behalf of the Belgian Science Policy Office is responsible for the use which might be made of the following information. The authors are responsible for the content.

No part of this publication may be reproduced, stored in a retrieval system, or transmitted in any form or by any means, electronic, mechanical, photocopying, recording, or otherwise, without indicating the reference :

Dr. Jasmina Magdalenic; Prof. Dr. Stefaan Poedts; Dr. Jens Pomoell; Dr. Manuela Temmer. ***Constraining CMEs and shocks by Observations and Modelling***. Final Report. Brussels : Belgian Science Policy Office 2016 – 2021 95p. (BRAIN-be - (Belgian Research Action through Interdisciplinary Networks))

TABLE OF CONTENTS

ABSTRACT	5
1. INTRODUCTION	6
2. STATE OF THE ART AND OBJECTIVES	7
3. METHODOLOGY	9
4. SCIENTIFIC RESULTS AND RECOMMENDATIONS	15
5. DISSEMINATION AND VALORISATION	88
6. PUBLICATIONS	89
7. ACKNOWLEDGEMENTS	95

ABSTRACT

During the last decades our dependence on technological assets is increasing, inducing the need for reliable space weather forecasting. The fast solar wind, coronal mass ejections (CMEs) and CME-driven shock waves are the main drivers of the space weather at Earth and the cause of the geomagnetic storms. The forecasting arrival of these disturbances, and their geomagnetic impact strongly relies on the MHD models such as EUHFORIA. The CCSOM project aimed to improve our knowledge on the space weather related phenomena and accuracy of their forecasting with EUHFORIA model. The studies of solar wind modelling with EUHFORIA showed that the main source of modelling inaccuracy arises from the EUHFORIA's coronal model and from the different morphological characteristics of the coronal holes that sourced the fast solar wind. We have implemented and tested different CME models in EUHFORIA. In particular, the spheromak CME model that contains the magnetic field, which allowed us to model the arrival of the magnetic structure of the CME at Earth. The studies performed in the framework of the CCSOM project significantly improved the accuracy of CME and solar wind modelling with EUHFORIA, and paved the way to other presently ongoing project that aim to continue improvements of the EUHFORIA model.

Keywords: Sun, solar wind, CMEs, shock waves, space weather, EUHFORIA

1. INTRODUCTION

The aim of the CCSOM project was to improve the modelling of CMEs and the background solar wind with the recently developed a full three-dimensional (3D) magnetohydrodynamic (MHD) model EUHFORIA (EUropean Heliospheric FORecasting Information Asset; Pomoell & Poedts, 2018). Every model that is used not only for the scientific but also for the operational purposes needs to be validated after its significant update or change. Therefore, dynamically developing models, or newly developed models that aim to become as realistic as possible, need to be constantly validated. The CCSOM project aimed to the implementation of different coronal models in EUHFORIA, the CMEs containing magnetic field, and to the model validation. The project resulted in a significantly improved and fully validated EUHFORIA model of solar wind, CMEs and CME-driven shock waves.

2. STATE OF THE ART AND OBJECTIVES

The Sun is the closest star to Earth and therefore only star where many astrophysical processes can be studied in details. We constantly observe the Sun and its surface activity and immediate consequences in interplanetary space. The outermost layer of the solar atmosphere, the corona, is a dynamic and complex plasma system in which the most energetic transient processes in the solar system, flares and coronal mass ejections (CMEs) occur. CMEs are large amounts of plasma and magnetic flux expelled from the Sun into the interplanetary medium. CMEs play the main role in creating disturbed space weather conditions (geoeffective CMEs) by driving geomagnetic storms that may disrupt satellite operations, navigation systems, and radio communications (e.g. Bothmer & Daglis (eds.) 2006). Studies of CMEs, in particular of their initiation and propagation, are therefore a key topic in solar physics and space weather research.

A CME is geoeffective if it arrives at the Earth and its magnetic field has a particular configuration. Namely, the north-south component B_z of the interplanetary magnetic field needs to be oriented southward, strong and long-lasting (e.g. Burton et al. 1975). In recent years, there has been a significant progress in improving the accuracy of the CME arrival predictions (e. g. Millward et al. 2013) but predicting the B_z configuration still remains to be difficult. The problem of B_z prediction is very complex as the magnetic configuration of a CME close to the Sun is poorly known, and its evolution on the way from the Sun to the Earth depends on several factors, including the interaction of the CME with the background solar wind e.g., deceleration/acceleration, deformation, erosion, shock wave formation. The resulting configuration at 1 AU may include the ICME (interplanetary CME), the shock driven by the ICME, and the sheath region between them (e.g. Schwenn 2006). The simplest ICME configuration is that of a magnetic flux rope. The geoeffective southward B_z may be contained both inside the ICME and inside the sheath. In the latter case, the strength of the B_z component crucially depends on the related shock parameters, which, in turn, depend on the ICME interaction with the background solar wind. Another degree of complexity is added by the intrinsically three-dimensional structure of CMEs and ICMEs.

Our current knowledge on the CME-ICME structure is poorly constrained by observations. The remote-sensing instruments allow tracking the propagation of CMEs in white light (from the corona up to more than 1 AU, see e.g. Möstl et al. 2009), but these observations do not provide information on their magnetic field. From the white light observations, it is often even difficult to distinguish between the CME and the CME-driven shock wave. The in situ instruments provide one or several one-dimensional cuts through the CME volume, which is insufficient to derive its full three-dimensional structure (Jacobs et al. 2009). Therefore, we need to rely on models, which are presently not realistic enough to predict the magnetic field configuration of ICMEs at the Earth. In addition, the routinely available in situ measurements were up to recently available only at 1 AU, which therefore did not allow us forecast with a sufficient lead time (for satellite operators etc.).

At the time of the project writing, the state-of-the-art model of the solar wind and ICME propagation in the inner heliosphere was ENLIL (Odstrčil et al. 2005). At the same time, EUHFORIA (Pomoell & Poedts, 2018) was just recently developed model which also aimed to

become the state-of-the-art model. The background solar wind in ENLIL and EUHFORIA is similarly defined. It is data-driven and described on the base of the coronal field derived from extrapolation of observed photospheric synoptic magnetograms, and empirical relations determining the wind speed, its density, and temperature (Riley et al. 2015). In ENLIL, the CME was almost exclusively a plasma “cone” without magnetic field structure. The concept of the flux rope insertion at the inner boundary of the heliospheric domain (0.1 AU) planned in the framework of the CCSOM project was promising the simulation of a number of physical effects: the ICME and its driven shock being separated by the sheath (ENLIL simulates them together as a single pressure pulse), internal magnetic configuration of the ICME and the sheath, evolution of the ICME magnetic field on the way from the solar corona to 1 AU, including deformation and erosion (e.g. Ruffenach et al. 2012). The starting advantage of the EUHFORIA model in comparison with ENLIL is its large flexibility, and possibility to easily replace different parts of the model which makes the model adaptation and improvements rather straight forward.

The overarching science question that was addressed in the CCSOM project is: how do CMEs propagate and evolve through the inner heliosphere?

To address this question, the main specific objectives of the project were:

- 1) to simulate the propagation of flux rope CME-ICME structures in realistic background solar wind conditions, with the resulting model exceeding the current state of the art, and
- 2) to compare the results of the obtained model with observations of a number of events of different types.

3. METHODOLOGY

The primary focus of the CCSOM project were improvements of the EUHFORIA model and data constrained modelling, therefore we first present the main information about the model. Additionally to the methods that were foreseen in the project description (described in this Section), we also developed and employed some new methods, that are described in the Section 4, together with the study for which they were developed.

3.1 EUHFORIA (European Heliospheric Forecasting Information Asset) model

Majority of presently available operational, physics-based solar wind and CME models lack some key characteristics in order to provide accurate forecasts of the coronal and heliospheric conditions. In particular, none of the presently available models (e.g. WSA-ENLIL etc.) is able to predict the magnetic structure of CMEs, and accordingly the strength of the geomagnetic impact, the stand-off distance of the associated shock wave, or the properties of solar energetic particle (SEP) events. In order to address this growing need for accurate space weather predictions, a new model named EUHFORIA was recently developed by KU Leuven and University of Helsinki.

EUHFORIA is a coupled model consisting of three essential parts: a coronal model, a heliospheric model and an eruption model. The main purpose of the *coronal model* is to provide the inner boundary conditions necessary for the initiation of the heliospheric part. In the default EUHFORIA set-up (EUHFORIA_0), the same as in Pomoell & Poedts, (2018), the MHD wind parameters at 0.1 AU are provided with 2 deg resolution by the semi-empirical Wang-Sheeley-Argé (WSA; Arge et al. 2003, 2004) model, in combination with the potential field source surface (PFSS) model (Altschuler & Newkirk 1969; Wiegmann et al. 2017) and the Schatten current sheet (SCS) model (Schatten et al. 1969). Using these initial boundary conditions in an MHD relaxation procedure, we obtain a steady heliospheric background wind.

The task of the *heliospheric model* is to compute the time-dependent evolution of the plasma from the inner boundary of EUHFORIA to the distance of typically up to 2 AU (in order to include the orbit of Mars within the domain). This is done by numerically solving the MHD equations with the boundary conditions provided by the coronal model. In the default set up of EUHFORIA the CMEs are injected at the interface radius determined by the eruption model. Thus, from 0.1 AU onwards, EUHFORIA provides a time-dependent, three-dimensional model of the heliosphere that self-consistently captures effects such as solar wind stream interactions, shock formation and the interaction of CMEs with structures in the solar wind. An important feature of EUHFORIA is its flexibility, namely the three models are fully autonomous and each part of EUHFORIA can be easily substituted with other model in a modular way, e.g. it is possible to replace the coronal model or the eruption model. This characteristic of EUHFORIA is particularly important and it was strongly employed in this project.

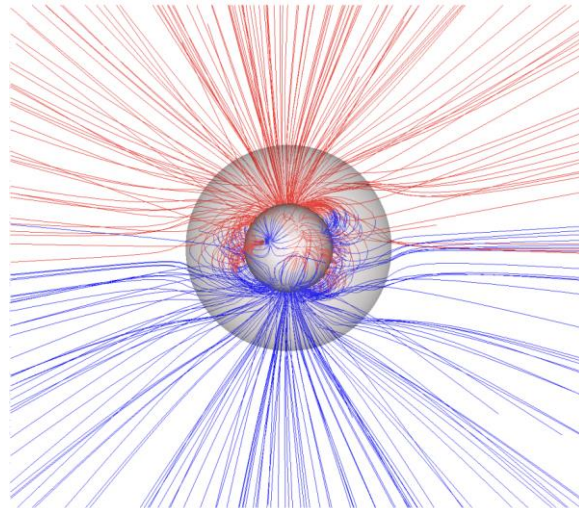


Figure 1

The coronal magnetic field as reconstructed by the PFSS and the SCS in EUHFORIA with a GONG ADAPT magnetogram on 2018-05-05 at 00:00 UT. Red and blue colors indicate the opposite magnetic field polarity between the two solar hemispheres. The inner grey sphere depicts the solar photosphere while the outer transparent sphere marks the radius of $2.3 R_{\odot}$, beyond which the SCS starts taking place (adapted from Samara et al., 2021).

After the magnetogram insertion EUHFORIA employs the PFSS (potential field source surface model; Altschuler & Newkirk 1969; Wiegmann et al. 2017) model until the height of $2.6 R_{\odot}$, to reconstruct a current-free magnetic field (Fig. 1a). Starting from the height of $2.3 R_{\odot}$ onwards, the SCS model (Schatten current sheet; Schatten et al. 1969) is used (Fig. 1a). This model starts before the end of the PFSS domain in order to reduce possible kinks in the magnetic field lines due to incompatible boundary conditions between the two models (see e.g. McGregor et al. 2011; Asvestari et al. 2019). The purpose of the SCS is to create an approximately uniform coronal magnetic field away from the Sun, maintaining a thin structure for the heliospheric current sheet (HCS). A more uniform magnetic field is necessary in order to obtain a better agreement between the model and the observations.

The initial version of the CME model in EUHFORIA consists of a hydrodynamic cone-like model whose parameters (width, speed, direction) were constrained from fitting the cone to coronal imaging observations of CMEs (see Section 3.3 and Fig.3).

Initial tests with EUHFORIA_0 (performed before this project) indicated that the model is producing results comparable with the state-of-the-art ENLIL model. However, before the CCSOM project EUHFORIA model was not yet ready for the frequent runs for the scientific or operational forecasting purposes. The improvements and modifications of EUHFORIA, as well as the validation of the model were planned to be performed within the CCSOM project.

3.2 Solar wind

In order to address the accuracy of the solar wind modelling with EUHFORIA we used the error analysis of the simulated evolution of the solar wind speed and density, employing the simple methods as e.g., cross-correlation, arithmetic mean and standard errors. Additionally, to evaluate the performance of the different model runs (i.e., EUHFORIA_0, EUHFORIA_1, each with different

magnetic field input, etc.) we computed the “confusion matrix”. A confusion matrix, contains the four elements TP (true positive: HSS predicted and observed), FP (false positive: HSS predicted but not observed), FN (false negative, no enhanced solar wind predicted but HSS observed), and TN (true negative, no enhanced solar wind predicted and no enhanced solar wind observed). The evaluation of the solar wind modelling with EUHFORIA is presented in Section 4 and in the publication Hinterreiter et al. 2019.

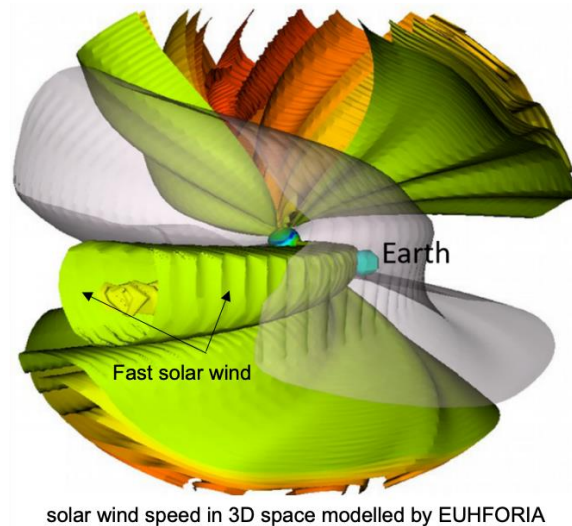


Figure 2

The background solar wind and heliospheric current sheet (grey isosurface) modeled by EUHFORIA and shown in the 3D presentation. The blue sphere presents Earth. The colorful sphere in the middle of the domain shows the solar wind velocities at the inner boundary of EUHFORIA (0.1 AU) while the colorful isosurfaces depict velocities between 530 and 650 km/s (see e.g. Samara et al. 2021).

In the course of the CCSOM project it was found that the available methods do not enable us to estimate, with sufficient accuracy, the performance of EUHFORIA. The reason for the problem in validation of the modelled solar wind characteristics and the in situ observations of the plasma characteristics is a strong variability of the solar wind time series. Therefore, a new method was developed, the so-called dynamic time warping (DTW) (Samara et al. 2022). This method is an alternative way of evaluating the performance of models and, in particular, of quantifying the differences between observed and modelled solar wind time series. The DTW can warp sequences in time, aiming to align them with the minimum cost by using dynamic programming. It can be applied for the evaluation of modelled solar wind time series in two ways. The first calculates the sequence similarity factor, a number that provides a quantification of how good the forecast is compared to an ideal and a nonideal prediction scenario. The second way quantifies the time and amplitude differences between the points that are best matched between the two sequences. As a result, DTW can serve as a hybrid metric between continuous measurements (e.g., the correlation coefficient) and point-by-point comparisons. DTW is a promising technique for the assessment of solar wind profiles, providing at once the most complete evaluation portrait of a model. More details about the method can be found in the Section 4 and Samara et al. (2022).

3.3 Three-dimensional reconstruction of CMEs and their propagation in the inner heliosphere

In order to model CMEs better and to use them as input for EUHFORIA, we employed the state of the art techniques in order to reconstruct the 3D structure of CMEs (Mierla et al. 2010). The coronagraph data available in the past (prior to the launch of STEREO in 2006) provided us with a two-dimensional representation of the CME three-dimensional structure projected onto the plane of the sky. As a consequence, the measured quantities like angular width, height, speed of CMEs are also projected on this plane and therefore, represent lower limits of the true, un-projected CME properties. The projection effects of these main quantities affect in turn the derived quantities like mass and energy. By observing CMEs from multiple viewpoints (STEREO, SOHO) it is possible to derive their true direction of propagation and true speeds in the coronagraph field of view (up to 15 Rs).

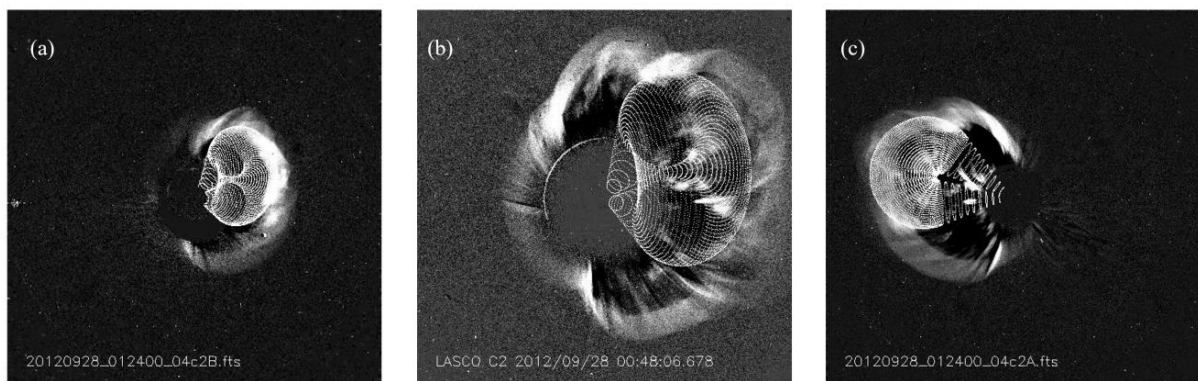


Figure 3

The 3D reconstruction of the CME observed on September 28, 2012. The CME reconstruction was done using forward modelling technique by Thernisien et al. 2006, 2009.

The panels: (a) STEREO B/COR 2; panel (b) SOHO/LASCO C3, and (c) STEREO A/COR 2, are at approximately the same time. The reconstructed flux rope is denoted with the white grid crossant (adapted from Jebaraj et al. 2020).

To derive the position of a feature in 3D from two view directions (either from two STEREO spacecraft, or from one STEREO spacecraft and one Earth direction (PROBA2 or SOHO)) we will use different methods (e.g. Mierla et al. 2009). The most common technique is tie-pointing and triangulation (e.g. Inhester, 2006).

The second method used for 3D reconstruction is forward modelling (Thernisien et al. 2006, 2009, see Fig.3). This method can reproduce the large-scale structure of a CME by using a magnetic flux rope-like model. It consists of a tubular section forming the main body of the structure attached to two cones that correspond to the "legs" of the CME. A similar forward model (using an ellipsoid) can be used to reproduce the 3D structure of a CME-driven shock (e.g. Kwon et al. 2014). Finally, a third technique is known as polarized ratio. It uses the properties of Thomson scattered light, which depends on the scattering angle between the direction of the incident light and the direction to the observer. The result is the position of the feature with respect to the plane of the sky.

For some events we employed also the observations by Heliospheric Imagers (HI) onboard the NASA STEREO mission to track the propagation of density structures i.e. CMEs in the heliosphere. The

trajectory of bright elements in the HI field of view carries information on the 3-dimensional propagation path and speed of solar wind transients. However, the one-dimensional time-elongation profiles of solar wind transients need to be converted into 3D coordinates. Three geometrical models are generally used, based on different assumptions on the shape of the transient. In the fixed-phi model (e.g. Rouillard et al. 2008), the solar wind transient is assumed to be a point-like source. The harmonic mean model (e.g. Lugaz, 2010) assumes the shape of a circle attached to the center of the Sun, The self-similar expansion model (Davies et al. 2012) assumes the solar wind transient to be a circle that is not attached to the Sun but is limited by a constant angular width in solar longitude.

3.4 Radio bursts associated with the eruptive events

Together with the studies of solar wind and CMEs we also studied the CME-driven shock waves employing the multiwavelength observations with the main focus to radio observations. While the white light coronagraph observations can give a good indication on the geometry of the shock and its driver, it is not always easy to identify a shock wave in a coronagraph image. The only way to exactly locate the 3D position of (a part of) the shock wave in the inner heliosphere employing observations is by using the radio signatures of the shock wave, so called type II radio bursts (Fig. 4) and a novel radio triangulation method (e.g. Magdalenic et al. 2014, Jebaraj et al. 2020, 2021). Type II radio bursts are observed in dynamic spectrum as a slowly drifting emission lanes, usually showing fundamental and harmonic bands (Fig. 4). Assuming the coronal electron density model, the drift rate of the type II radio bursts can provide us the estimate of the shock wave velocity (see e.g. Magdalenic et al. 2008).

In the framework of the CCSOM project we employed the direction-finding or goniopolarimetric observations, from WIND and the twin STEREO spacecraft. The direction of arrival of an incoming electromagnetic radio wave, its flux, and its polarization were derived from these observations. Because of the different types of antenna on these spacecraft, we have used different direction-finding methods. For the WIND observations, the standard spinning demodulation method (Manning & Fainberg, 1980) was applied. For the STEREO observations, we used goniopolarimetric inversion of a signal measured on nonorthogonal antennas using the singular value decomposition (SVD) technique (Krupar et al. 2012). From the direction-finding data we can retrieve the wave vector directions, which allow estimation of the radio source location for a case when the radio emission is observed by two or more spacecraft. The position of the radio sources in the 3D space is then considered to be the closest point between the two wave vectors. The shortest distance between wave vectors gives an indication of the source position in the 3D space. The described radio triangulation method was so far applied only very rarely, in most cases to study the propagation path of so called type III radio bursts (e.g. Reiner et al. 2009; Thejappa et al. 2012). In the framework of CCSOM project the radio triangulation method was extensively used in study or propagation of shock waves (e.g. Jebaraj et al. 2020, 2021).

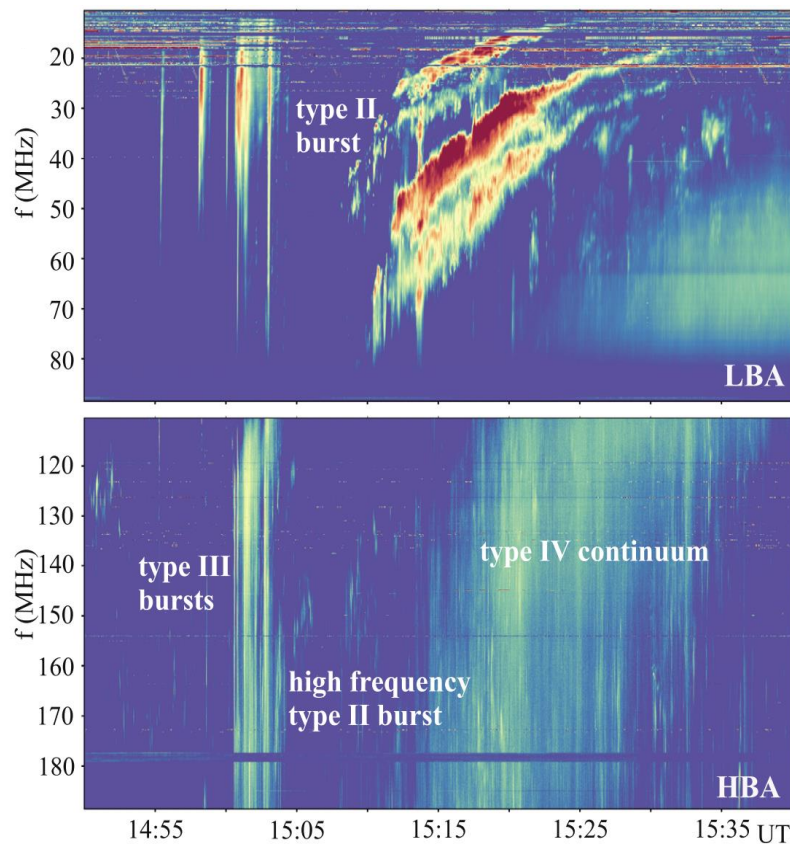


Figure 4

Dynamic radio spectrum i.e. the time/frequency diagram, with color-coded emission intensity, shows the radio event on 2014 August 25 observed by LOFAR radio telescope. Three types of solar radio bursts, type III bursts (radio signature of electrons accelerated along the open field lines), type II burst (radio signature of electrons accelerated at the shock front) and type IV continuum (radio signatures of electrons associated with the CME propagation) are marked. All these types of radio bursts were studied in the framework of the CCSOM project e.g. Palmerio et al. 2019; Jebaraj et al. 2020, 2021; Magdalenic et al. 2020. (Adapted from Magdalenic et al., 2020).

4. SCIENTIFIC RESULTS AND RECOMMENDATIONS

In the framework of CCSOM we have addressed number of objectives, in order to answer to the overarching science question of CCSOM: how do CMEs propagate and evolve through the inner heliosphere? To answer to the science question, we simulated the background solar wind and the propagation of flux rope CME-ICME structures in the realistic solar wind conditions and compared the modelling results with observations. Some of the project results opened new scientific questions, that were then also addressed in the project. The main project results are group in three parts addressing the solar wind, CME-ICMEs and the CME-driven shock waves.

4.1 Modeling of the background solar wind

4.1.1 Assessing the performance of EUHFORIA modeling

This section presents mostly work published in Hinterreiter et al. (2019).

In this study we employed the so-called default setup of EUHFORIA (Section 3 and Pomoell & Poedts, 2018). We describe this set up in details because it was employed in a number of studies in the CCSOM project. In EUHFORIA the solar wind speed depends on several parameters and the functional form of the empirical relation can be selected by the user. In Hinterreiter et al. (2019) we employed the following form:

$$v(f, d) = v_0 + \frac{v_1}{(1 + f)^\alpha} \left[1 - 0.8 \exp(-(d/w)^\beta) \right]^3, \quad (1)$$

where f and d are the flux-tube expansion factor and the angular distance from the footpoint of each open field line to the nearest CH boundary, respectively. The parameters in Eq. 1 are set to $v_0 = 240$ km/s, $v_1 = 675$ km/s, $\alpha = 0.222$, $\beta = 1.25$ and $w = 0.02$ rad. Since the original WSA relation is designed to provide the wind speed at Earth, and as the solar wind continues to accelerate beyond the inner boundary in the heliospheric MHD model, we have additionally subtracted 50 km/s to avoid a systematic overestimate of the wind speed. To compensate for solar rotation, we rotate the solar wind speed map at the inner boundary by 10° . We have also limited the minimum and the maximum solar wind speed at the inner boundary to 275 and 625 km/s, respectively (McGregor et al. 2011). In addition to the wind speed, the remaining MHD variables need to be determined. While the topology of the magnetic field is directly obtained from the SCS model, the magnitude of the solar wind magnetic field is set to be directly proportional to the speed. The plasma number density is given by:

$$n = n_{fsw} (v_{fsw}/v_r)^2, \quad (2)$$

with the number density of the fast solar wind $n_{fsw} = 300 \text{ cm}^{-3}$ (e.g. Venzmer and Bothmer, 2018), the fast solar wind speed $v_{fsw} = 675$ km/s, and v_r coming from the empirical speed definition. We used a constant plasma thermal pressure of 3.3 nPa, at the inner boundary of EUHFORIA, which is in accordance with the fast solar wind temperature of about 0.8 MK. For more details see also Pomoell and Poedts (2018).

The angular resolution of the daily runs in this study was 4° , and 512 grid cells were chosen in the radial direction to cover the 0.1 to 2 AU domain. We used the EUHFORIA daily runs based on the synoptic GONG magnetograms (the start time was about 23:30 UT each day) and do not include

modeling of possible CMEs. The study comprises years 2008 and 2012. Each daily run, based on one magnetogram input, simulates the background solar wind at the heliocentric distance of 1 AU over a total time span of 14 days (± 7 days) covering $\pm 92.4^\circ$ in longitude (gray slice in Fig. 5) with a temporal resolution of ten minutes.

4.1.1.1 Combining individual EUHFORIA runs for obtaining average EUHFORIA time series

The central region of the Sun has the magnetic field information with the smallest projection effects, and it is thus the most reliable part of the magnetogram. In order to combine the individual daily runs of EUHFORIA, which overlap in time, we developed a method containing information with highest weight on the central region of the Sun. The central region is defined as ± 1 day around the central meridian at 0° (schematic drawing in Fig. 5a). The weighting of each curve is done by a Gaussian distribution with the central part receiving the strongest weight (Fig. 5b). This procedure does not include blending of the entire 3D solutions, but only combining the solutions in order to extract a time series at an exact location in space at the Earth. Studies that include CME modeling with EUHFORIA do not combine the runs.

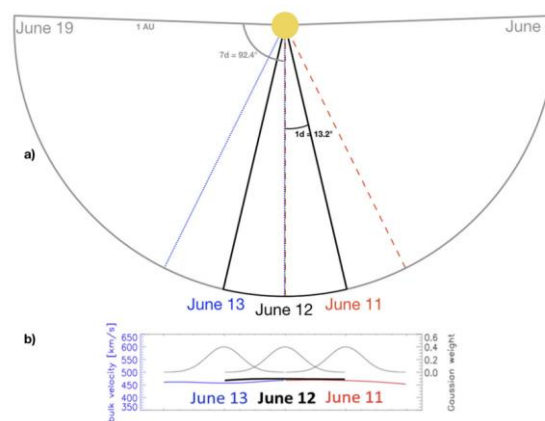


Figure 5

Panel a) Schematic representation of combining EUHFORIA modeling time series for consecutive days. Different colors represent the selected range ($\pm 13.2^\circ$ from the solar central region) for each day. In grey color we indicate the full range ($\pm 92.4^\circ$) provided by EUHFORIA model. Panel b) Gaussian weight used for the model properties shown for three individual days. (Adapted from Hinterreiter et al., 2019).

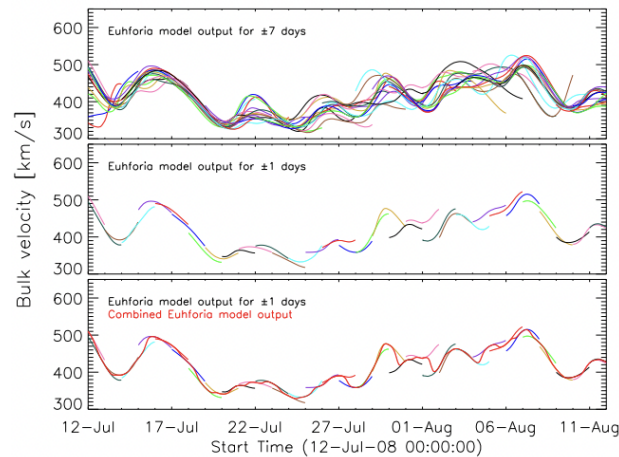


Figure 6

Applying the method for the construction of average EUHFORIA time series. Three panels show the solar wind speed in time interval July to August 2008. The top panel shows full EUHFORIA model output (\pm seven days). The middle panel shows EUHFORIA model output limited to \pm one day and the bottom panel shows model output (different colors for each daily run) and resulting time series (thick red). (Adapted from Hinterreiter et al., 2019).

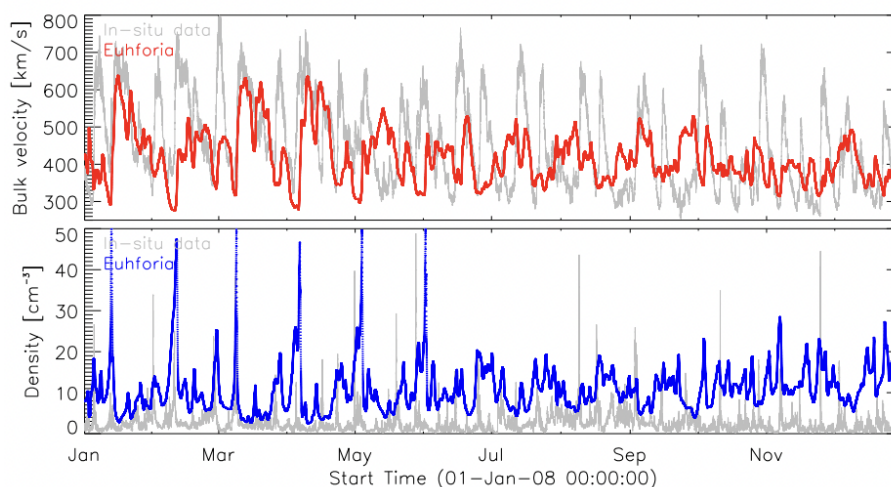
Figure 6 shows how the method was applied. The top panel of Fig. 3 shows the solar wind speed modeled by EUHFORIA for the full model output (\pm seven days). Different colors represent results from 32 daily runs. As can be seen, the simulated solar wind speeds for consecutive days may show significant offsets. In order to obtain a smooth time series we first limit the curves in time to \pm one day (middle panel) and then combine them by using a Gaussian distribution (cf. Figure 2b). The obtained combined time series which is used for the analysis is represented in the bottom panel of Fig. 6 by the thick red curve. We also tested different limits of temporal ranges for the individual runs; e.g. \pm three days, in order to check the quality of the method when combining individual runs. The resulting combined time series are similar, and slightly more smoothed compared to using a time range limit of \pm one day.

We have also evaluated how the combined time series for the modeled solar wind speed are affected when shifting the weighting to a region different from the central part of the Sun. With this, we take into account that compared to the central region of the magnetogram the eastern or western region could influence more strongly the simulated solar wind. Although the results show some differences between the combined time series, for the longer time ranges the general trend is retained.

4.1.1.2 Comparison of observations and modelled solar wind

In order to assess the accuracy of the EUHFORIA's modeling of the background solar wind we chose two intervals of different levels of solar activity. At first, a quiet period during year 2008 is considered, for which only three ICMEs, at the end of the year, were reported in the near Earth solar wind according to the Richardson and Cane ICME list (Richardson and Cane, 2010, see www.srl.caltech.edu/ACE/ASC/DATA/level3/icmetable2.htm). This period is used as a benchmark time interval for the model performance as it quite optimally represents the background solar wind without significant transient perturbations. A second interval considered covers the year 2012, a period with a rather high level of solar activity during which 35 ICMEs are reported (cf. Richardson and

Cane ICME list). In order to evaluate how well EUHFORIA models the background solar wind, we compare the combined time series with the in situ measured plasma speed and density as provided by the Solar Wind Electron, Proton and Alpha Monitor onboard the Advanced Composition Explorer (ACE/SWEPAM: McComas et al. 1998). Figure 7 shows the obtained results. The grey curves represent observed values by ACE, while red and blue curves represent modelled values of the solar wind speed and density, respectively. The statistics presented of the background solar wind modelled with EUHFORIA show on average lower values of the modelled solar wind speed than the in situ measured velocity. On the other hand, the modelled solar wind density is considerably higher than the observed one (in the default setup of EUHFORIA these two parameters are coupled, see Eq. 2). We note that the correlation between modelled and observed values is significantly better in the first half of the year 2008. In the second half of that year, the maximum fast solar wind speeds are lower than observed ones while the minimum values are significantly different, i.e., larger than the observed ones. For the year 2012 the discrepancies between the modelled values and observations are more pronounced. Nevertheless, periods of lower wind speeds during 2012 are rather well reproduced, which might be simply a consequence of a very low wind speed in general obtained for this year. The in situ solar wind speed was also compared to the individual daily runs in order to assess the probability of artificially enhanced or reduced fast wind flows due to combining of the daily runs (Section 2.2). In the two studied years we found only one case of the fast solar wind that was observed in the majority of the daily runs but not in the combined time series (around 22 August 2012). The opposite cases, where the combined time series show significant increase of the solar wind speed that was not modelled in the relevant daily runs, were not found. As a consequence of the, on average, underestimated solar wind speed modelled by EUHFORIA, fast flows arrive with a systematic delay in time. The amount of delay depends on the difference between the modelled and observed wind speed. For example, the fast solar wind with average speed of 600 km/s will need about 2.9 days to arrive at the Earth, while those of about 500 km/s will need about 3.5 days. In this case the induced latency of the modeled solar wind will be about 14 hours. We observe the influence of this effect particularly strongly in the second half of the year 2008 (Fig. 7).



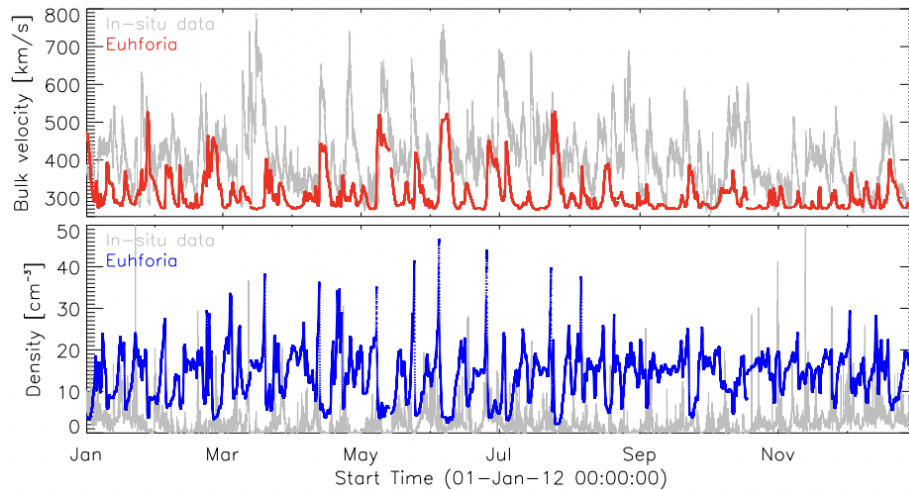


Figure 7

The background solar wind modeling results of EUHFORIA compared with the in situ observations of the solar wind characteristics during the year 2008 (top panel) and year 2012 (bottom panel). Red curve is solar wind velocity and blue is solar wind density. During the first few months the amplitude of the solar wind velocity as modeled by EUHFORIA is similar to observations. During about last 8 months of the year 2008 the solar wind velocity and density are significantly underestimated (Adapted from Hinterreiter et al., 2019).

4.1.1.3 Hit-Miss statistic and evaluation of modeling results

In order to evaluate the accuracy of the EUHFORIA model we performed hit-miss statistics using two different methods for comparing measured and modeled results. We also compare the minimum and maximum phase of the results and give initial results on the effects of different input parameters for the model. In this analysis we focus only on the solar wind velocity.

A) Hit-Miss Statistics by Automatic Peak-Peak Matching Method

To evaluate the model performance, we calculate continuous variables (e.g. root-meansquared error: RMSE) and apply an event-based approach for detecting the maxima (peak finding algorithm) in the solar wind observations. For the event based approach we used an automatic peak-finding algorithm. To be defined as a peak, certain properties (minimum speed is 350 km/s, minimum gradient is 60 km/s, for further details see Reiss et al., 2015) have to be fulfilled. A hit is found if the modeled peak appears within a time window of \pm two days around the measured peak, and a miss if the modeled peak is out of this time window. If the peak is found in the combined time series of EUHFORIA and not in observations, we consider this a false alarm. Since the study also encompasses the year 2012 with a high level of solar activity, it was necessary to isolate intervals with possible ICMEs in the in situ observations. The vertical pink lines in Fig.8 indicate the times of CME occurrences according to the CME list (Richardson and Cane, 2010). For both years under study we obtain a similar result regarding the RMSE, which is about 125 km/s. We detected 39 solar wind peaks in the EUHFORIA combined time series and 43 in the in situ data. Applying the automatic peak-finding algorithm method, we obtain 18 hits, 21 false alarms, and 25 misses. In 2012 the EUHFORIA combined time series shows 21 peaks and 38 are detected in the in situ observations. This corresponds to 14 hits, 7 false alarms, and 24 misses.

As this is a rather poor result we inspect the solar wind profiles in more detail and investigate the reason for the poor performance.

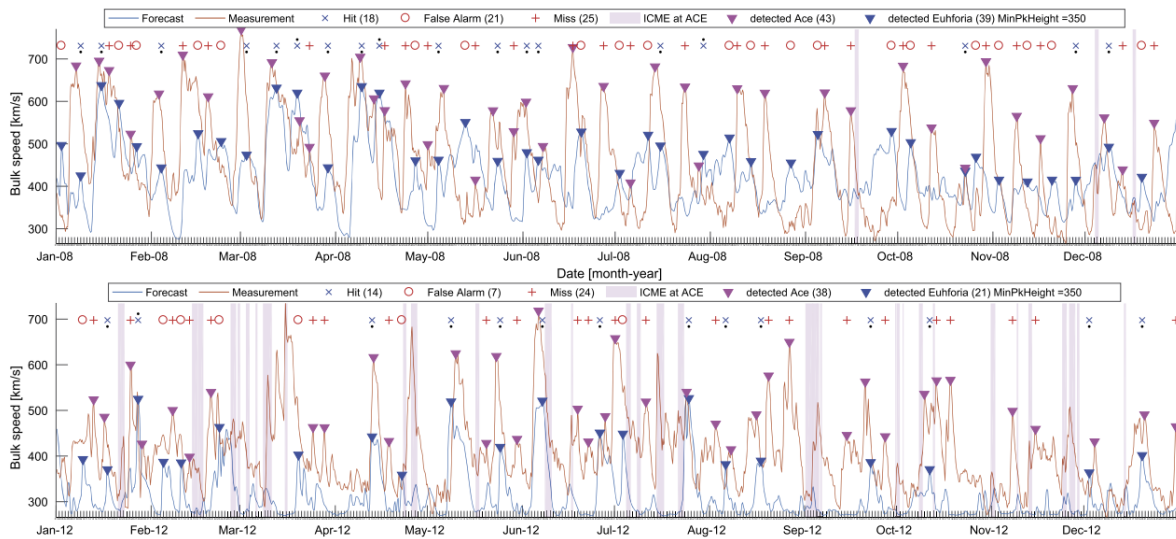


Figure 8

EUHFORIA modeled solar wind bulk velocity (blue) in comparison to in situ measurements (orange) for 2008 (top panel) and 2012 (bottom panel) using a peak-finding algorithm. The pink vertical bars indicate times of CME occurrences according to Richardson and Cane (2010).

B) Hit–Miss Statistics by Manual Peak–Peak Matching Method

The in situ observations frequently show several subsequent local maxima of the solar wind speed associated with a single fast flow generally originating from a large and extended, in latitude or in longitude or both, CH. In such a case the automatic peak-finding algorithm finds several peaks, and it is not possible to make a one-to-one identification with the usually smooth increase of the solar wind speed modeled by EUHFORIA. In order to better understand such long-lasting flows and to unambiguously relate modeled and observed velocity peaks with each other, we checked the development of the CHs on the Sun two days before and three days after the CH started crossing the central meridian. For this purpose we analyzed automatic CH areas detected by the CHIMERA software (Garton, Gallagher, and Murray, 2018) and CH drawings. The peaks in the in situ measured solar wind speed that could not be related to CHs were also excluded from the statistical study. We considered observed and modeled solar wind peaks to be associated, i.e. a hit, if the increase started more or less simultaneously and the peak was achieved within two days after the peak as modeled by EUHFORIA. When the modeled solar wind increase did not have a counterpart in the in situ observations we considered this a false alarm, and when the observed fast flow was not reproduced by EUHFORIA we consider to have a miss. The manual identification of the CHs and associated fast flows shows 17 hits, 12 misses, and 6 false alarms for 2008 and 13 hits, 18 misses, and no false alarms for 2012. We note that these results reveal a significantly smaller number of false alarms and misses in comparison to the automatic method. This indicates that the CH development and its shape have strong influence on the fast solar wind speed profile measured at 1 AU.

This analysis showed that is, the comparison of the modeled and observed solar wind time series, very complicated task due to high dynamics of the compared time series. In order to improve the process

of validation of the quality of the background solar wind modeling we have developed a new method, so called Dynamic Time Warping. For details of this method see Samara et al. 2022.

4.1.1.4 Conclusions on the accuracy of solar wind modeling with EUHFORIA

In this Section we list some of the most important results of the study and refer to the parts of this report where the related studies are presented.

- *On how the open flux and the source surface heights influence modeling results.*

Comparing CH sizes extracted from EUV observations, and modeled open-flux areas (i.e. CH areas) by PFSS using GONG synoptic magnetograms shows that on average CHs are underestimated in the model. It is found that the amount of modeled open flux is lower than actually observed, and open-flux areas show up smaller in angular width (Section 4.2 and Asvestari et al. 2019). Failure in reliably modeling open magnetic flux has consequences for proper solarwind modeling, in particular for the fast solar-wind flow originating from CH areas. This will not only result in an underestimation of the solar-wind speed but also might cause the fast flow to be too narrow, and hence, the flow may completely miss the Earth. In a systematic test it was shown that changing the source-surface height (one of the default input parameters to EUHFORIA) significantly influences the modeled open flux and can even result in a shift of the position of the CH considered (Section 4.2 and Asvestari et al., 2019).

- *How the shape and location of CHs influence the accuracy of modeled solar wind.*

While manually associating the observed and modeled solar-wind flows (Section 3.1.2), we recognized that the EUHFORIA performance is closely related also to the size, shape, and location of the CHs. The qualitative study of the CH characteristics and the quality of the modeled fast solar wind (presented in this section) shows that for circular and equatorial CHs occurring during the low level of solar activity, EUHFORIA models well the associated fast flows. However, fast flows associated with narrow CHs elongated in longitude are rarely reproduced well by EUHFORIA. In the case of the narrow CHs elongated in latitude, the modeled solar wind is mostly underestimated, hence leading to a late arrival at the Earth. And when the solar wind is originating from low/high-latitude CHs (greater than $\pm 30^\circ$) and/or the extensions of polar CHs, it will rarely be reproduced correctly by EUHFORIA. We also noticed that fast flows associated with patchy CHs, irrespective of their latitudes and longitudes, are poorly reproduced or not reproduced at all by EUHFORIA. Furthermore, the fast flows originating from low-latitude CHs might pass South or North of the Earth (when the associated CHs are situated at the southern or northern solar hemisphere, respectively) and they will not be observed in the EUHFORIA time-series output at the Earth (see also Hofmeister et al. 2018). The extensive study on the relationship of the CHs and the associated fast solar wind is presented in Section 4.3.

- *Input parameters and resolution of EUHFORIA runs.*

In order to understand how different input parameters and resolution of the EUHFORIA runs influence the accuracy of modeled solar wind, we vary the resolution of the heliospheric model and the input density of the fast solar wind at the inner boundary compared to the default settings (we considered the time interval of 19 days).

The results show that a decrease of the solar wind density by 50% (initial value is 300 cm^{-3} at 0.1 AU) induces an increase of the modeled solar wind speed from several percent up to 15% (absolute value depends on the part of the flow that is considered).

We also found that the high resolution runs (2° and 512 cells, respectively) result in an increased solar-wind speed (up to about 20%) and in an earlier arrival time of the high-speed stream at 1 AU (up to several hours). If we compare the two extreme cases, the default EUHFORIA runs (angular and radial resolution of 4° and 256 cells, respectively) i.e. low resolution and high density, and the high-resolution and low-density runs, we find a shift of the arrival time of the fast flow of about -12 hours, and a significant increase of the solar wind speed (from about 6% to more than 40%, depending on which part of the fast flow is considered). These results indicate that the quality of the modeled fast solar wind varies a lot depending on the input parameters to the model. We note that when more than one parameter is modified the solar-wind speed changes in a non-linear manner and that the changes strongly depend on the flow considered.

These results bring forward the need for a detailed ensemble-parameter study that will provide a well-defined benchmark for solar-wind modeling with EUHFORIA. The parameter study of EUHFORIA's modeling background solar wind employing the novel PSP observations is in the progress (Samara et al., in preparations).

4.1.2. Reconstructing coronal hole areas with EUHFORIA and adapted WSA model: Optimizing the model parameters

This section presents mostly work published in Asvestari et al. (2019).

In order to inspect how the coronal model of EUHFORIA reproduces the fast solar wind we tested one of its main components, i.e. WSA model (See Section 3.1).

According to the generally accepted opinion, coronal holes are sources of open flux, and therefore also sources of fast solar wind. In order to test how good EUHFORIA reconstructs the open flux we use remote sensing EUV observations and CATCH tool (Collection of Analysis Tools for Coronal Holes; Heinemann et al. 2019) to extract CH areas and compare them to the open flux areas modeled by EUHFORIA.

We consider the adopted WSA model that is part of the default set up of EUHFORIA. In the coronal model of EUHFORIA we employed only the Potential FieldSource Surface (PFSS) model for the inner corona and the Schatten Current Sheet (SCS) model for the outer regions (PFSS+SCS). The height R_{ss} , of the outer boundary of the PFSS, known as the source surface, and the height R_i , of the inner boundary of the SCS are important parameters which can strongly affect the modeled CH areas. This study is focused to understanding which impact the two model parameters can have on the modelling results.

We vary R_{ss} within the interval $[1.4, 3.2] R_o$ with a step of $0.1R_o$, and R_i within the interval $[1.3, 2.8] R_o$ with the same step, and the condition that $R_i < R_{ss}$. This way we have a set of 184 initial parameters to the model, and we assess the model results for all these possible height pairs. More detailed description is presented below.

4.1.2.1 Data set and methodologies

Although the WSA model performs a global simulations and provides open-closed field regions for the entire surface we focus to the modeling results for the front side of the Sun, as seen from Earth, where the selected CHs are located. We also do not analyze results toward the limb, with one exception, that of the CH on 3 January 2017, which is linked to a polar CH.

In order to avoid any effects on the modeled results due to quantitative differences among magnetograms (Riley et al. 2014), we employed magnetograms provided by the Global Oscillation Network Group (GONG) and developed with the Air Force Data Assimilative Photospheric flux Transport (ADAPT) model (<ftp://gong.nso.edu/adapt/maps/gong/>).

The studied data set consists from 15 CHs observed in the time interval 2012-2017. All CHs have longitudinal position of center of mass (CoM) located along or within 10° of the central meridian of the Sun.

For extracting the CH boundaries, we employed CATCH tool and the EUV observations from the Atmospheric Imaging Assembly (AIA; Lemen et al. 2012) on board the Solar Dynamic Observatory (SDO; Pesnell et al. 2012). Although CHs might appear somewhat different when observed at different wavelengths, we used the full disk images at 193 \AA (size $1,024 \times 1,024$), which are the most frequently used for studies of CHs. The CATCH tool is an intensity threshold algorithm that is modulated by the intensity gradient along the CHs boundary.

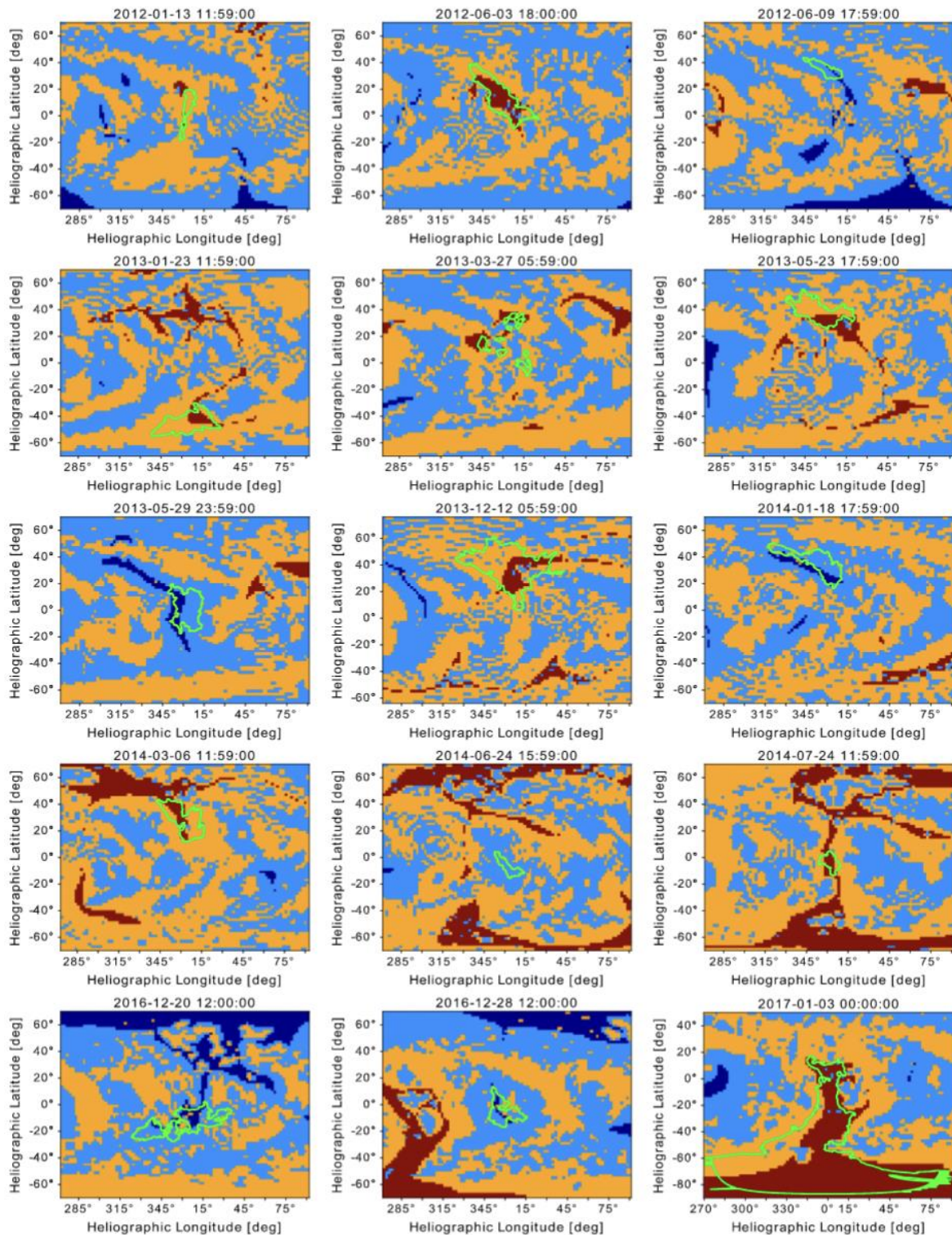


Figure 9

Model generated maps of open-closed field regions based on magnetic field reconstructions by the adopted WSA model in EUHFORIA. Dark blue and red regions represent open field areas of positive and negative polarity, respectively. Regions marked with cyan and orange are accordingly positive and negative closed field areas. The green outlines overplotted on the maps are the EUV defined optimal boundaries of the CHs as extracted with CATCH. Although the model generates the map for the entire solar surface, we plotted only a fraction of the map aiming to improve the clarity of the CH areas and the over plotted boundaries. (Adapted from Asvestari et al. 2019).

The reconstruction of open flux areas was done using EUHFORIA. For each of the selected CHs we run the coronal model of EUHFORIA for a large sample of $[R_i, R_{ss}]$ heights. To define the height pairs, we started with R_i taking the value of $1.3R_o$ up to $2.8R_o$ with a step of $0.1R_o$, and for each R_i we varied R_{ss} from $1.4R_o$ to $3.2R_o$ with the same step, and the condition that $R_i < R_{ss}$. ADAPT magnetograms, at date-time as that of the analyzed EUV images, were used as input to EUHFORIA model, which then produced maps of the open and closed magnetic regions for the specified input heights R_i and R_{ss} .

To create the open-closed flux maps, the solar surface is divided in a regular mesh consisting of pixels covering $2^\circ \times 2^\circ$ per pixel. For each pixel the procedure assigns a field line and traces it from the solar surface upwards toward the source surface. If the tracked field line is curved below the source surface and can be traced back down to the solar surface, it is assigned as a closed one. On the other hand, if the traced field line pierces through the source surface, it is accredited as an open one (see Figs. 1 and 9).

4.1.2.2 Results

A) CH reconstruction using the default model boundary heights

The results presented in Fig. 9 are the output of the model run for the default pair of heights, $[2.3, 2.6] R_o$. To better visualize the modeled CH area and the over plotted EUV-based boundaries, especially in the cases of very small CHs, we only plot the front side of the Sun (Earth view). In addition, for CHs that do not extend to polar regions, high latitudes of Northern and Southern Hemispheres are excluded from the images. The light green contours are the optimal CH boundaries derived from EUV observations using catch, as described in the previously.

The Fig. 9 also shows that, for most of the CHs, the model runs based on the default heights $[2.3, 2.6] R_o$ fail in reconstructing well the area and geometry as compared to the EUV extraction. Not only are the CHs modeled thinner and overall smaller but also for some cases (i.e., 9 June 2012, 23 May 2013, and 18 January 2014) the CHs appear to be shifted. For the CH of 24 June 2014 the model is unsuccessful in modeling open flux both within the expected boundaries and in the surrounding area. A CH that appears to be well modeled by EUHFORIA is the one on 3 January 2017, which is a southern polar CH with a large extension that reaches to low Northern Hemisphere latitudes. We note that the CH boundaries extracted with CATCH are only the part of the CH that is visible from Earth's line of sight. This explains why also in the EUHFORIA output open/closed field map we do not focus on longitudes beyond $\pm 90^\circ$.

B) Assessing for systematic shifting of open flux regions

Maps of open-closed flux indicate the possibility of shifting of the modeled CH areas with respect to the expected location. To assess this, we investigated the likelihood of a systematic shifting (see Fig. 10). All directions (eastward/westward and northward/southward) were investigated. In addition, we considered both a 2° and a 4° shifts in each direction. From this analysis no systematic effect could be identified. The role of CH characteristics, such as mean intensity, elongation, size, CoM latitude, and hemispheric position, in shifting effects was evaluated independently. Regardless of

whether the sample is assessed as a whole or divided in groups based on the CH characteristics, the conclusion for possible shifting remained negative for all cases.

C) Finding the optimum paired values for [R_i , R_{ss}]

Figure 10 is a collective plot for the coverage resulting from the model runs for each of the 184 height pairs and the 15 CHs. Each panel represents the results for a particular CH. The x-axis is the source surface height, the y-axis is the coverage, cov; and the color map defines the height of the inner boundary of the SCS model, R_i . The striking feature in this figure is that for the vast majority of the CHs reducing R_i significantly improves the modeled results. That is, the modeled open flux areas grow to cover more of the total expected area outlined by the EUV defined CH boundaries and thus better capture it. This is reflected in the improvement of the coverage, cov, parameter plotted on the y-axis of Fig.10.

4.1.2.3 Conclusions

This study aims to assess how accurate is the PFSS+SCS part of the adopted WSA model in modeling CH areas. Although values between 1.6 to 3.25 R_o are considered realistic

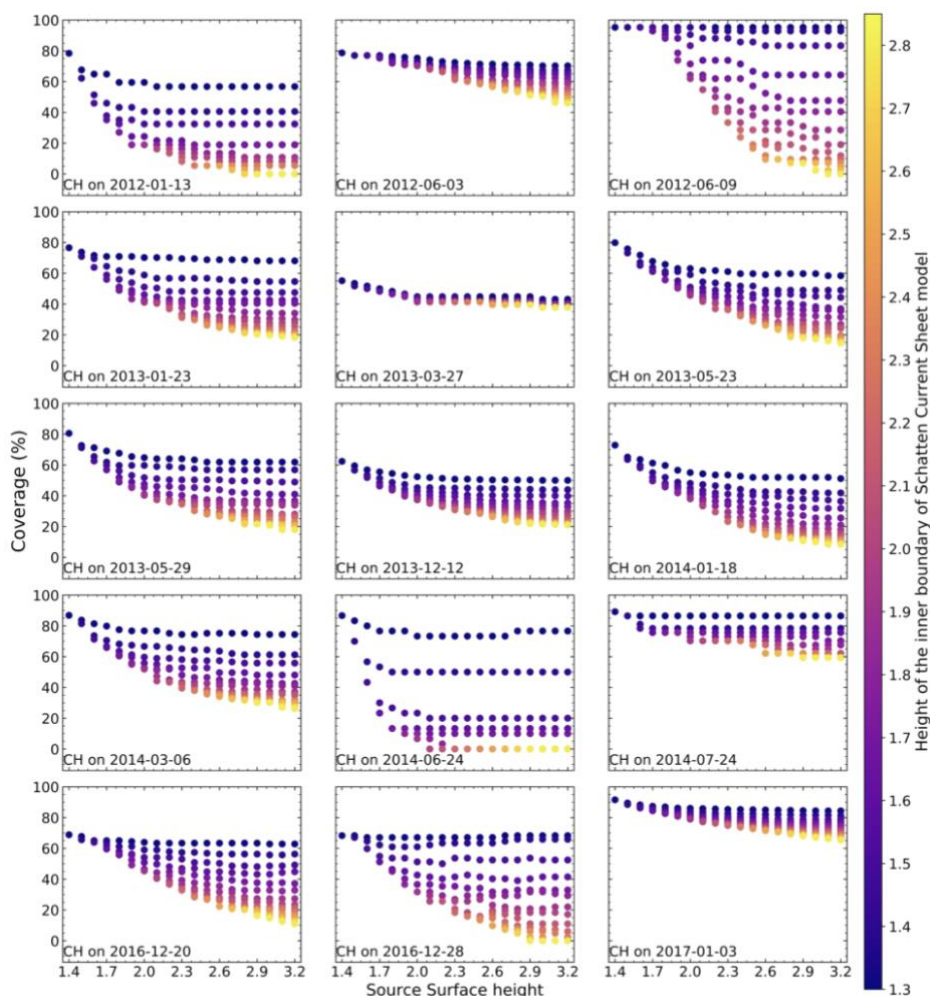


Figure 10

Collective results of model runs based on the 184 pairs of heights for the source surface and the inner boundary of the SCS model. Each panel presents the results for one CH, and they are placed in chronological order. The x-

axis is the source surface height, and the color bar is the height of the inner boundary of the SCS model increasing from dark to bright colors. The y axis shows the coverage, cov. For the majority of CHs best coverage is achieved for lower height values for the inner boundary of the SCS model. (Adapted from Asvestari et al. 2019).

for the source surface height, a commonly used value is $2.5R_o$ (e.g., Arge & Pizzo, 2000). McGregor et al. (2008) concluded that for the modified WSA model, which is also used in EUHFORIA, the optimal heights of the source surface and the SCS model inner boundary are $[2.3, 2.6] R_o$, which we considered as the default pair of heights.

Our main result is that the default heights employed so far, $[2.3, 2.6] R_o$, fail to model the expected CH areas and/or their locations, with coverage below 60%. This suggests that CH areas are not properly modeled using the default setup of EUHFORIA. This also explains the underestimated solar wind velocity discussed in Section 4.1 and in Hinterreiter et al. (2019). This result might also provide some explanation for the discrepancy between the open flux output by the WSA model and that measured in situ at Earth (Linker et al. 2017; Riley et al. 2015).

We note that in some of the studied cases even the whole CH was not reconstructed, but missed. This study clearly shows that lower heights (R_i below $1.5 R_o$ and R_{ss} below $2.3 R_o$) lead to an improved coverage (cov > 60%) of the CH areas defined by the EUV extracted boundaries, i.e., the modeled open field area better represents the EUV observed CH area. However, it also strongly results in opening flux outside the EUV defined CH boundaries as well. More precisely, modeled open flux areas mark a much larger region than the CH areas observed in EUV. This suggests the possibility that open flux can originate beyond CHs, which diverge from the standard paradigm according to which CHs are the sources of open field. This result also suggests that EUV-defined CHs might only provide a lower limit of the actual open field region. This last point is in agreement with Linker et al. (2017) result, that is, that lowering the heights leads to overestimating open flux regions. Assuming that the standard paradigm for open flux origin is correct, this raises the question of how low the source surface height can be placed in order to properly model CH areas and at the same time not model excess open flux areas outside the EUV defined boundaries. Considering modeling the SW velocity at 1 AU, it will be very interesting to see the effect of the modeled open flux areas outside the EUV defined boundaries can have. Our analysis also shows that it is rather the height of the inner boundary of the SCS model and not of the source surface that has a stronger effect on the modeled result. We also deduced that low values of this boundary lead to better results in terms of CH area reconstruction. It is noteworthy that this result is based on analyzing a CH sample from only one solar cycle and considers CHs located in the central meridional zone. Increasing the size of the sample and also extending it over a larger period of time can potentially lead to different height selection.

4.1.3 Influence of coronal hole morphology on the solar wind speed at Earth

This section presents mostly work published in Samara et al. (2022).

The results of study presented in Section 4.1 and 4.2 (Hinterreiter et al. 2019 and Asvestari et al. 2019) indicate large importance of the shape of CHs on the modeling results of EUHFORIA. The study by Samara et al. (2022) was performed in order to improve our knowledge on the association of the fast solar wind characteristics and the morphology of CHs, their sources on the Sun. The final aim

of this work is to implement newly obtained knowledge and further modify and improve EUHFORIA model.

It is generally accepted that the high-speed stream (HSS) peak velocity at Earth directly depends on the area of the CHs on the Sun, however, different degrees of association between the two parameters were obtained by different authors. We revisit this dependence employing the data set for which also all needed observations are available for modeling of the background solar wind with EUHFORIA. The aim of the study is to understand how CHs of different properties influence the HSS peak speeds observed at Earth and draw from this to improve solar wind modeling with EUHFORIA.

Our data set encompasses a sample of 45 nonpolar CHs observed during the minimum phase of solar cycle 24. The CH characteristics were extracted by the CATCH tool using EUV observations.

We first examined all the correlations between the geometric characteristics of the CHs and the HSS peak speed at Earth for the entire sample. The CHs were then categorized in two different groups based on morphological criteria, such as the aspect ratio and the orientation angle. We also defined the geometric complexity of the CHs, a parameter which is often neglected when the formation of the fast solar wind at Earth is studied.

The quantification of complexity was done in two ways. First, we considered the ratio of the maximum inscribed rectangle over the convex hull area of the CH. The maximum inscribed rectangle provides an estimate of the area from which the maximum speed of the stream originates. The convex hull area is an estimate of how irregular the CH boundary is. The second way of quantifying the CH complexity was carried out by calculating the CH's fractal dimension which characterizes the raggedness of the CH boundary and internal structure.

Considering the entire sample, we obtained the best correlations between the HSS peak speed observed in situ, and the CH longitudinal extent. When the data set was split into different subsets, based on the CH aspect ratio and orientation angle, the correlations between the HSS maximum velocity and the CH geometric characteristics significantly improved in comparison to the ones estimated for the whole sample. By further dividing CHs into subsets based on their fractal dimension, we found that the Pearson's correlation coefficient in the HSS peak speed – CH area plot decreases when going from the least complex toward the most complex structures. Similar results were obtained when we considered categories of CHs based on the ratio of the maximum inscribed rectangle over the convex hull area of the CH. To verify the robustness of these results, we applied the bootstrapping technique. The method confirmed our findings for the entire CH sample. It also confirmed the improved correlations, compared to the ones found for the whole sample, between the HSS peak speed and the CH geometric characteristics when we divided the CHs into groups based on their aspect ratio and orientation angle. Bootstrapping results for the CH complexity categorizations are, nonetheless, more ambiguous.

Our results show that the morphological parameters of CHs such as the aspect ratio, orientation angle, and complexity play a major role in determining the HSS peak speed at 1 AU. Therefore, they need to be taken into consideration for empirical models that aim to forecast the fast solar wind at Earth based on the observed CH solar sources.

4.1.3.1 About data sets and methods

The starting data set were the 1-minute in situ solar wind observations during the recent solar minimum interval from November 2017 to September 2019. The solar wind in situ signatures (bulk speed v_b ; proton density n ; temperature T ; magnitude of the interplanetary magnetic field (IMF) B ; the IMF latitudinal component B_z ; and the IMF longitudinal ϕ -angle) observed at the Lagrangian point 1 (L1) by the Wind spacecraft (Ogilvie et al. 1995) were examined in order to identify clear HSS cases. In order to focus only on clearly undisturbed HSSs, we excluded all the intervals for which an interplanetary coronal mass ejection (ICME) was recorded based on the RichardsonCane list (Richardson & Cane 2010).

In the considered time window of 25 Carrington rotations, we isolated 63 events that contained all the signatures of a HSS following the common definition. A HSS was identified when a simultaneous increase in the solar wind speed and the temperature was recorded, preceded by a density increase. The density increase indicated the arrival of the compression region that was formed from the interaction of the upcoming fast solar wind with the preceding slow solar wind. An increase in the total magnetic field strength was also observed due to that compression. Additionally, the longitudinal angle of the IMF vector (ϕ -angle), indicated if the field was pointing toward or away from the Sun. This angle should be predominantly in one of those two directions and match the polarity of the source CH in order to confirm the arrival of the HSS. It was calculated by taking into account the arctan of the B_x , B_y components of the IMF in the Geocentric Solar Ecliptic (GSE) frame.

The criteria for the detection of HSSs also consider velocities above 400 km/s (Schwenn 2006; Vršnak et al. 2007). After isolating the HSSs in the in situ observations, we searched for the CHs from which these fast streams originated. For that purpose, we inspected images of the Sun two to five days (which corresponds to the usual travel time of HSSs from the Sun to Earth) prior to the beginning of each HSS. The inspection was done by employing EUV observations at 193 Å, recorded by AIA. Additionally, we examined the NOAA full-Sun drawings in order to confirm the position and polarity of the CH. The NOAA drawings are based on H-alpha observations, sunspots, magnetograms, as well as on He I 10830Å ground-based observations which help define the CH boundaries. In order to confirm the association between a HSS and a particular CH, we required that the polarity of the ϕ -angle detected in the in situ observations was the same as the polarity of the CH in the NOAA drawings.

The CH characteristics were extracted using the CATCH tool (Heinemann et al. 2019). The basic principle of the CH extraction relies on an intensity-based threshold technique applied to EUV filtergrams of sufficient contrast, a preliminary form of which was developed by Rotter et al. (2012a). We note that, even if all CHs are individually processed and extracted by CATCH, the procedure is not sufficiently accurate for polar CHs due to the strong projection effects and the lack of reliable information from the Sun's polar regions. Therefore, we excluded all the extensions of the polar CHs (18 out of the total 63 CHs) from our set and only focused on the nonpolar ones (45 out of 63 in total). Our data set includes all nonpolar CHs found in the time interval November 2017 - September 2019, and which are associated with HSSs observed at Earth and their center of mass (CoM) is found on (or very close to) the central meridian since the connectivity of the CH with Earth, through the produced HSS, is optimal in this case. No other preselection criteria were applied, i.e., our sample contains CHs of different sizes and shapes.

4.1.3.2 Defining geometric complexity of CHs & CHs as fractal objects

In the process of modeling and forecasting the HSS arrival, one of the frequently ignored parameters is the CH geometric complexity. This parameter was, up to now not systematically discussed in the literature. We have quantify the geometric complexity of the CHs in the two different ways: a) by taking the ratio of the maximum rectangle that can be inscribed within the CH, over the convex hull area of the CH, and b) by calculating the fractal dimension (FD) of the CHs. We note that the first way is simpler and more approximate. The second way is more precise since fractality estimates the self-similarity of a structure over different scales.

Abramenko et al. (2009) was, to our knowledge, the only other author that addressed the fractality of CHs. Their work was focused on the complexity of the CH magnetic fields and not on the morphological structure of the CHs.

Reiss et al. (2016) were the first to mathematically introduce the parameter of “compactness” as a measure to quantify how irregular the shape of a CH is and distinguish among CHs and filament channels. Based on shape analysis, compactness (C) is defined as follows:

$$C = U^2 / 4\pi A, \quad (1)$$

where U denotes the perimeter of the structure and A is the CH area. The definition by Reiss et al. (2016) is not applicable to this study because it does not take into account how hollow the internal part of the CH is. The meaning of CH complexity should not be restricted to the irregularity of the outer boundary of the structure, but further include the internal part of it. This area is not always compact and it may well influence the maximum HSS velocity. Therefore, we sought a more encompassing measure to quantify the geometric complexity of the CHs by considering both the fragmentation in the interior and the raggedness along the boundary.

A) Solidity: the ratio of the maximum inscribed rectangle over the convex hull area

The first, more approximate way to quantify the CH complexity is by estimating the ratio of the maximum rectangle that can be inscribed within the interior of a CH, over the convex hull area of that CH. The convex hull area envelops all line segments that join any two points of the edge of the structure. We refer to this parameter as “Solidity”. Figure 10 shows a small (Fig. 10a) and large (Fig. 10b) value of the Solidity, corresponding to a fragmented and compact CH, respectively. The maximum inscribed rectangle (red rectangle in Fig. 10) is an approximation of the biggest, most compact area found inside a CH. As a result, this quantity should be a good approximation of the area from which the fastest part of the solar wind originates. To calculate the maximum inscribed rectangle within the CH, we used the MATLAB function from Seibold (2020). We chose a rectangular shape instead of a circular or square one, as it accounts for the maximum area of the compact part of the CH better.

B) CHs as fractal objects

Another way of quantifying the complexity of a CH area is by calculating the fractal dimension (FD) of its contours (both internal and external). The fractal analysis is a mathematical method for measuring complexity in nature and it has been long used in different scientific domains. The complexity and FD of an object increases as the object’s border is more ragged; the branching pattern

is more irregular and lines get more twisted. Fractality characterizes the self-similarity of a structure over different scales.

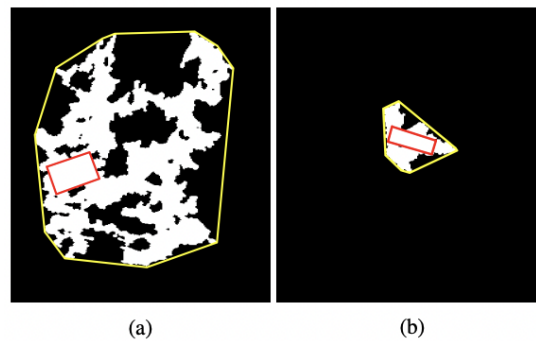


Figure 11

Examples of the maximum inscribed rectangle in the interior part of CHs (red box) and the convex hull area (the area included inside the yellow lines of each structure). Panel (a): Very fragmented and patchy CH with a maximum inscribed rectangle = $1.08 \times 10^{10} \text{ km}^2$, a convex hull area = $31.69 \times 10^{10} \text{ km}^2$, and Solidity = 0.03. Panel (b): More compact CH with a maximum inscribed rectangle = $0.49 \times 10^{10} \text{ km}^2$, a convex hull area = $1.87 \times 10^{10} \text{ km}^2$, and Solidity = 0.26. (Adapted from Samara et al., 2022).

On the other hand, the convex hull area (the area included inside the yellow lines shown in Fig. 10) provides a quantification of the smallest convex set that contains all points of our structure. The more irregular the boundary of a CH is, the larger the convex hull area becomes. Therefore, for a Solidity close to 1, the CH is compact enough to have its edges close to its main body (Fig. 11b), whereas a Solidity much smaller than 1 implies a very fragmented, inherently hollow, structure (Fig. 11a).

The landmark book of Mandelbrot (1983, and references therein) has shown that the boundary length of a fractal object can be mathematically expressed as a power law of the following form: $N(r) = \text{const} \times r^{-D}$, where $N(r)$ presents a measure of the fractal structure at scale r . The parameter D is called “fractal” because it is not an integer number and is called a “dimension” because it provides a measure of how completely an object fills the space. If D is an integer number, then it is equal to the Euclidean dimension in which an ideal point has dimension 0, a line has dimension 1, a plane has dimension 2, and an ideal solid volume has dimension 3. Applying this to our CH maps, which are not straight lines and do not cover the whole two-dimensional space, the FD is in the range $1 < D < 2$. A number of methods have been developed to estimate the FD of an object such as the Hausdorff dimension, the Minkowski-Bouligand, or the box-counting method.

In the framework of our analysis, we followed the dimensionless box counting procedure by Georgoulis (2005, 2012). Based on this method, the binary image of interest is covered by $(L/\lambda)^2$ boxes, where L corresponds to the linear dimension of the image and λ is the size of the box’s edge. By varying λ , we counted the number of boxes $N(\lambda)$ that contain part of the structure of interest. The complexity results for our CHs, which are based on both the fractal dimension and Solidity measures can be found in Table 3 by Samara et al., 2022. The first two columns show the ranking based on the Solidity, while the next two columns show the results based on the fractal dimension. Figure 11 presents the relation between the Solidity and the FD. We note that the two parameters are inverted quantities. Namely,

less complex CHs correspond to higher values of the Solidity and lower values of FD. On the other hand, more complex CHs correspond to lower values of the Solidity, and higher values of FD.

Figure 12 presents the Solidity and the FD (panels (a) and (b), respectively), as a function of the CH area. The HSS peak velocity is color-coded. We find that small CHs are statistically less complex, while large CHs show a high degree of complexity. From the same plots, we also deduce that smaller HSS peak speeds, namely between 400 - 500 km/s, stem from smaller, less complex CHs with areas below $4 \times 10^{10} \text{ km}^2$ (dark blue-shaded circles). Faster HSSs stem from progressively more complex, but importantly larger, CHs.

To understand how the CH complexity influences the HSS velocity at Earth, we studied the relation between the HSS peak velocity and CH area by splitting the CHs into groups based on their FD and Solidity. For our sample, the FD ranges between 1.10 and 1.40. Therefore, three different groups were taken into account, namely, $FD = (1.1, 1.2]$, $FD = (1.2, 1.3]$, and $FD = (1.3, 1.4]$, beginning from the least complex to the most complex structures, respectively. Figure 13 shows how the HSS peak velocity depends on the CH area for the three defined categories. For the least complex CHs (Fig. 13a), we obtain a good correlation ($cc = 0.74$) between the two parameters.

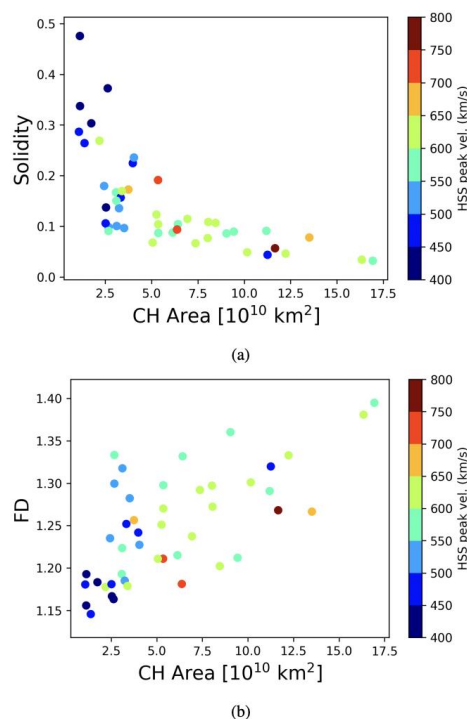


Figure 12

Panel (a) Solidity as a function of the CH area. Panel (b) The fractal dimension as a function of the CH area. The HSS peak velocity is color-coded.

(Adapted from Samara et al., 2022).

We note that this subset contains CHs of small sizes (mostly below $4 \times 10^{10} \text{ km}^2$). As the geometric complexity increases (see Fig. 13b), the CH size becomes bigger and the correlation between the peak velocity of the HSS at Earth and the CH area decreases ($cc = 0.57$). For the most complex CHs (see Fig.

13c), a weak, possibly not very important correlation is obtained. We repeated the same procedure by splitting our points based on the Solidity (see Fig. 14)..

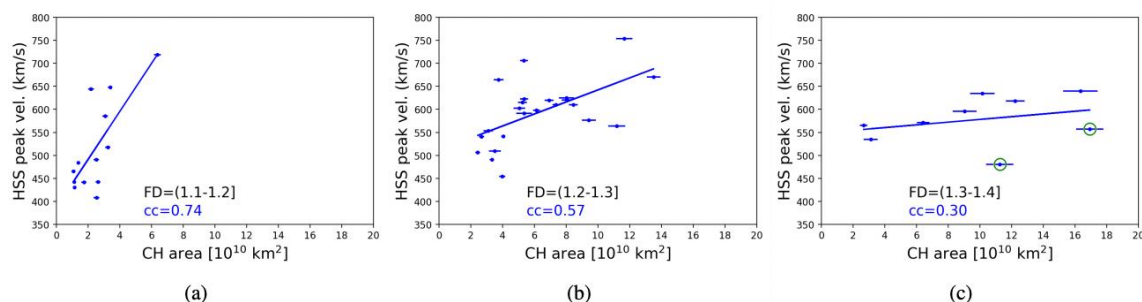


Figure 13

HSS peak velocity as a function of the CH area for different FD ranges, going from the least complex (panel a) to the most complex (panel c) CHs. Green circles in panel (c) indicate the points responsible for the second peak observed in the Pearson's cc distribution after the application of the bootstrapping technique (Fig. C.1c). (Adapted from Samara et al., 2022).

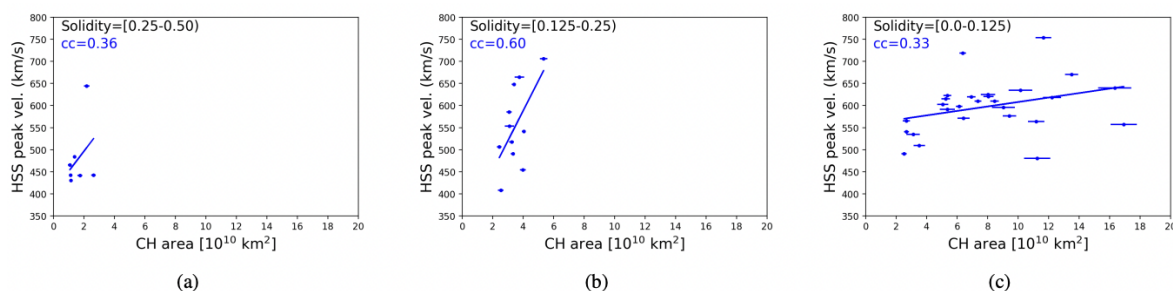


Figure 14

HSS peak velocity as a function of the CH area for different Solidity ranges, going from the least complex (panel a) to the most complex (panel c) CHs. (Adapted from Samara et al., 2022).

The latter parameter ranges from between 0 - 0.5. We divided this interval into three groups as well based on the ranges [0, 0.125), [0.125, 0.25), and [0.25, 0.50), which go from the most complex to the least complex structures, respectively. Our results in Fig. 14 show that the cc in the HSS peak velocity – CH area plots for the different Solidity subsets follow the same pattern found based on the FD grouping, but only for the medium and most complex CHs. Namely, the cc for CHs of medium complexity (Fig. 14b) is 0.60 and drops for the very complex CHs to cc = 0.33 (Fig. 14c). For the first subgroup (Fig. 14a) cc = 0.36, which is lower than the one estimated for the medium-complexity group. The noticeably less significant association seen in Fig. 14a, compared to the one seen in Fig. 13a, possibly happens due to the definition of the Solidity which, as explained earlier, is a rougher complexity measure compared to the FD.

4.1.3.3 Some results

In this Section we listed some of the results obtained in the framework of this study, for more details please see Samara et al. 2022

In this study we inspected CH characteristics such as the CH area, CH longitudinal and latitudinal extent, CH CoM latitude, and their relationship with the maximum velocity and duration of the HSS at Earth. We divided our sample into different groups based on geometric criteria such as their aspect ratio, orientation angle, and geometric complexity.

Main conclusions of this study are summarized as follows:

- For the full data set, the best correlation is obtained between the CH longitudinal extent and the HSS peak velocity in situ with a $cc = 0.57$. The better correlation between these two parameters, compared to what was estimated between the HSS peak velocity and the CH area or HSS peak velocity and CH latitudinal extent, is a consequence of the propagation effects that a HSS undergoes on the way from the Sun to Earth. CHs with larger longitudinal extents produce faster HSSs at Earth, up until the extent of 32 deg for our sample ($cc = 0.75$). Beyond this threshold, regardless of the increase in the longitudinal width of a CH, the HSS peak speed no longer increases.

- We did not find a good correlation between the CH area and the latitudinal extent do not seem to be very strongly associated with the HSS duration observed in situ. As expected, the HSS duration has the best correlation with the CH longitudinal extent ($cc = 0.68$).

- When dividing data sample into two different groups based on their aspect ratio (longitudinal over latitudinal extent), we find that CHs with an aspect ratio < 1 show better correlations between the HSS peak velocity and the CH characteristics (area, longitudinal, and latitudinal extent), not only compared to the CHs with an aspect ratio higher than one, but also compared to the entire sample. In the case of an aspect ratio < 1 , the associated HSSs more probably directly impact Earth, not just brush it off with their flanks. Furthermore, the majority of the CHs in this group have comparable latitudinal and longitudinal extents, which induce the longer impact of the HSS and assures arrival of the fastest part of the HSS.

- We also divided the main data set into groups based on the CHs' orientation angle, with respect to the solar equator. The majority of CHs with negative orientation angles are situated in the northern solar hemisphere, and have their leading edge toward the equator. This subset shows very good correlations between the CH geometric characteristics and the HSS maximum velocity at Earth, which are better than the ones found for the entire sample. The same was obtained for the CHs with positive orientation angles, after the removal of outliers. Most CHs in this subset are situated in the southern solar hemisphere with their leading edge toward the equator.

- We also categorized our sample based on the degree of geometric complexity, a parameter, that, to our knowledge, is not usually considered in similar studies. We introduced two parameters to quantify the complexity: the ratio of the maximum inscribed rectangle over the convex hull CH area, which we call "the Solidity," and the fractal dimension (FD) of the structures. Both methods consider the irregularity of the CH boundary, but also the hollowness within the interior part of the CHs. We have found that the correlation between the HSS peak velocity at Earth and the CH area systematically decreases with the increase in the FD (increase in complexity). A good correlation ($cc = 0.74$) is identified for the least complex CHs, a medium correlation ($cc = 0.57$) for the medium-complex CHs, and a poor correlation ($cc = 0.30$) for the most complex structures. When categorizing our sample based on the Solidity, our results show a decrease in cc for the medium complex to the most complex CHs, whereas the results are more ambiguous for the least complex CHs.

- To confirm the reliability of the obtained results for the entire data sample and the different subsamples, we applied the bootstrapping method. This method is usually applied to small data sets in order to validate the statistical significance of the results obtained with other methods. Bootstrapping led to the same results for the entire sample compared to what we found based on the original data set. Namely, when treating the data set as a whole, the best correlation is obtained between the HSS peak velocity and the CH longitudinal extent, rather than the CH area or latitudinal extent. Bootstrapping also confirmed our results in the cases of the aspect ratio and orientation angle. The associations of the CH area, as well as longitudinal and latitudinal extents with the HSS peak speed in situ are stronger when we split our data set based on these two parameters, rather than when we dealt with the entire sample at once. Therefore, we conclude that both the aspect ratio and orientation angle are significant geometric factors that influence the way a HSS encounters Earth. They should be considered for empirical relationships and models that aim to predict the fast solar wind based on the CH properties observed on the Sun. Moreover, results with bootstrapping show that the median value of the Pearson's cc decreases while going from the least complex to the most complex CHs, based on the criterion of FD. This result agrees with our findings obtained from the original data set. The very low correlation found between the HSS peak speed and CH area for the most complex CHs is somewhat ambiguous, though. The bootstrapping method shows the existence of a second peak in the distribution, indicative of the possibility that some combinations of data points can give a very high cc . Such high cc values mainly occur when the two data points, circled in green below the linear regression line of Fig. 13c, are not considered during the resampling of the bootstrapping. Nevertheless, we should not assume that they are outliers or remove them from the statistics because they correspond to big and patchy CHs according to the criteria of that subsample. We note that this was the smallest subsample among the three considered. A bigger and more diverse sample of CHs would clarify if the Pearson's cc continued to decrease or not, in the case of the CHs of very high FD. Regarding the CHs' categorization based on the Solidity, the results with bootstrapping show that the median Pearson's cc drops when going from the medium complex to the most complex CHs. Our findings for the least complex group are ambiguous because of the large scattering of the points (Fig. 13a) and the large interquartile range of the cc , after the bootstrapping application. This study highlights the need to better understand the CH characteristics. It helped us identify the most important parameters and correlations that need to be addressed and, ideally, understood to forecast the solar wind at Earth better. We have found that out of all the different CH characteristics, their aspect ratio, orientation angle, and complexity seem to be parameters that need to be taken into account for solar wind modeling and forecasting purposes. A follow-up study will aim to understand how the revealed correlations can help improve solar wind modeling with the EUHFORIA.

4.2 Modeling CME-ICMEs with EUHFORIA

In the framework of the CCSOM project significant number of scientific papers was published with the topic related to the CME modeling and implementation of different CME models or different coronal model into EUHFORIA. In this section some of these publications will be briefly addressed.

4.2.1 Selection of the CME models & methodology for obtaining the CME parameters needed as input to EUHFORIA

At the beginning of the CCSOM project we investigated the implementation of CME models in EUHFORIA that include an internal magnetic field structure. Altogether four new CME models were inspected: 1) A spherical hydrodynamic model; 2) A linear force-free spheromak model (LFF model); 3) A magnetohydrostatic spheromak model and 4) The Gibson-Low flux rope model.

During the initial testing of the models, the spheromak models (Fig. 15) were selected to receive the focus of the development efforts, in the framework of this project. The reason for that was the relative simplicity of the models in relation to the Gibson-Low (GL) model. In the GL model, a significant complication is that the legs of the model CME remains attached to the Sun (Fig.16). When modelling several consecutive events, as is often the case, the CME needs to detach in order to allow other CMEs to take over.

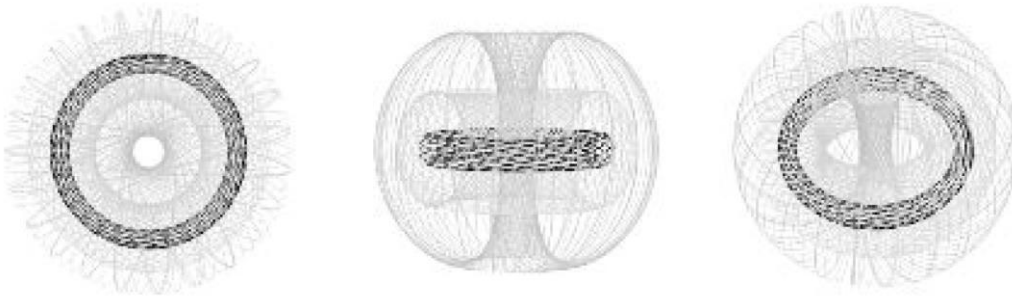


Figure 15

Three different views of the spheromak CME model.

On the other hand, the spheromak-type models do not suffer from this as they are closed magnetic structures enclosed within a sphere. This considerably simplifies the insertion of the CMEs into the dynamic solar wind. In addition, the models have only a few additional parameters as compared to the hydrodynamic models regularly used with EUHFORIA.

However, at the beginning of the project it was not clear how well the spheromak models will perform in modelling of CMEs and CME-driven shock waves. Therefore, although the main focus, was on the spheromak models, also the GL model was implemented. In addition, a spherical hydrodynamic CME was also implemented to serve as the hydrodynamic counterpart of the spheromak models. Two spheromak models were implemented in EUHFORIA: a linear force-free model and a magnetohydrostatic version. In the later, the CME model fulfils the condition of magnetohydrostatic equilibrium,

$$\mathbf{J} \times \mathbf{B} - \nabla P = 0 \quad (3)$$

while in the former the Lorentz force vanishes which requires the thermal pressure to be uniform within the CME. The two models allow us to study the effect of internal pressure equilibrium on the propagation and evolution of CMEs in the heliosphere.

Coronagraph observations from multiple points of view (e.g. obtained from SOHO/LASCO and STEREO/COR) were used to reconstruct the 3D kinematic and geometric parameters of the selected CMEs. In the reconstruction of the CME velocity, particular focus was put on the development of a method which allows us to separate the contributions of the radial/translational speed and of the

expansion speed to the total 3D speed. We present the method and briefly discuss the importance of this separation.

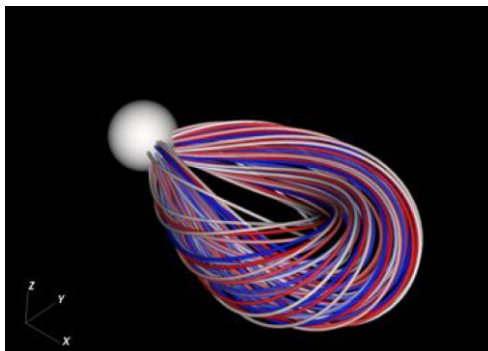


Figure 16

The schematic presentation of the Gibson - Low CME model.

When propagating in the solar corona, CMEs typically start exhibiting a self-similarly expanding behaviour starting from about 3 R_{\odot} . In such a cases (this is true for majority of CMEs), the total speed of the CME central leading edge, also called CME nose, is the sum of two contribution. One part is coming from the displacement of the CME centre of mass, and one associated to the increasing of its size/radius (Fig. 17). When the CME is observed from one point of view only, the separation of the two speed components is almost impossible due to projection effects and insufficient vantage points of view. However, when fitting white-light CME images, i.e., coronagraph observations, with some of the 3D reconstruction model, it is possible to estimate the expansion speed and the radial speed of the CME nose using analytical relations.

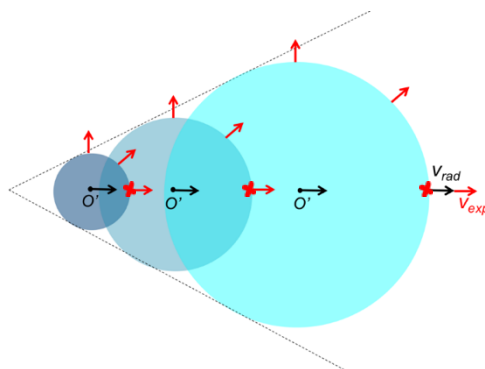


Figure 17

The schematic presentation of the contribution of the radial and expansion speeds to the total speed of the CME at the nose, for a self-similarly expanding CME.

A sketch with marked parameters characterising the CME shape in the Graduated Cylindrical Shell (GCS model; Thernisien 2006, 2009) is presented in Fig.18. In this model, the expansion speed can be estimated from the variation in time of the radius R ($\theta=\pi/2$). The radial speed that corresponds to the speed of the CMEs centre of mass propagating away from the Sun, can be estimated from the variation in time of the segment marked as OC1.

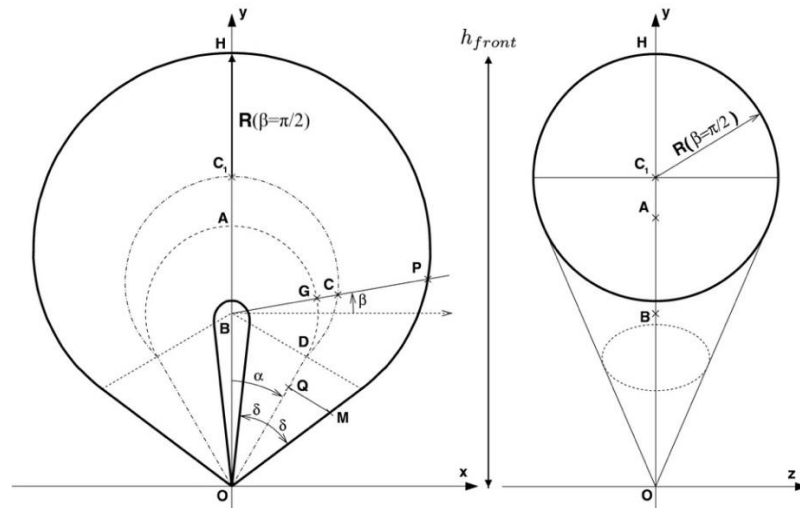


Figure 18

The schematic presentation of the GCS model for reconstruction of the CMEs and obtaining the parameters needed for modelling CMEs in EUHFORIA. The face-on (left) and edge-on (right) representations. In the case $\alpha = 0$, the face-on and edge-on views coincide. (Adapted from Scolini et al., 2019).

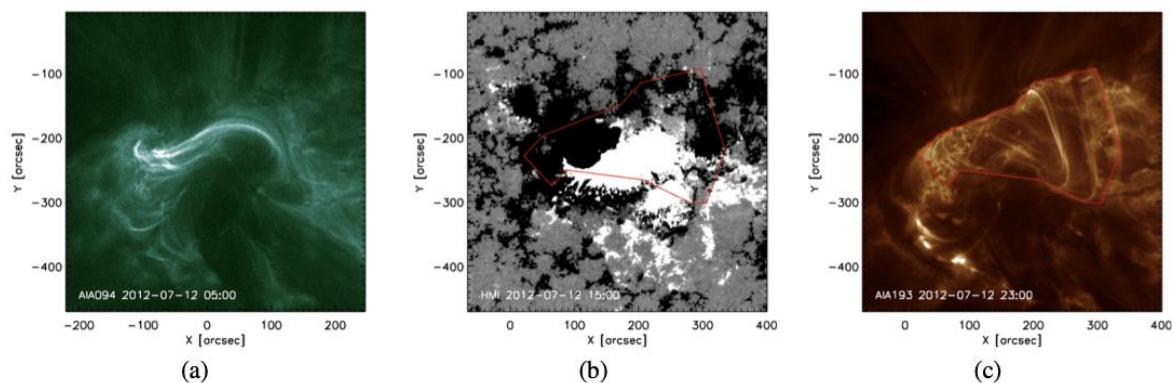


Figure 18

Example of 12 July 2012 event (AR 11520). Panel a): AIA 94 Å image of the pre-eruptive sigmoid. Panel b): HMI magneto-gram with PEA area overlaid (saturated at -100 gauss and +100 gauss). Panel c) PEA from AIA 193 Å with the area outlined by a polygon. (Adapted from Scolini et al., 2019).

Additionally to the CME kinematic and the magnetic parameters, we also investigated the determination of the CME magnetic field orientation, helicity, and strength from photospheric and low-coronal observations of CMEs and their source Active Regions (ARs). An accurate determination of those magnetic parameters is crucial for making reliable predictions of the ICME properties at Earth. Moreover, this is particularly important for modelling with EUHFORIA that has implemented the new spheromak flux-rope CME model.

- As indication of the original orientation of the flux-rope axis, the direction of the main Polarity Inversion Line (PIL) in the AR, and/or the orientation of the Post-Eruptive Arcade (PEA) developing after the eruption needs to be considered. Although the CME magnetic field orientation can be altered by rotations occurring in the low corona, based on observations of

the source AR, we start from the simplest case in which the CME undergoes no or little rotation during its propagation from the Sun to 0.1 AU.

- The helicity of the flux-rope structure is estimated from EUV observations of the source AR, often showing evidence of pre-eruptive sigmoids.
- For the determination of the CME magnetic field strength, the approach proposed by Gopalswamy et al. (2017), originally developed assuming a Lundquist flux-rope solution, can be extended to a linear force-free spheromak magnetic field configuration (corresponding to the same flux-rope model implemented in EUHFORIA). The method allows to estimate the magnetic field strength and toroidal field in a flux-rope structure, based on the magnetic flux that has reconnected in an AR in association to an erupting event. The reconnected flux is in turn estimated by combining observations of the AR photospheric magnetic field with that of the PEA developing after the eruption. The method, adapted to the equations of a spheromak configuration, has been tested on several test case events. The properties of NOAA AR 11520, source region of the halo CME studied by Scolini et al. 2019, are presented in Figure 19.

4.2.2 The evolution of coronal mass ejections in the inner heliosphere: Implementing the spheromak model with EUHFORIA

This section presents mostly work published in Verbeke et al. (2019).

This publication presents the implementation of a new model for CMEs in the magnetohydrodynamics (MHD) inner heliosphere model EUHFORIA. Utilising a linear force-free spheromak (LFFS) solution, the model provides an intrinsic magnetic field structure for the CME (Fig.19). As a result, the new model has the potential to predict the magnetic components of CMEs at Earth. In this paper, we present the implementation of the new model and show the model capability. We present the initial validation runs for the new magnetised CME model by considering the same set of events as used in the initial validation run of EUHFORIA that employed the cone model. In particular, we have focused on modelling the CME that was responsible for creating the largest geomagnetic disturbance (Dst index). Two scenarios are discussed: one where a single magnetised CME is launched and another in which we launch all five Earth-directed CMEs that were observed during the considered time period. Four out of the five CMEs were modelled using the Cone model.

In the first run, where the propagation of a single magnetized CME is considered, we find that the magnetic field components at Earth are well reproduced as compared to in-situ spacecraft data. Considering a virtual spacecraft that is separated approximately seven heliographic degrees from the position of Earth, we note that the centre of the magnetic cloud is missing Earth and a considerably larger magnetic field strength can be found when shifting to that location. For the second run, launching four Cone CMEs and one LFFS CME, we notice that the simulated magnetised CME is arriving at the same time as in the corresponding full Cone model run. We find that to achieve this, the speed of the CME needs to be reduced in order to compensate for the expansion of the CME due to the addition of the magnetic field inside the CME. The reduced initial speed of the CME and the added magnetic field structure give rise to a very similar propagation of the CME with approximately the same arrival time at 1 AU.

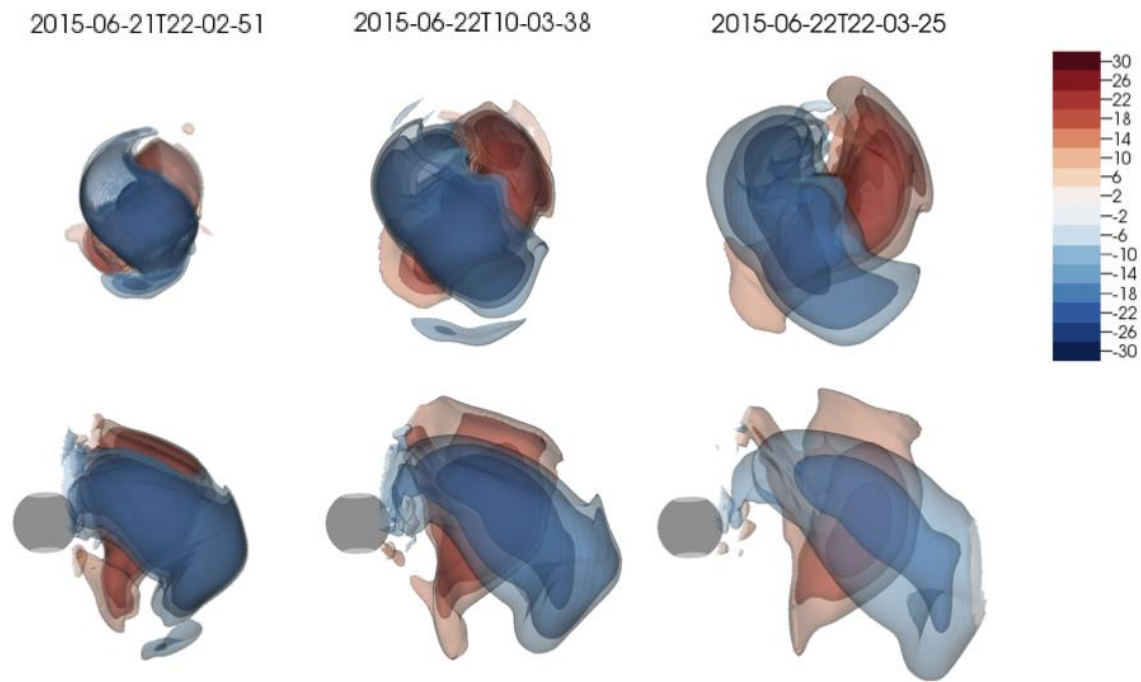


Figure 19

Snapshots of the magnetic B_z structure [nT] of the LFFS CME as tracked through the inner heliosphere for different time stamps. *Top panels*: view from Earth towards the Sun, that is hidden behind the magnetic structure, *bottom panels*: side view. (Adapted from Verbeke et al., 2019).

In contrast to the Cone model, however, the magnetised CME is able to predict the magnetic field components at Earth. However, due to the interaction between the Cone model CMEs and the magnetised CME, the magnetic field amplitude is significantly lower than for the run using a single magnetised CME.

We can conclude that the LFFS model is able to simulate and predict the magnetic field components and the propagation of magnetised CMEs in the inner heliosphere and at Earth. We note that shifting towards a virtual spacecraft in the neighbourhood of Earth can give rise to much stronger magnetic field components. This gives the option of adding a grid of virtual spacecrafts to give a range of values for the magnetic field components.

For more details of this study see Verbeke et al. (2019).

4.2.3 Observation-based modelling of magnetized coronal mass ejections with EUHFORIA

This section presents mostly work published in Scolini et al. (2019).

Coronal mass ejections (CMEs) are the primary source of strong space weather disturbances at Earth. Their geo-effectiveness is largely determined by their dynamic pressure and internal magnetic fields, for which reliable predictions at Earth are not possible with traditional cone CME models. This study was focused to modeling of two well-observed Earth-directed CMEs, testing for the first time the predictive capabilities of a linear force-free spheromak CME model initialised using parameters derived from remote-sensing observations. We have employed observation-based CME input parameters, in modeling with EUHFORIA and the cone and spheromak CME models.

Simulations show that spheromak CMEs propagate faster than cone CMEs when initialised with the same kinematic parameters. We interpret these differences as the result of different Lorentz forces acting within cone and spheromak CMEs, which lead to different CME expansions in the heliosphere. Such discrepancies can be mitigated by initialising spheromak CMEs with a reduced speed corresponding to the radial speed only. Results at Earth provide evidence that the spheromak model improves the predictions of B (B_z) in comparison to a cone model. When considering virtual spacecraft located within $\pm 10^\circ$ around Earth, B (B_z) predictions reach 45–70% (58–78%) of the observed peak values. The spheromak model shows inaccurate predictions of the magnetic field parameters at Earth for CMEs propagating away from the Sun-Earth line, so extra care due to limitations related to the assumed spherical shape is needed. The spatial variability of the modelling results and the typical uncertainties in the reconstructed CME direction indicate the need to consider predictions at Earth and at virtual spacecraft located around it.

4.2.3.1 Some findings on modeling CMEs with cone and spheromak model

The main aim of this study, focused on the two Earth-directed CME events, was assessing the capabilities of the new spheromak CME model in predicting the ICME magnetic properties at Earth. The CMEs were initialised using CME parameters derived directly from remote sensing observations. We discuss here the differences in terms of the dominating forces acting on the CMEs in the MHD description. For each event, we simulated the CMEs using both the cone model and the spheromak model. Our analysis indicates that the use of a spheromak model initialised with observations-based CME input parameters significantly improves the prediction of the ICME internal magnetic field intensity and orientation at Earth (see Figs. 20 and 21). These results also make us expect a net improvement in the prediction of the CME geo-effectiveness in terms of impact on the terrestrial environment. The prediction of the CME arrival time at Earth was found to be highly dependent on the CME model and CME input parameters used, and a detailed investigation of the forces acting on the CMEs was needed in order to understand its dependence on the CME initialisation.

The key findings of this work can be summarised as follows.

- 1.** The determination of the CME parameters at 0.1 AU from remote-sensing observations is an extremely challenging process. It can be performed only in the case of well observed events, and even then it still needs to be complemented by a number of assumptions and approximations. Being aware of such limitations, we performed this first analysis for two CMEs that were observed by the full constellation of spacecraft monitoring the Sun and its atmosphere from different view points on the ecliptic plane.

We focused on relatively simple CME events, characterised by almost no rotation and deflection in their magnetic structure after the eruption, so that their evolution from the eruption site up to 0.1 AU could be considered approximately radial and self-similar. Both events were also observed as clear magnetic cloud (MC) signatures at 1 AU, making the comparison with simulation outputs easier as magnetic field rotations were smooth and easy to identify.

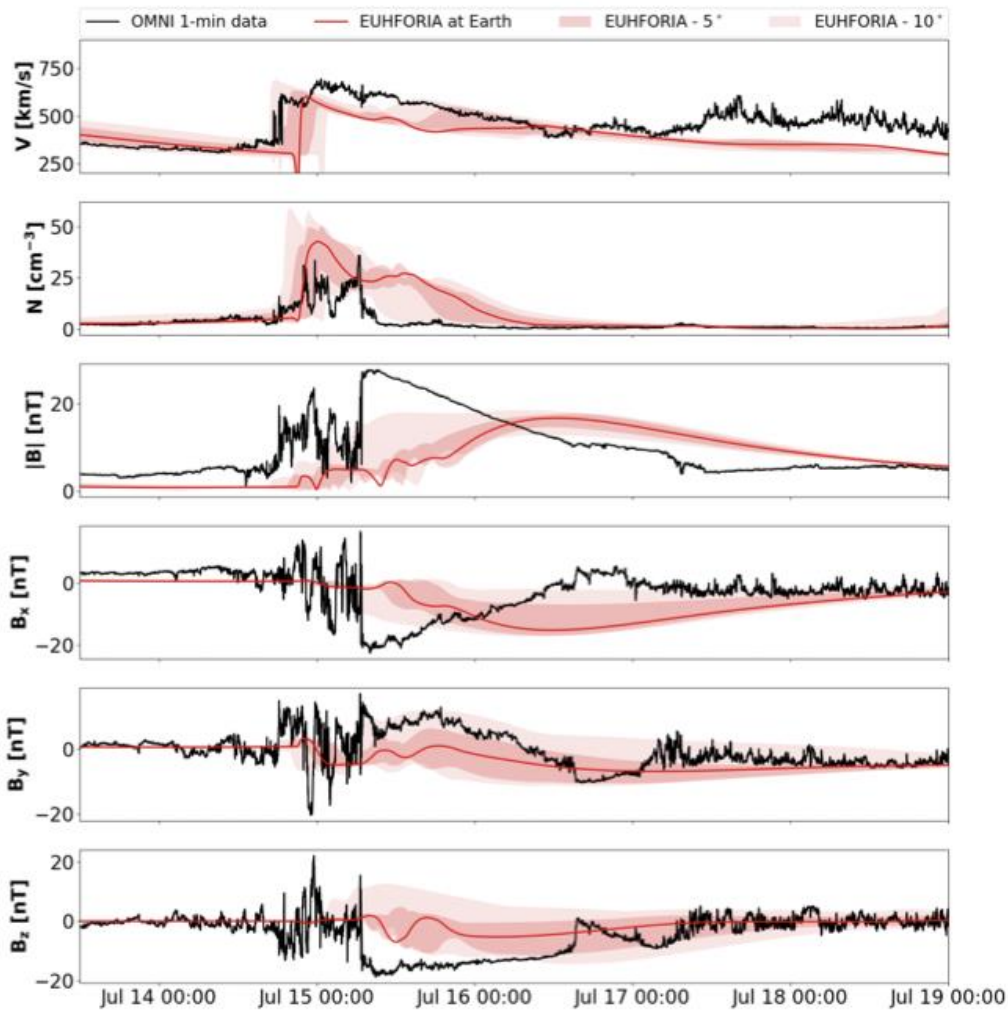


Figure 20

The comparison of the EUHFORIA time series (red curves) and in situ data (1 min OMNI data marked with black curve). The dark red and light red shaded areas show the maximum variation of EUHFORIA predictions at positions separated by 5° and 10° in longitude and/or latitude from Earth. *From top to bottom*: speed, number density, magnetic field strength, B_x , B_y , B_z components in GSE coordinates.

2. In this publication a new observational method was presented, based on GCS fitting outputs, to separate the radial and expansion speeds of CMEs (see also Section 4.2.1). Testing this method against empirical relations in the literature, we observed that single spacecraft observations and multi spacecraft observations provide quite different estimations of the CME expansion and radial speeds. On one side, the geometrical approach based on multi-spacecraft observations is based on 3D geometrical relations, and hence it is in principle more consistent with the geometry used in the coronagraphic reconstruction of the CMEs and in heliospheric simulations. On the other hand, it can only be applied to CME events that were observed from more than one view point, and it has not been tested yet on a large set of events, as is the case of the empirical relations considered here.

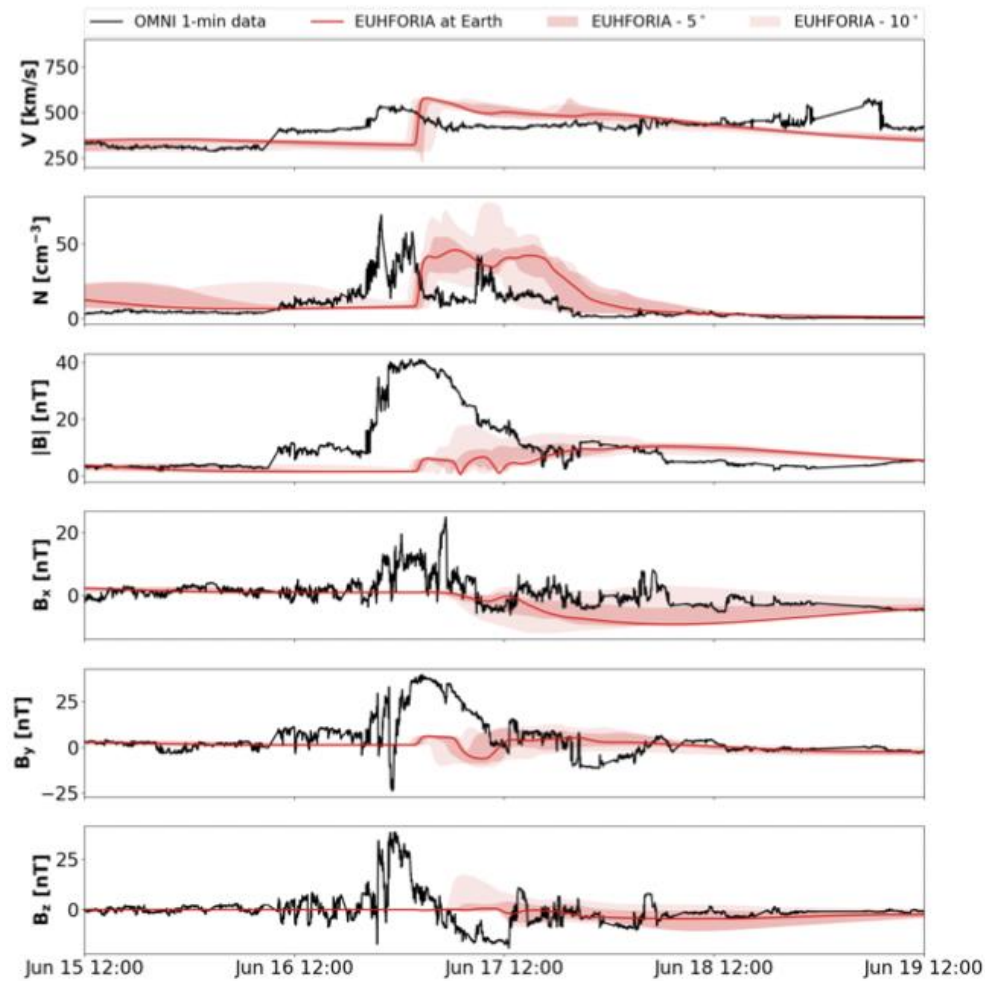


Figure 21

EUHFORIA time series at Earth compared to in situ data (1 min OMNI data marked with the black curve). The dark red and light red shaded areas show the maximum variation of EUHFORIA predictions at positions separated by 5° and 10° in longitude and/or latitude from Earth. From top to bottom: Speed, number density, magnetic field strength, B_x , B_y , B_z components in GSE coordinates.

Although additional testing would be needed in order to assess the performance of this approach in the case of a statistical set of CME events, the geometrical approach has two major additional strengths compared to the empirical ones: (1) it allows us to go beyond empirical relations that may work on large sets of events but may fail in single cases, and (2) it allows us to quantify the contribution of the expansion and radial speeds for any CME, and not only to those that were observed as full halos.

3. The separation of the radial and expansion speeds is critical in order to model the propagation of spheromak CMEs in the heliosphere and to predict their arrival time at Earth. The simulation results show that spheromak CMEs propagate significantly faster than cone CMEs when initialised with the same kinematic parameters. For both case studies, it was shown that those differences in the propagation can be mitigated by initialising spheromak CMEs at 0.1 AU using a reduced speed (v_{rad}) that considers only the radial motion of the CME centre of mass, instead of the combination of the radial and of the expansion motion of the CME apex ($v_{\text{rad}} + v_{\text{exp}}$). Based on further analysis of the simulation outputs, we interpreted these differences as the result of the different

Lorentz force acting on cone and spheromak CMEs (particularly at the CME-solar wind interface due to magnetic pressure gradients), which in turn leads to different CME expansions in the heliosphere.

4. Considering predictions of the peak ICME magnetic field parameters at Earth, results for presented case studies show that using the spheromak CME model improves the predictions of B (B_z) at Earth by up to 60 (40) percentage points for Event 1, and 12 (22) percentage points for Event 2, in comparison to the cone model. At the same time, the model predictions appear to be sensitive to the exact position sampled in the heliosphere. Considering virtual spacecraft separated by 5° and 10° in longitude and latitude from Earth, B (B_z) predictions improved significantly, reaching up to 70% (78%) of the observed peak value for Event 1, and 45% (58%) for Event 2. This provides an indication of the spatial variability of the predictions at 1 AU. As such separations are consistent with the typical uncertainties in the reconstruction of the CME direction of propagation from the GCS model, in the case of a background solar wind that is uniform at angles up to 10° around the Sun-Earth line, results obtained from virtual spacecraft around Earth can also be used as efficient alternative to otherwise time-consuming ensemble simulations of CMEs performed varying the CME direction of propagation.

5. In both studied events, the predicted magnetic field time series show very extended MC radial (temporal) signatures. That suggests that the spheromak model tends to overestimate the radial size of the CME at 1 AU, not fully accounting for global shape deformation effects such as pancaking. This was also visible in the time delay of the magnetic field peaks compared to observations. Extending the current CME model to include the possibility to introduce ellipsoidal spheromak CMEs could mitigate this effect, and is something that needs to be quantified in future study.

6. Event 1 (12 July 2012 CME) represents a well-understood CME event in terms of its solar, coronal, and heliospheric evolution, and it was associated with a successful prediction of the ICME magnetic properties using the spheromak CME model. Event 2 (14 June 2012 CME) on the other hand turned out to be a more complicated event than expected. In fact, it appeared to be a single non-interacting CME event considering its evolution along the Sun-Earth line (including its in situ signature characterised by a nicely rotating magnetic field structure), but it was actually associated with a CME-CME interaction occurring between the main CME and a previous CME that erupted from the same AR on 13 June 2012. The analysis and modelling of this event was per se already more complicated than that of Event 1. Moreover, Event 2 also provided an example of the limitations of the spheromak CME model in reproducing the global shape of flux-rope structures in the heliosphere. The simulations of CME2 using the latitude and half width derived from the GCS reconstruction predicted the CME to propagate almost completely south of the ecliptic, so that almost no magnetic field signatures associated to the ICME were predicted at Earth. On the other hand, in situ observations of the event show magnetic signatures compatible with an almost-central crossing of Earth through the flux-rope structure. A way to cope with such limitations and have a correct prediction of the magnetic field rotations observed at Earth is by launching the spheromak CME directly on the equatorial plane.

To summarize, this study was focused on Earth-directed CME events that were associated with clear MC signatures at Earth, with the aim of benchmarking the current EUHFORIA prediction capabilities in the case of well-observed CME events. Initial results indicate significant improvements in the predictions of the ICME magnetic field structures at Earth when using a more realistic spheromak CME model compared to a traditional cone CME model. However, most CME events are

more complex than the case studies presented in this work, either due to their interaction with other structures in the solar wind, including other CMEs, or due to the limited observations available. This particularly will become a critical issue in the next years as observations from the STEREO spacecraft will reduce towards the end of the mission, eventually preventing 3D reconstruction of CME events until the launch of new missions. Therefore, several efforts to assess the predictive capabilities of the EUHFORIA model in more complex scenarios are also needed. In particular, a detailed analysis of the EUHFORIA capabilities in modelling CME-CME interactions is addressed in the following Section 4.2.4.

4.2.4 Evolution of Interplanetary Coronal Mass Ejection Complexity: A Numerical Study through a Swarm of Simulated Spacecraft

This section presents mostly work published in Scolini et al. (2021).

In-situ measurements carried out by spacecraft situated in radial alignment are critical to advance our knowledge on the evolution of CMEs and their magnetic structures during propagation through interplanetary space. Yet, the scarcity of radially aligned CME crossings restricts investigations on the evolution of CME magnetic structures to a few case studies, preventing a comprehensive understanding of CME complexity changes during propagation. This study focuses on EUHFORIA simulations of CMEs interacting with different solar wind streams using the linear force-free spheromak CME. The novelty of the approach lies in the investigation of the evolution of CME complexity using a swarm of radially aligned, simulated spacecraft. Our scope was to determine under which conditions CMEs exhibit variations of their magnetic structure and complexity during propagation, as measured by spacecraft that are radially aligned.

The first results indicate that the interaction with large-scale solar wind structures, and particularly with stream interaction regions, increases the probability to detect an increase of the CME magnetic complexity between two spacecraft in radial alignment, compared to cases without such interactions.

4.2.4.1 Identification and Classification of CME Structures and about the Spheromak Magnetic Structure

At each virtual spacecraft, the start of the CME-driven perturbation i.e., a shock-like discontinuity is determined through our algorithm by scanning the radial speed, density, and magnetic field time series forward in time and applying conditions similar to those typically used to detect fast-forward interplanetary shocks at 1 AU. The detailed identification criteria can be found in Appendix B.1 of Scolini et al. (2021).

At locations where a CME-driven perturbation is detected, time series are scanned in order to assess whether there is a magnetic ejecta (ME) after the shock-like discontinuity. The exact criteria used to determine the ME start and end times vary with heliocentric distance and for different solar wind regimes. However, they are in overall based on two typical characteristics of Mes, i.e., an enhanced magnetic field strength, and a low plasma β compared to the surrounding solar wind. After having identified the nominal boundaries of the in situ CME substructures (i.e., sheath, ME) at each virtual spacecraft, we classify the ME signature using a classification scheme inspired by Nieves-Chinchilla et al. (2019) and based on the amount of rotation of the magnetic field components, i.e., B_R , B_T , and B_N ,

in the local radial-tangential-normal coordinate system. This analysis provides information on the ME structure that is later used in the study on how CME complexity varies with distance, for various propagation scenarios. Because our simulations employ a spheromak magnetic structure for which rotations $>180^\circ$ are expected for a large variety of spacecraft crossings (as shown in Appendix A), we have adapted the original classification to better distinguish rotations up to 360° . We also further assign a numerical index (C) to each ME class in order to rank the level of complexity of the detected structure. If an ME is detected at a spacecraft located at coordinates (r, θ, f) , the defined classification scheme is applied (see Scolini et al. 2021).

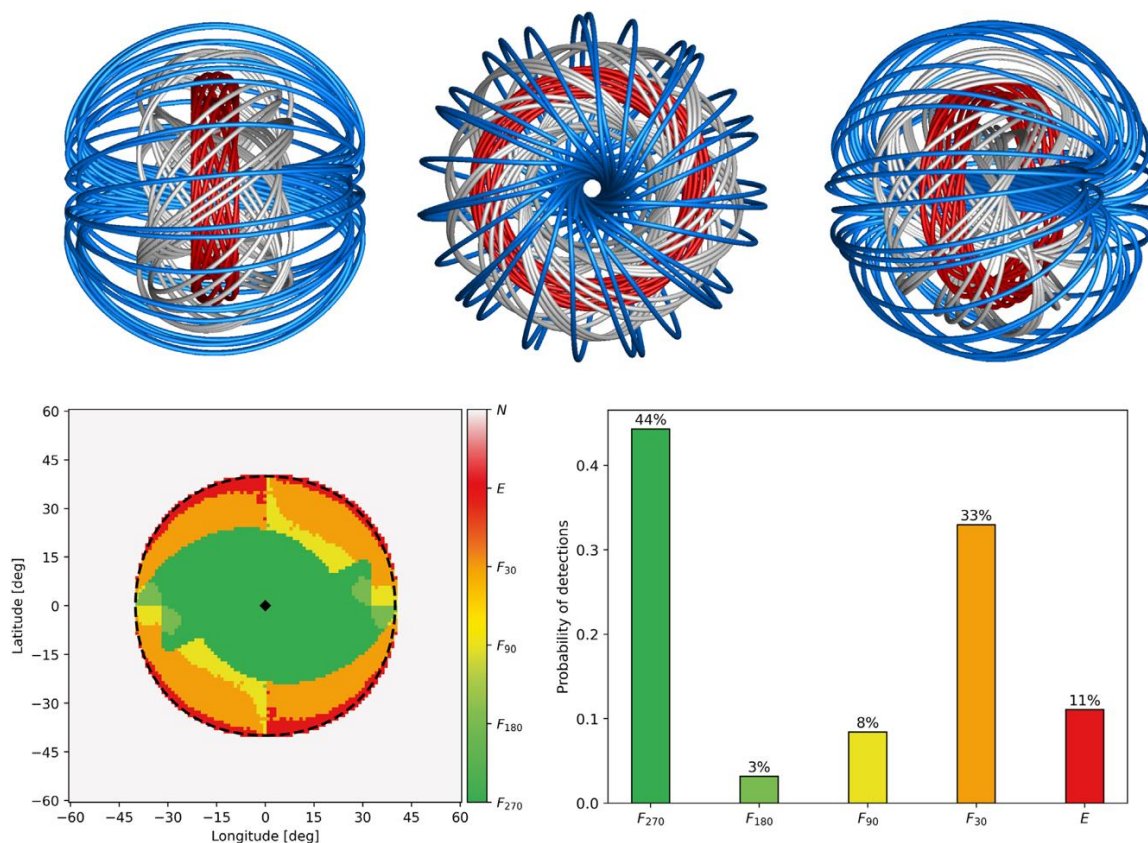


Figure 22

Spheromak magnetic structure used in EUHFORIA simulations.

Top: 3D visualization of selected magnetic fields from three perspectives: front view (a), side view (b), angled view (c). Different colors mark field lines characterized by different morphologies.

Bottom: (d): Longitude–latitude 2D map showing the spatial distribution of the ME signature classifications, obtained by radially crossing the structure at various impact angles. (e): Probability to detect the different ME signatures considering all possible radial crossings throughout the structure. (Adapted from Scolini et al. 2021.)

Starting from the ME nominal boundaries, the ME start and end times are varied by $\pm 25\%$ of the total ME duration, in order to assess the variability of the classification with respect to slight variations of the boundaries. The final ME classification is chosen as the most probable classification obtained among all possible combinations of boundaries. We included two additional categories representing the non-detection of an interplanetary shock-like perturbation (N), and the detection of an interplanetary shock-like perturbation, which was not followed by a ME (S). In these cases, we do

not assign a complexity index to the observed signatures because of their intrinsically different nature compared to ME signatures. We tackle the known limitations of the spheromak model in reproducing CME global magnetic structures by focusing the investigation of CME magnetic complexity to central regions only.

An overview of the nominal, standalone magnetic field structure of the linear force-free spheromak model used in the two set of modeling rounds and without accounting for any interaction with the solar wind is presented in Fig. 22. As visible from panels (a)–(c), all magnetic field lines are confined within a spherical surface. Panel (a) provides a frontal view of the structure, similar to the one that would have been seen by an observer located near the ecliptic plane along the Sun–Earth line in run A before the insertion of the CME into the heliospheric domain. Panels (b) and (c) provide additional side and angled views of the magnetic structure.

By crossing the spheromak structure in the radial direction at various impact angles (varying the crossing directions by $\Delta\vartheta = \Delta f = 1^\circ$ incremental steps) and calculating the rotations of the magnetic field components along each direction, we generate a longitude–latitude 2D spatial distribution map of the ejecta classifications. The distribution is symmetric with respect to the spheromak main axis, oriented along the equatorial plane, and is dominated by a central core of F_{270} ejecta types surrounded by F_{30} classifications in the north and south flank regions. Minor contributions from F_{180} and F_{90} types are visible in the core-to-flank transition region, while E types are detected only by crossings at the very edge of the structure. In the panel (e) we present the probability to detect the different ME types over the totality of crossings considered. The detection probability is highest for F_{180} (44%) and F_{30} (33%) types, and significantly lower for the remaining types (11%, 8%, 3% for E , F_{90} , F_{180} types, respectively).

4.2.4.2 Discussion and conclusions

The main scope of this study was determining under which conditions and to what extent CMEs exhibit variations of their magnetic structure and complexity during propagation through interplanetary space.

- We had to restrict to the central part of the CME structure in order to limit the effect of known limitations arising from the use of a spheromak CME model.
- From the comparative analysis of non-interacting/interacting scenarios, distinct evolutionary behaviors characterizing CMEs propagating through different ambient conditions have emerged. Our results provide evidence that the interaction with such structures, and particularly with SIRs, can double the probability for a CME to increase its magnetic complexity during propagation. This result is independent from the CME impact angle, suggesting that the detection of complexity changes is likely an indication of interactions with other structures, rather than the result of a crossing far from the CME center. The present work provided first evidence that CME structures propagating through different solar wind backgrounds develop different complexity evolutionary patterns, based on numerical simulations employing a spheromak flux-rope model.
- Another way to look at the development of CME magnetic complexity during propagation involves consideration of the coherence of the magnetic structure as a function of heliocentric

distance and in our simulations, we find that the Alfvén speed in the ME at 1 AU is about 120 km/s (~97 km/s). The higher Alfvén speed retrieved in run A may indicate a more coherent evolution of the ME structure than in run B, in agreement with our results of the complexity changes.

- This work represents the first attempt to quantify complexity changes in CME magnetic structures using numerical simulations. Our simulations assumed very idealized solar wind conditions and did not include any latitudinal dependence of its properties, enabling us to quantify the effect of the presence of a HSS and SIR on CME complexity, and the comparability of different runs. Therefore, the results presented here shall be interpreted as lower limits, as ubiquitous distortions of the local solar wind properties are likely to induce higher complexity changes in real CMEs both in the absence and presence of SIRs along their path. Investigations exploring a broader range of CME–solar wind interactions, the spatial dependence of CME complexity and its changes, and the comparison with observations for real events, will be explored in future studies.
- Our results shed new light on the evolution of CME magnetic structures, helping the identification and interpretation of CME conjunction observations involving both past and current missions (such as Parker Solar Probe, Solar Orbiter, and BepiColombo), and providing guidelines for the planning of future missions involving alternative alignment configurations.

4.2.5 Modelling a multi-spacecraft coronal mass ejection encounter with EUHFORIA

This section presents mostly work published in Asvestari et al. (2021).

In this study we employed the spheromak CME model to reconstruct a well observed CME and compare model output to in situ observations. We focus on an eruption from 6 January 2013 that was encountered by two radially aligned spacecraft, Venus Express and STEREO-A. We first analysed the observed properties of the source of this CME eruption and we extracted the CME properties as it lifted off from the Sun. Using this information, we set up EUHFORIA runs to model the event. The EUHFORIA predicted arrival times from half to a full day ahead of the in situ observed ones, but within errors established from similar studies. In the modelling domain, the CME appeared to be propagating primarily southward, which is in accordance with white-light images of the CME eruption close to the Sun.

In order to get the observed magnetic field topology, we aimed at selecting a spheromak rotation angle for which the axis of symmetry of the spheromak is perpendicular to the direction of the polarity inversion line (PIL). The modelled magnetic field profiles, their amplitude, arrival times, and sheath region length are all affected by the choice of radius of the modelled spheromak.

4.2.5.1 About the methods and analysis

To determine the helicity sign of the magnetic field structure of the CME, we investigated observational proxies for determining the helicity sign using remote-sensing imaging observations (Chen et al. 2014; Palmerio et al. 2017)

The filament was visible for several days before the eruption. On 27 December 2012, it was within the field of view of Earth and, therefore, we used SDO/HMI magnetograms to analyse its magnetic field topology. The photospheric magnetic field is positive to negative from the solar east to

the solar west, with the filament lying above the PIL (top left panel in Fig. 23). We note that $H\alpha$ images (Fig. 23, top right corner) show that the orientation of the filament barbs (marked with arrows) relative to the filament axis along the PIL indicate a sinistral, positive helicity, flux rope. STEREO-A EUV images (bottom panels) of the post eruption arcade (PEA) show the flaring arcades being right-skewed in comparison to the underlying magnetic PIL. This supports the positive helicity sign indicated by the pre-eruption signatures of the filament.

Figure 24 shows illustrative magnetic field lines for two different orientations of the spheromak together with the direction of the PIL and filament in the corona indicated by the magenta dashed line. In this study, we selected the rotation angle according to panel b. With this choice, the axis of symmetry of the spheromak is perpendicular to the direction of the PIL. The choice is motivated in order to obtain magnetic field rotation (blue field lines) consistent with the observationally inferred magnetic field structure. It is important to note, however, that the maximum of the field strength occurs along the axis of symmetry in the spheromak. We also performed model runs using the rotation indicated in panel a and confirmed that incorrect rotation of the magnetic field vectors was obtained.

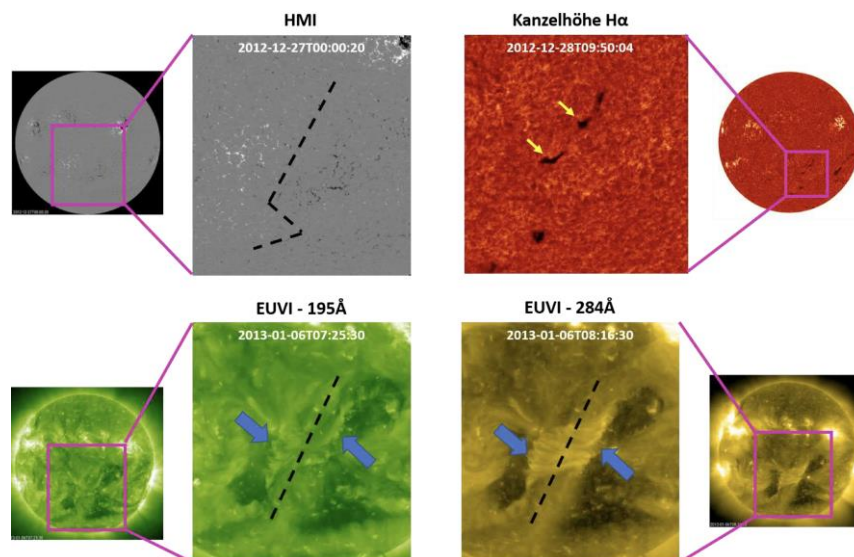


Figure 23

Filament and post-eruption characteristics used in identifying the flux rope helicity sign. The images in the top left corner show the magnetic field topology at the HMI magnetogram a few days prior to the eruption. The black line marks the PIL. In the top right corner there are $H\alpha$ images of the Sun taken with the solar telescope at Kanzelhöhe Solar Observatory and compensated for limb-darkening following the method by Chatzistergos et al. (2018). Barb structures are indicated with yellow arrows. The STEREO-A EUVI filtergrams at 195 Å and 284 Å (left and right images in the bottom row, respectively), show the post-eruption arcade and flare ribbons. The latter is indicated by blue arrows in the bottom row zoomed images, while the black dashed line indicates the PIL. (Adapted from Asvestari et al. 2021.)

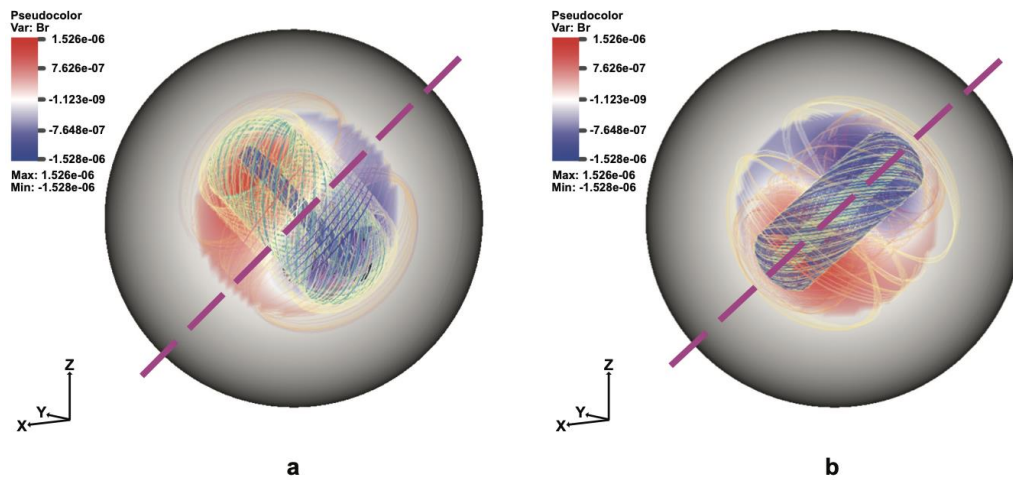


Figure 24

Magnetic field topology of the modelled spheromak CME based on the selected tilt. *Left*: magnetic structure for the case when injecting a spheromak with a tilt value obtained from the GCS fitting. *Right*: spheromak with rotation angle equal to the tilt increased by 90 degrees anticlockwise. The magenta dashed line marks the orientation of the observed filament and thus the GCS tilt. (Adapted from Asvestari et al. 2021.)

4.2.5.2 Discussion and results

In this study, we analysed a multi-spacecraft CME encounter in order to investigate whether the EUHFORIA model can reconstruct the evolution of the flux rope observed by two radially aligned spacecraft. The event, an extended filament eruption that occurred on 6 January 2013, created clear in situ signatures at Venus Express and STEREO-A, while it only produced a mild disturbance at MESSENGER. The location of the eruption did not allow for information about the magnetic flux content of the CME to be extracted. However, EUV and white-light images allowed for the determination of the eruption time and the CME helicity sign, as well as the extraction of kinetic and geometric parameters of the large-scale structure using the GCS model. Although two more eruptions occurred close to the event under study, we deduced from the analysis of an observational and from a modelling assessment that neither of these eruptions significantly interfered with the primary event in this study. The CME was modelled using three different sets of parameters. The three simulation runs were done for different radii for the spheromak ($R_{\omega\text{EO}}$, $\langle R \rangle$, and $R_{\omega\text{FO}}$). Based on the orientation of the PIL and spheromak, we justified that it is necessary to rotate the spheromak by 90 degrees anticlockwise from the GCS-derived tilt, and we submitted the runs using this modified tilt. The main conclusions of the observational and modelling analysis are as follows.

1. Magnetic field and plasma measurements by Venus Express and STEREO-A suggested that the observed CME did not significantly evolve between the two spacecraft measurements.
2. Remote-sensing observations indicated a direction of propagation pointing southward.
3. Matching the GCS fitted structure to that of the spheromak used in EUHFORIA is not unique and can be difficult, introducing different possibilities reflecting the fact that the magnetic field structure is not directly manifested in the white-light emission and thus poorly constrained.

4. The radius of the modelled spheromak had an impact on the modelled magnetic field profiles and their amplitude, the arrival times, and the distance between the shock and the flux rope arrival.
5. Similarly to what was indicated by the white-light images, the model showed that the direction of propagation of the CME was mainly southward. The modelled time series at the real spacecraft locations did not fully agree with the in situ measurements, while virtual spacecraft placed at the same radial distances but lower in latitude showed better agreement to the in situ observations. The same holds true for a longitudinal displacement further east relative to the Sun–Venus Express–STEREO-A line. This suggests that a better agreement between observations and modelled result is found in these areas.
6. One possible explanation is that the observed CME underwent deflection from its initial course in the inner heliosphere (Zuccarello et al. 2012). The possibility of pancaking of the CME, which would have resulted in flattening and stretching, and which are not modelled by the simulation, may also be a contributing factor. In this case, despite a more southward propagation of the CME, the flux rope could still have been stretched to higher latitudes, resulting in a more nose encounter of the CME with the two spacecraft. This would be in accordance with the in situ signatures that indicate an encounter closer to the nose. This kind of effect would not have necessarily been captured by EUHFORIA, at least not to a full extent especially if the front flattening took place before 0.1 AU.
7. The predicted arrival times are well ahead of the ones extracted from the in situ signatures but within errors previously established from other studies and possibly a result of both the propagation and the expansion speed being included in the GCS fitting approach.

The aim of this study was to assess the degree to which the EUHFORIA–spheromak model is able to capture the evolution of CMEs in the context of multi-spacecraft encounters. Although there were some unexpected inaccuracies in the output, we conclude that the model predicted the B -field and most importantly the B_z -component at the nose of the CME well, which appeared to have been encountered in situ by Venus Express and STEREO-A. This is of crucial importance when studying Earth-directed CMEs.

4.3. Tracking CME-driven shock waves using radio observations

Modeling of the shock waves with EUHFORIA was a challenging task as the CME models of EUHFORIA had the CME insertion at the height of 0.1 AU, when the CME-driven shock, in the majority of cases is already formed. Thus, preliminary studies were done for implementing different coronal models that would allow us to model the shock already in the low corona. Our results show that the CME-driven shock waves can be modelled by EUHFORIA, but the stand-off distance between CME and the shock is modeled well only at close-to 1 AU distances.

In the framework of CCSOM project several papers were published addressing the physics of shock waves and modeling their propagation. Herein, we will address some results from several related publications. For all related publications see the reference list.

Studying the shock waves using radio observations (Palmerio et al. 2019; Magdalenic et al. 2020; Morosan et al. 2020; Mann et al. 2022), and tracking them using radio triangulation resulted in

important scientific findings (Jebaraj et al. 2020). We modeled the CME-driven shock waves and associated radio emission (Kouloumvakos et al. 2020, 2021; Jebaraj et al. 2021) employing the Magneto-Hydrodynamic Around a Sphere Thermodynamic model (Lionello et al. 2009; Riley et al. 2011). The recommendation is to implement in EUHFORIA coronal models which include the CME insertion in the low corona.

4.3.1 Coronal Conditions for the Occurrence of Type II Radio Bursts

This section presents mostly work published in Kouloumvakos et al. (2021).

Type II radio bursts are generally observed in association with flare-generated or coronal-mass-ejection-driven shock waves. The exact shock wave and coronal conditions necessary for the production of type II radio emission are still under debate. Shock waves are important for the acceleration of electrons necessary for the generation of the radio emission. Additionally, the shock geometry and closed field line topology, e.g., quasi-perpendicular shock regions or shocks interacting with streamers, play an important role for the production of the emission. In this study we perform a 3D reconstruction and modeling of a shock wave observed during the 2014 November 5 solar event. We determine the spatial and temporal evolution of the shock properties and examine the conditions responsible for the generation and evolution of type II radio emission. Our results suggest that the formation and evolution of a strong, supercritical, quasi-perpendicular shock wave interacting with a coronal streamer were responsible for producing type II radio emission. We find that the shock wave is subcritical before and supercritical after the start of the type II emission. The shock geometry is mostly quasi-perpendicular throughout the event. Our analysis shows that the radio emission is produced in regions where the supercritical shock develops with an oblique to quasi-perpendicular geometry.

4.3.2 Some conclusions

In this study we modeled a shock wave associated with a solar event and a complex type II radio burst. We performed a detailed comparison between the shock model and the radio observations in the metric and decametric range. Our key findings can be summarized as follows:

1. We show that the shock formation precedes the start of the type II radio burst; however, the shock wave is then subcritical and electron acceleration is at that time too weak to produce radio emission.
2. We show that the start of the type II radio burst occurs about when the shock becomes supercritical. The early intense phase of the type II burst occurs when the shock is mostly confined to closed field regions. This likely explains why no escaping energetic electrons are observed as additional type III emissions. Part of the shock wave interacts with a streamer, and the shock geometry is mostly quasi-perpendicular at this time.
3. We show that type II radio emission most probably originates, throughout the event, from regions where the shock wave is strong and supercritical, with relatively high density compression ratio and quasi-perpendicular geometry (high ϑ_{BN}). This strongly supports the notion that shock drift acceleration generates the electron beams that are ultimately responsible for type II radio emission. A comparison between the shock model and the radio

observations from NRH confirms that the radio sources are situated near strong shock regions with oblique to quasi-perpendicular shock geometry.

4. The evolution of the shock wave inside a streamer seems to play a very important role in the enhancement of the shock strength and the formation of a supercritical shock. Most importantly, we find that this condition will favor the efficient electron beam acceleration by the shock and the production of type II radio emission.

For more details on this study see Kouloumvakos et al. (2021).

4.3.3 Using radio triangulation to understand the origin of two subsequent type II radio bursts

This section presents mostly work published in Jebaraj et al. (2020) & Jebaraj et al. (2021).

Eruptive events such as CMEs and flares accelerate particles and generate shock waves which can arrive at Earth and can disturb the magnetosphere. Understanding the association between CMEs and CME-driven shocks is therefore highly important for space weather studies. Herein we present a study of the CME/flare event associated with two type II bursts observed on September 27, 2012. The aim of the study is to understand the relationship between the observed CME and the two distinct shock wave signatures.

The multiwavelength study of the eruptive event (CME/flare) was complemented with radio triangulation of the associated radio emission and modelling of the CME and the shock wave employing MHD simulations by EUHFORIA.

We found that, although temporal association between the type II bursts and the CME is good, the low-frequency type II (LF-type II) burst occurs significantly higher in the corona than the CME and its relationship to the CME is not straightforward. The analysis of the EIT wave (coronal bright front) shows the fastest wave component to be in the southeast quadrant of the Sun. This is also the quadrant in which the source positions of the LF-type II were found to be located, probably resulting from the interaction between the shock wave and a streamer.

The relationship between the CME/flare event and the shock wave signatures is discussed using the temporal association, as well as the spatial information of the radio emission. We also discuss the importance and possible effects of the frequently non-radial propagation of the shock waves.

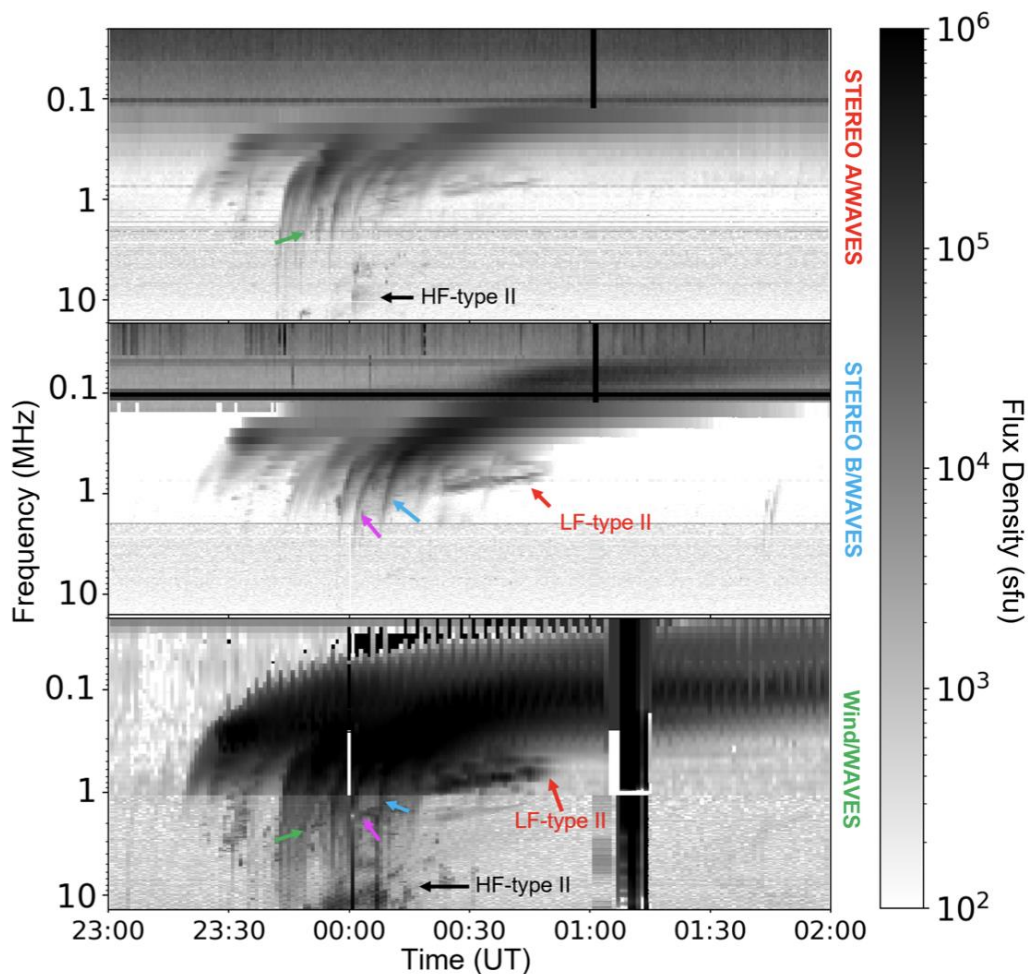


Figure 25

Calibrated dynamic radio spectra (solar flux units, i.e. *sfu*) observed by the Wind/WAVES, STEREO A/WAVES, and STEREO B/WAVES show the radio event associated with the September 27/28 event flare/CME. The LF-type II, i.e. the low frequency type II burst (indicated by the red arrow), observed by all three spacecraft, shows fundamental and second harmonic emission lanes. The HF-type II, i.e. the high frequency type II burst, which is indicated by the black arrow was best observed by Wind/WAVES. The flare impulsive (FI) type III group (marked by the green arrow) and the type III associated with the flare decay (FD and FD*) phase are indicated by the blue and pink arrows, respectively. (Adapted from Jebaraj et al. 2020.)

4.3.3.1 Shock waves signatures in radio observations

The shock waves associated with eruptive events can manifest via a variety of signatures. Chromospheric Moreton waves, EIT waves (coronal bright fronts associated with solar eruptions; see e.g. Zhukov & Auchère 2004, and references therein), and type II radio bursts (Fig 25) are often considered to be signatures of the same shock wave propagating in the solar corona (e.g. Warmuth et al. 2004; Vršnak et al. 2006).

This study is focused on type II radio bursts which are the longest known signatures of shock waves in the solar corona, and are also excellent means for tracking the shock wave propagation (e.g. Wild & McCready 1950; Klassen et al. 1999; Magdalenic et al. 2012)

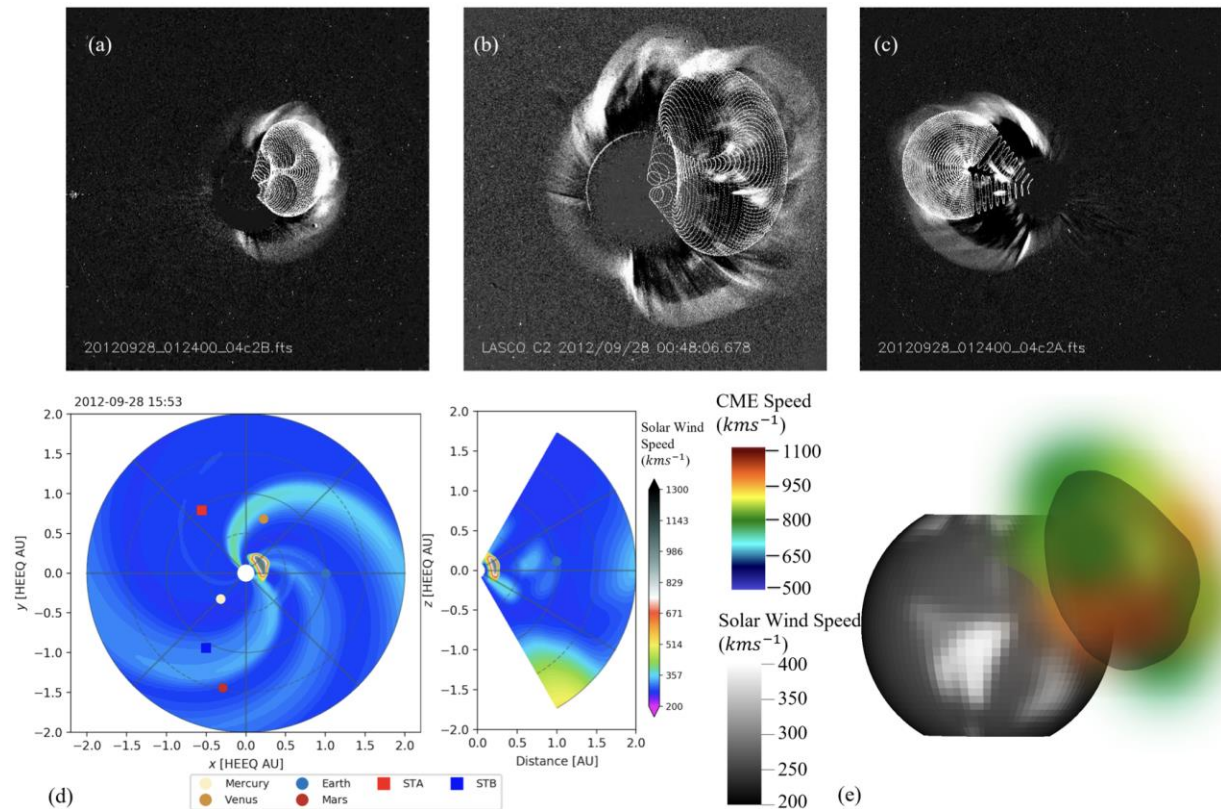


Figure 26

Panels a–c: graduated cylindrical shell (GCS) reconstruction of the CME body. Coronagraph images from: (a) STEREO B/COR 2, (b) SOHO/LASCO C3, and (c) STEREO A/COR 2 at roughly the same time (September 28, 2012 at 01:24 UT).

Panels d and e: CME modelled by EUHFORIA. (d) Propagation of the modelled cone CME in the ecliptic and meridional perspectives. (e) CME speeds at the cone surface as seen from Earth. The grey sphere shows the solar wind radial velocity at the inner boundary of EUHFORIA. (Adapted from Jebaraj et al. 2020.)

We employed EUHFORIA model to analyse the CME propagation. The simulations were performed using the EUHFORIA v1.0.4 version of the model (Hinterreiter et al. 2019) The CME parameters such as the half width, direction of propagation (longitude and latitude), and 3D speed obtained from the GCS reconstruction were used as input for the cone CME model. The obtained results are presented in Fig. 25.

4.3.3.2 Summary of findings on the origin of type II radio bursts

The relationship between CME/flare events, shocks, and associated type II radio bursts has been extensively discussed for several decades (e.g. Cairns et al. 2003, and references therein). This study brings some new and important findings on the association of the radio emission and solar eruptive phenomena.

Bellow, we list the most important results:

- Radio triangulation studies of type III bursts have been performed in the past, but we show for the first time that the source positions of type III bursts observed during a single eruptive event were located in significantly different locations. We find that the FI-type III bursts (observed during flare impulsive phase) originate from close to the western CME-flank region,

and the FD-type III bursts (observed during the flare decay phase) originate from close to the eastern CME-flank region (Figs. 25 and 27.).

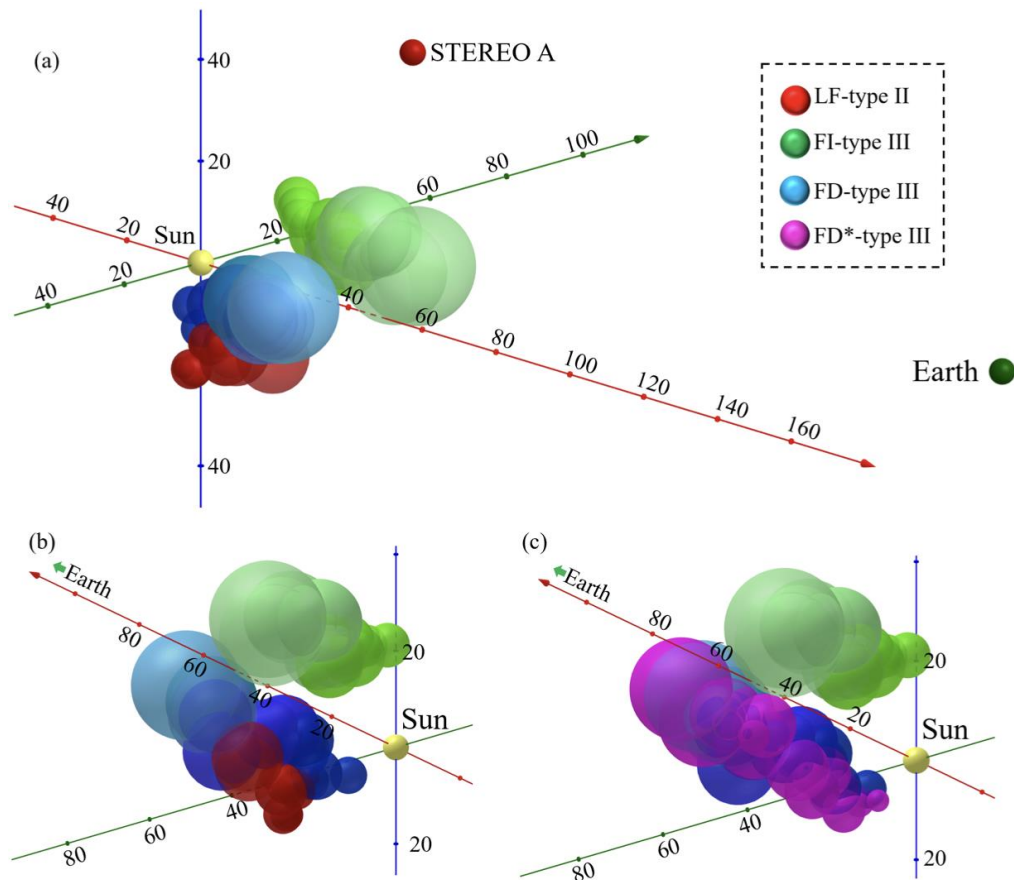


Figure 27

Panel a: Results from radio triangulation studies of type II and type III radio bursts. The yellow sphere represents the Sun, while the red and green spheres represent STEREO A, STEREO B and Wind, respectively. The spheres of varying size represent the radio source regions. The green spheres mark the radio source positions of the FI-type III close to the CME flank. The LF-type II and the FD-type III, denoted by the red and blue spheres, have source positions at the southeast side of the Sun, i.e. close to another CME flank. Panel b: FI-type III, FD-type III, and LF-type II plotted from a different perspective. Panel c: three different type IIIs plotted together. (Adapted from Jebaraj et al. 2020.)

- We find the propagation path of two subsequent type III bursts are very similar (FD- and FD*-type III, Fig. 27), with differences smaller than the source region sizes (i.e. distance between two wave vectors). We do not find any significant difference in the source positions for the same frequency pairs for these two bursts, which would be expected if the scattering processes in this event were significant. The accuracy of the radio triangulation is therefore within the limits induced by the radio triangulation method.
- One of the two type II bursts (HF- and LF-type II, Figs.25 and 27.) associated with the studied event, the LF-type II, starts at an unusually low frequency. We find that the LF-type II was associated with the interaction of the shock wave and a streamer region. Although appearing

at very different parts of the CME (different flanks), both of the type II radio bursts seem to be driven by the CME.

- The radio triangulation study of the LF-type II burst provides evidence of the strongly non-radial propagation of the radio sources. Although this has already been discussed previously (e.g. Bougeret 1985, and references therein), only the 3D information obtained in the radio triangulation allows us to quantify the effects associated with the non-radial propagation.
- The coronal electron densities obtained in the present radio triangulation study show that all radio bursts in this event are generated in the regions of higher density than what is usually considered when employing 1D density models. This is to be expected in particular during periods of high solar activity and at times when the global magnetic field of the Sun is very complex. Therefore, employing the 1D density models for explaining radio emission should be considered with great care, and only as a first level approximation.
- The EIT wave associated with the eruptive event accelerates (from 320 to 770 km/s) when passing a nearby active region, in the direction roughly coinciding with the propagation direction of the LF-type II. The reconstructed dome

Radio triangulation is not dependent on a density model and therefore provides a unique opportunity to study different aspects of the radio bursts and their association with the solar transients. The radio emission can be influenced in different ways during its propagation through the corona, and this will also affect the results of the radio triangulation. Therefore, as with all other observations, gonipolarimetric observations need to be treated with care, and their limitations must be taken into account. Nevertheless, direction finding observations provide unique information on the 3D positions of the radio emission, and can help us to understand the processes of radio emission during eruptive events in an unprecedented way.

4.3.3.3 Generation of interplanetary type II radiation and shock wave modelling

After understanding the origin of type II radio bursts observed on 27 September 2012, we focus our study to isolate and understand the shock wave properties necessary for accelerating electrons and leading to the production of the radio emission.

First, we modelled the 3D expansion of the shock wave by exploiting multi-viewpoint reconstruction techniques based on extreme ultraviolet imaging. The physical properties of the shock front were then deduced by comparing the triangulated 3D expansion with properties of the background corona provided by a 3D magnetohydrodynamic model. The radio triangulation technique provided the location of radio source on the surface of the modelled wave in order to compare radio sources with the shock properties. Study of the temporal evolution of the shock wave parameters and their role in the generation of radio emission shows a close relationship between the shock wave strength and its geometry. We deduce from this analysis that there may be several mechanisms at play that generally contribute to the generation of radio emission. Further, the comparison between the reconstructed sources of radio emission and the ambient shock wave characteristics reveals the complex relationship between shock parameters and show how they can influence the morphology of the observed type II radio emission.

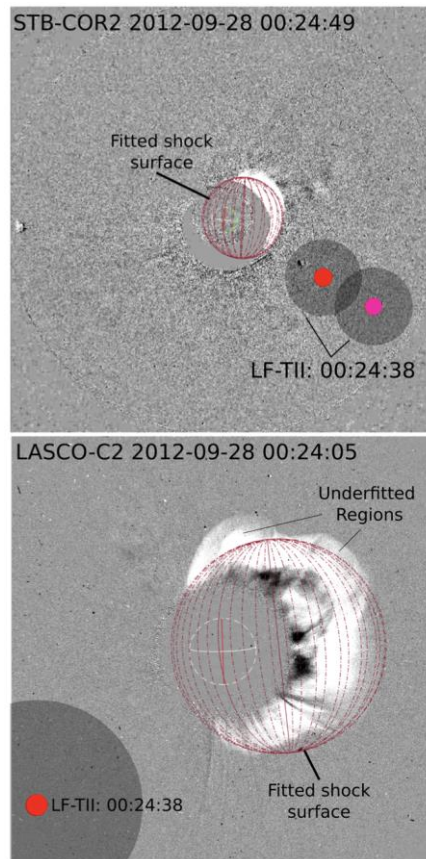


Figure 28

Shock wave fitting was done using multi-viewpoint observations from STEREO B/COR2 (*top panel*) and SOHO/LASCO C2 (*bottom panel*) at 00:24 UT. This is the time of observation of the highest triangulated frequency pair of the LF-type II burst. The red spherical mesh represents the fit to the white light shock. The regions indicated as underfitted are the regions that are not accounted for in the shock wave modelling. The red and the fuchsia points are the centroids of the highest frequency LF-type II sources and the dark-shaded region is the full source region obtained from radio triangulation. (Adapted from Jebaraj et al. 2021.)

A) Shock wave modeling

In order to study the association of the shock wave characteristics and generation of the type II radio burst we modelled the shock wave. Details of the applied model are presented in Rouillard et al. (2016) and Kouloumvakos et al. (2019). An example of the model application with the aim to explain the generation of the low coronal shock signatures (i.e. metric wavelength type II) was presented in Zucca et al. (2018) and Kouloumvakos et al. (2021). The model of the shock wave used in this study combines 3D shock reconstruction employing white light observations with the static MHD simulations, allowing us to calculate the shock kinematics and the shock parameters in the 3D space. We start with the 3D reconstruction of the observed pressure wave. The wave reconstruction is performed using the multi-viewpoint EUV and white-light observations of STEREO (EUVI at 195 Å, COR1, and COR2), SOHO (LASCO C2 and C3), and the 193 Å channel of SDO/AIA. An example of the reconstructed wave surface is presented in Fig. 28. This reconstruction allows us to model the wave in 3D space and calculate the speed along the entire wave front and along different propagation directions. The wave modelling was done with a temporal resolution of one minute.

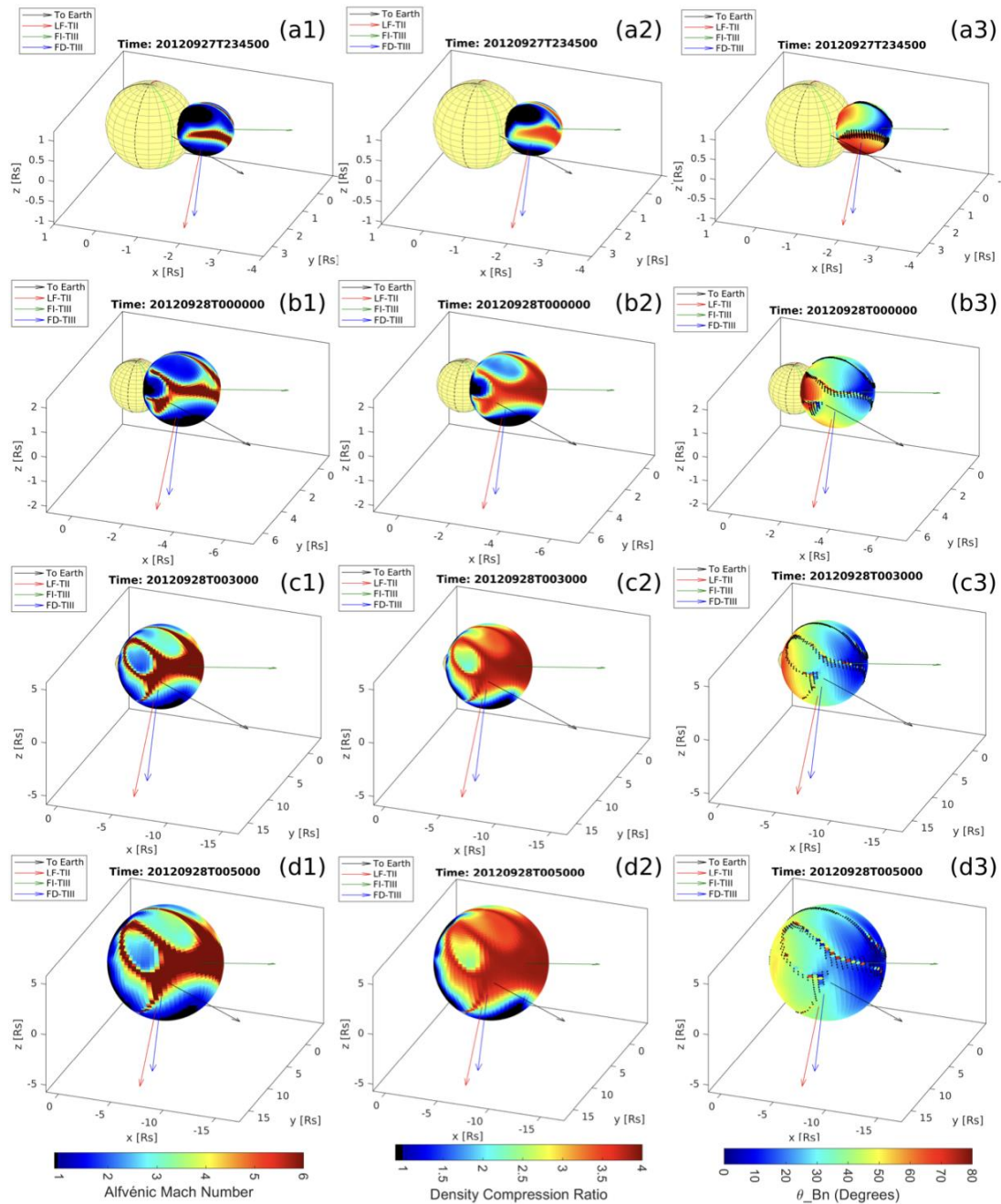
We note that in the case of geometric reconstruction of the pressure wave, the assumed self-similar expansion in the lateral directions will limit the accuracy of the modelled wave. The modelling errors will be considerable for events where the shock wave is strongly asymmetric. Our reconstruction was rather conservative in some directions, resulting in some under-fitting in the lateral regions (e.g. the regions labelled in Fig. 28). Nevertheless, we expect that in the regions of interest, the wave fitting was rather accurate. We estimate that the uncertainty in the reconstructions based on white light can be about $1 R_{\odot}$, at heights above $5 R_{\odot}$.

Once the pressure wave was reconstructed, we used the magnetic field and plasma properties of the solar corona provided by the Magneto-Hydrodynamic Around a Sphere Thermodynamic (MAST) model (Lionello et al. 2009; Riley et al. 2011) to determine the properties of the expanding wave. The shock parameters such as Mach number (M_A), compression ratio, and shock geometry (ϑ_{BN}) were then computed on the surface of the modelled pressure wave. This technique provides the properties of the pressure wave from the onset of the eruption in the low corona until the time when the observation of the LF-type II radio burst is stopped. We investigated the conditions on the surface of the pressure wave and its association with both the HF and LF-type II radio bursts. The source positions of HF-type II burst were approximated using intensity-directivity relationship and the LF-type II burst source positions were estimated employing the radio triangulation technique (Jebaraj et al. 2020).

B) Shock wave parameters in 3D

First, we analyzed the 3D evolution of the modelled pressure wave, starting at about 23:45 UT, when the wave was in the low corona and when the first shock wave signatures were observed in dynamic spectrum (Fig. 25). In Fig. 29, we show a series of snapshots of the modelled pressure wave. The colours present different shock parameters computed on the surface of the expanding pressure wave using the upstream MHD variables obtained from the MAST model. The combination of the three parameters plotted in Fig. 29 (arranged in columns) enables us to locate the regions where the shock wave was most likely to be formed and it gives a good indication on the generation of the type II radio emission. Panels a to d in show snapshots of the modelled pressure wave at four different times selected for a detailed analysis. The times are selected in such a way to correspond with the different phases of the wave propagation and subsequent production of type II radio bursts.

Figure 29 row a shows the modelled wave at 23:45 UT which corresponds to the onset of the HF-type II radio burst (23:43 UT). The fundamental component of the HF-type II was observed at 28 MHz which is approximately $1.9 R_{\odot}$ from the solar surface (when considering 3.5-fold Saito density model, Saito 1970). The starting frequency of the HF-type II radio burst indicates that radio emission was formed higher up in the solar corona opposed to the metric type II radio bursts associated with low-coronal shock wave.


Figure 29

Snapshots of the modelled shock wave parameters at different times (*a–d*) and with different parameters estimated at the reconstructed pressure wave front surface (1–3). The yellow sphere represents the Sun and the colour coded ellipse represents the modelled pressure wave. The arrows indicate the propagation direction of the different triangulated radio bursts, while the black arrow indicates the Sun-Earth line. The coloured meridians visible on the surface of the Sun represent the solar central meridian as viewed from STEREO A (red), STEREO B (blue), and Earth (black). The presented times are: the start of the HF-type II (*panel a*), middle of HF-type II (*panel b*), start of LF-type II (*panel c*), and the end of LF-type II (*panel d*). The different parameters plotted in the rows are, (1) the Alfvén Mach number (M_A), (2) the density compression ratio, and (3) the angle between the shock normal and the upstream magnetic field (θ_{BN}). (Adapted from Jebaraj et al. 2021.)

The modelled pressure wave at this time was at a height of about $2.1 R_o$ as it steepened to a shock only in some regions as seen in Figs. 29a1 and a2. In other regions (coloured black and dark blue) the compression ratio was less than one, indicating that a wave has not steepened into a shock. The shock wave was strong along narrow regions on the flanks where both the density compression and shock geometry had considerably high values of ~ 3.5 and $\sim 60^\circ$ respectively.

Shock regions located near the apex of the CME are characterised by the high Alfvén mach number ($M_A \gg 6$) and density compression (~ 3.5). However, in this region the shock geometry was predominantly quasi-parallel ($\theta_{BN} \ll 30^\circ$), suggesting that in this regions the shock drift acceleration will not be very efficient.

Row b of Fig. 29 shows the wave at 00:00 UT which corresponds to the time of the middle of the HF-type II radio burst. The shock was formed near the apex of the CME, along its main direction of propagation. Additionally, at a few locations along the flanks we found a median value of ~ 2.5 for the Alfvén Mach number M_A indicating that the pressure wave also steepened into a shock. We note that these regions are located close to a coronal streamer where the Alfvén speed is low due to the weak magnetic field and the plasma density higher than the ambient density. The shock wave strength is enhanced when propagating through such a regions and, consequently, the shock is thus more efficient in electron acceleration. The density compression ratio shows similar behaviour to the Alfvén Mach number (e.g. Fig. 29b1). The highest values are found in the more extended region stretching from flank regions (near the streamer) and across the apex region. Panel b3 of Fig. 29 shows that the shock geometry was mostly quasi-parallel at the apex and was quasi-perpendicular towards the flanks. At 00:30 UT, approximately after the onset of the LF-type II radio burst, the apex of the modelled wave was at a distance of $7.5 R_o$. The shock wave continued to strengthen at the apex region and a region along the eastern flanks. The propagation direction of the LF-type II is marked by the red arrow (Fig. 29c1). This region was also located in close proximity to the heliospheric current sheet (HCS) which is marked in panel c3 of Fig. 29 with the black strips on the shock bubble.

The shock wave continued to evolve but less rapidly than in the previous snapshots (Fig. 29d). At approximately 00:50 UT the ending of the LF-type II burst was also observed. Furthermore, the shock compression in the lower regions of the flank are below unity suggesting that the shock wave may have already passed from a piston-driven phase into mostly a blast wave propagation and therefore subject to weakening.

C) Synthetic radio spectra

To explore the importance of different variables and their role in the generation of radio emission, we assumed the shock drift acceleration mechanism (SDA; see e.g. Street et al. 1994; Ball & Melrose 2001; Mann & Klassen 2005; Mann et al. 2018, and references therein). For SDA, a pre-existing supply of non-thermal electrons is required since the acceleration of lower energy thermal electrons is not very efficient in low β plasma (solar corona). Nevertheless, this can be offset if the tail of the upstream thermal electron distribution can be accelerated to high-enough energies by a nearly-perpendicular ($\theta_{BN} \sim 90^\circ$) shock wave geometry. For radio waves to be produced, high frequency electrostatic Langmuir waves need to be generated efficiently. Langmuir waves are generated by an

unstable distribution of streaming electrons where the faster non-thermal electrons outrun the slower thermal electrons (e.g. Melrose 1980; Robinson & Cairns 2000; Mann et al. 2018).

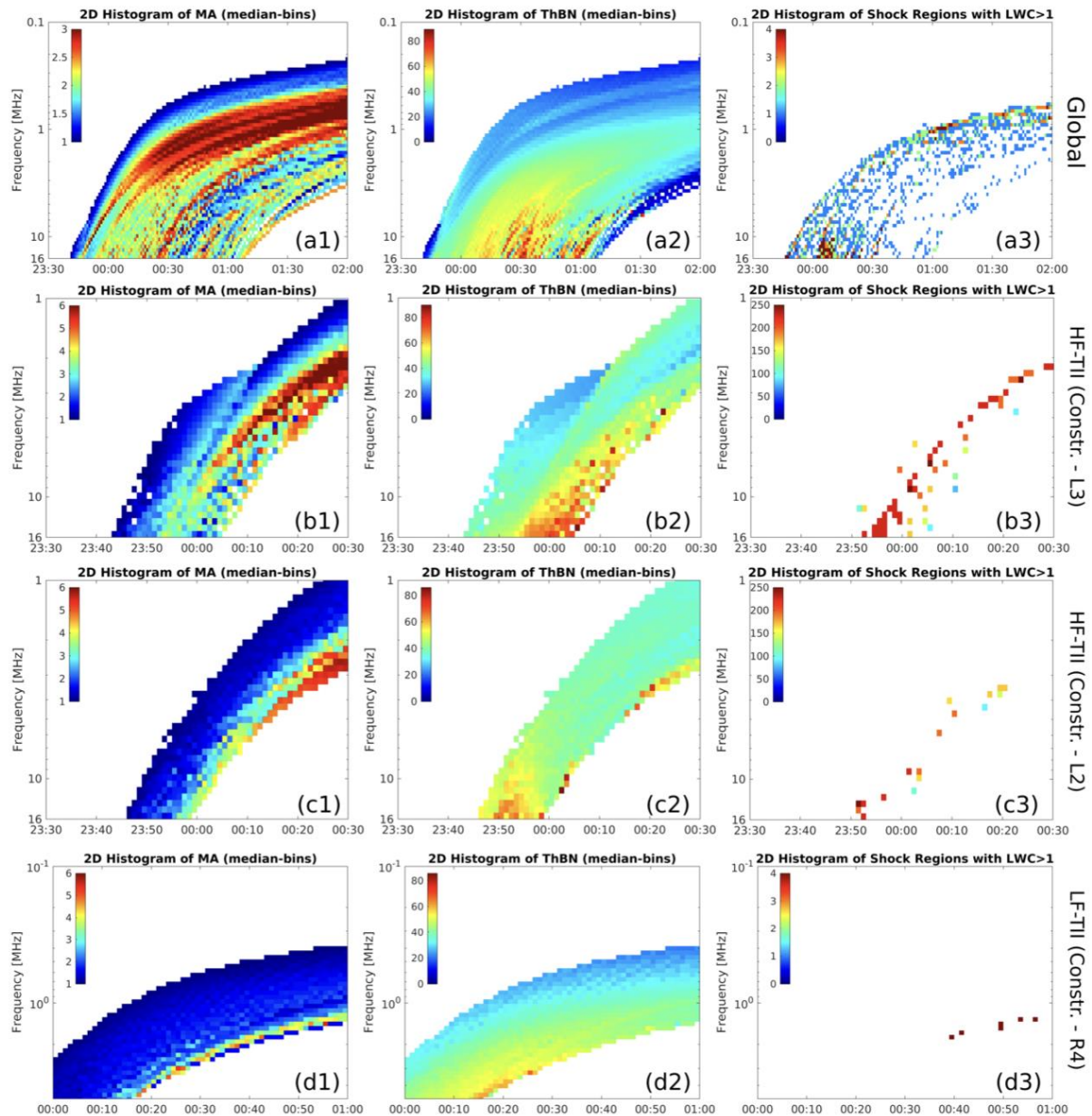


Figure 30

Histogram maps of different shock wave parameters plotted in a form of dynamic spectra. The four rows of 2D-histogram maps were produced in different areas of the wave. The histogram maps were constructed considering: (a) the full shock surface, (b) only L3 region of HF-type II, (c) region L2 of HF-type II, and (d) region R4 of LF-type. The three columns show different wave parameters: (1) the Alfvén Mach number (M_A), (2) the Shock wave geometry (ϑ_{BN}), and (3) the Langmuir wave conversion ratio ($LWC > 1$). (Adapted from Jebaraj et al. 2021.)

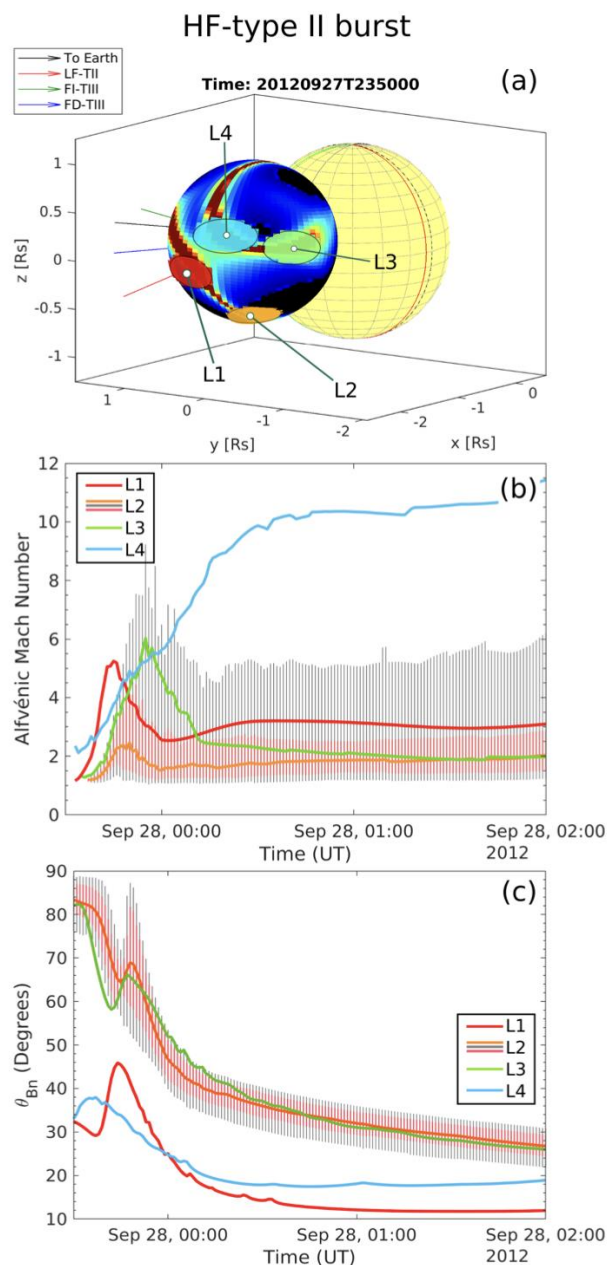
After being excited, the Langmuir waves may undergo wave-particle and wave-wave nonlinear interactions to produce radio emission in the fundamental and harmonic of the local plasma frequencies. The intensity of the emission at both bands is highly dependent on few factors such as the upstream electron and ion temperatures.

Once the radio waves are emitted, the ambient density inhomogeneities may also suppress the waves produced close to the local plasma frequency. Therefore, the chain of events leading up to the production of radio emission are dependent on macroscopic details, such as shock wave and upstream properties, as well as kinetic factors, such as the distribution of the electrons and their properties (Knock et al. 2003a).

To quantify the relationship between the wave parameters (e.g. M_A and θ_{BN}) in specific regions of the wave with the possibly associated radio emission, we used a novel approach introduced in Kouloumvakos et al. (2021). We produced 2D histogram maps, which is a spectrum like presentation of the wave parameters as a function of time (hereafter: synthetic spectra). The synthetic spectra was produced at close to the plasma frequency which allows comparison with the fundamental components of the radio emission observed in the dynamic spectra. Since the radio emission process depends on the Langmuir waves, we also used the model described in Mann & Klassen (2005) and Mann et al. (2018) to estimate the efficiency of the Langmuir waves production of this process can be examined using the cross-shock potential obtained from the Rankine-Hugoniot jump conditions. Mann et al. (2018) adopted the model described in Holman & Pesses (1983) for analysing the cross-shock potential of nearly perpendicular shock wave geometries as this determines the distribution of the unstable electron beams. Therefore, the efficiency at which Langmuir waves are produced and subsequently converted into electromagnetic radiation can be used to map the regions that are most favourable for the generation of type II radio emission.

Columns 1 and 2 in Fig. 30 show a complex spectral evolution of the pressure wave's strength and geometry (M_A and θ_{BN}). The synthetic spectra presented in panels a1 and a2 show that there are several regions where the pressure wave is super-critical and quasi-perpendicular, namely, where shock wave characteristics are present. In these regions, Langmuir waves can be efficiently produced and subsequently converted into electromagnetic radiation (see panel a3). This indicates that the shock associated radio emission can be, in principle, generated co-temporally at more than one location but with strongly different efficiency. The panel a3 of Fig. 30 shows one dominant high intensity region, starting around 16 MHz (at 00:00 UT) and after a gap (region of low efficiency for production of Langmuir oscillations) continuing about 30 min later at about 2 MHz. The patchy signatures are again enhanced at 01:00 UT and continue till the end of the modelling time. For the high frequency region we find a moderate shock strength and highly quasi-perpendicular geometry, and for the low-frequency region, we find a high shock strength and an oblique geometry.

The panels in row b and c of Fig. 30 present the spectra of the wave parameters in the specific regions L2 and L3 (see Sect. 5.2.2). Those two regions are possible source regions of the HF-type II radio emission. The two regions have similar θ_{BN} values, while the M_A is more enhanced for region L3 (see also Fig. 7). Further, also the bandwidth of the M_A and ϑ_{BN} in the region L3 is broader in comparison to L2. Comparing the Langmuir wave conversion (Figs. 9c2 and c3) for both regions, it is clear that the L3 region is more likely to be the source of radio emission than the region L2. This result indicates that even small difference in the shock wave strength, M_A , can be essential for the generation of the radio emission. We note that although the major contribution to the HF-type II radio emission is probably from region L3, a small contribution from the L2 region cannot be completely excluded (Fig. 30c3).

**Figure 31**

The HF-type II source regions on the pressure wave bubble. *Panel a*: modelled wave with the values of M_A plotted on the wave's surface roughly around the start of HF-type II radio burst. Circles titled L1–L4 represent the regions where the source of HF-type II could be located. *Panel b*: temporal evolution of the Alfvén mach number (M_A) in the selected regions which are represented by the colored median lines. The quartiles and decile values are given only for L2. The temporal evolution of the geometry in these regions is presented in *panel c*. (Adapted from Jebaraj et al. 2021.)

Figure 30 also shows the synthetic spectra of two main wave parameters and Langmuir wave conversion rate for the region R4. The location of region R4 was obtained in the radio triangulation study of LF-type II radio burst (Jebaraj et al. 2020). The synthetic spectrum for M_A shows only a narrow region with the high shock strength in the range between 2 MHz and 1MHz.

The synthetic spectrum of ϑ_{BN} shows that the wave geometry was most of the time oblique. The quasi-perpendicular regime was found only in the frequency range 3–1 MHz and in the very limited time interval (00:20–00:50 UT). The synthetic spectrum of Langmuir wave conversion rate (Fig. 30d3) shows that the Langmuir waves can be efficiently produced in a very narrow, patchy and intermittent region starting at \sim 00:40 UT at 2 MHz. This result does not fully coincide with the observations (Fig. 25), as the observed radio emission starts at about 00:20 UT at 1 MHz for the fundamental component that is modelled here.

We have previously shown that the emission could be originating also from the upper quartile and decile regions of the localized area. Therefore, median histograms may not be completely representative of the real situation, inducing discrepancy between observation and modelled shock wave characteristics. Furthermore, our model considers a spherical surface for the wave, which is a somewhat idealised picture.

4.3.3.4 Some conclusions on modeling of the shock wave and associated type II radiation

In this study (Jebaraj et al. 2021), the position of the type II radio bursts (see Jebaraj et al. 2020) was compared with the modelled pressure wave obtained from combined multi-viewpoint observations in EUV and WL, and the MAST model.

The first part of the study was focussed to the south-west region of the pressure wave bubble, most probably associated with the decametric HF-type II radio burst (see Fig. 31). We found two regions, i.e., L2 and L3 where the wave geometry exceeded $\theta_{BN} \sim 70^\circ$ and the strength was as high as $M_A \sim 5$. Therefore, out of these two regions, region L3 appears to be most probable type II source region.

In the second part of the study, we found that the shock geometry at the time of the LF-type II radio burst was mostly oblique, between 55° at the start and 45° at the end of the observed LF-type II burst (see Fig. 32). The type II source regions, obtained from radio triangulation, were located close to the streamer and the HCS. It is quite probable that due to this position, the particular geometry provided was favourable to the enhancement of the shock strength ($M_A \sim 3.5$) and, consequently, the generation of the radio emission as well. The most important results of the study are summarised below. Each point is also discussed in the framework of earlier studies.

- The comparison of radio observations and modelled pressure wave associated with an eruptive event shows that the wave may steepen to a shock, however, if it remains sub-critical, it will not produce type II radio emission. We find that radio emission is generated only when the shock wave is super critical, which is in accordance to the shock drift acceleration model that we employed to make the histogram maps. In this study, both the HF- and LF- type II radio bursts were formed when the shock wave was super-critical ($M_A \geq 2.0$). Comparing the modelling and radio observations, we found that the regions where the Alfvén Mach number was greater than unity, but sub-critical ($M_A \leq 2.0$), did not provide any contribution to the observed type II radio emission. This finding is also in accordance to Gopalswamy et al. (2010), who found that sub-critical shock waves are often radio quiet.
- Our analysis shows that a specific combination of shock geometry, shock strength, shock speed, and the presence of energetic electrons is essential for generation of radio emission.

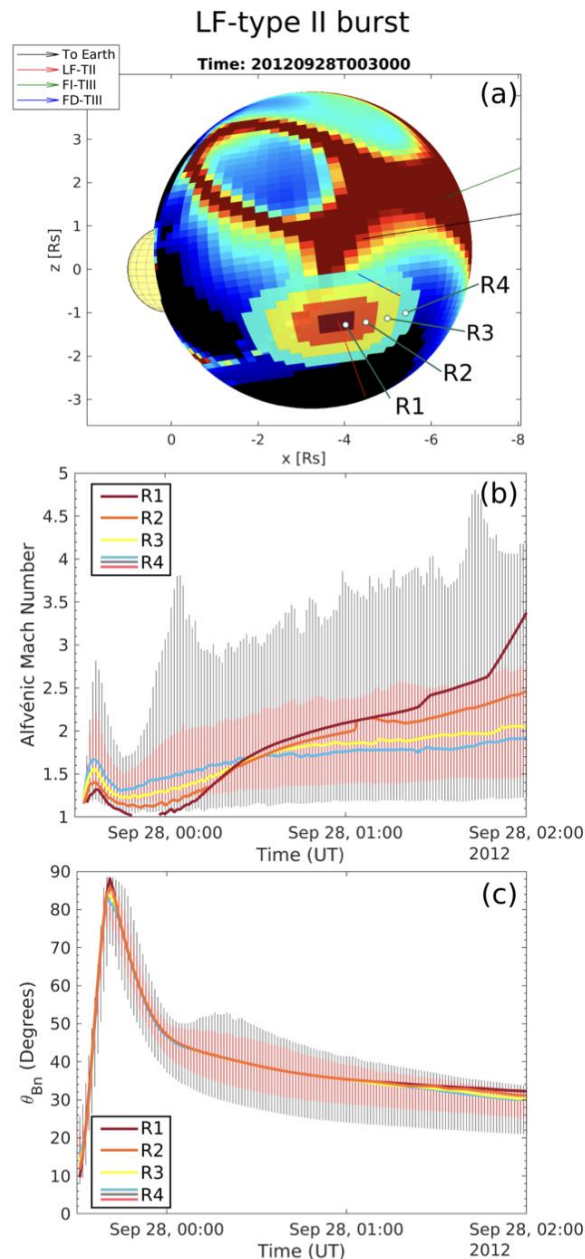
We found that a quasi perpendicular geometry was crucial for the generation of the herein studied type II bursts. We also found that the generation of the radio emission depends less on the shock wave strength in the case of high values for $f M_A \geq 3.0$. This is more pronounced at larger heights where the shock strength and compression ratio show little variation.

The studies of the importance of shock wave geometry in the generation of radio emission (e.g. Krauss-Varban & Wu, 1989) also showed that electrons are most efficiently energised in the quasi-perpendicular regime. We found that the decametric HF-type II was formed in regions where the shock geometry was $\vartheta_{BN} \geq 70^\circ$; this finding is similar to those from Kouloumvakos et al. (2021) for metric type II radio bursts. For the LF-type II, the results were somewhat different. The type II was formed when the shock geometry, obtained from modelling, was more oblique than in the case of the HF-type II. We found small regions with the quasi-perpendicular regime and it is probable that the patchy LF-type burst was generated in these small regions. According to Kuncic et al. (2002) for a quasi-perpendicular shock wave geometry, the spatially varying cross shock potential only shows small changes when $M_A \geq 3.0$. Given that the strength of the shock wave in the interplanetary space is, on average, $M_A \gg 2.0$, the LF-type II radio emission may largely depend on the shock wave geometry and the upstream electron distribution.

- We showed that intermittency of the radio emission, in particular of the HF-type II radio burst, was probably due to localised source regions with rapidly changing geometry. We also confirmed that the source of the HF-type II is located close to the western CME flank, as suggested by Jebaraj et al. (2020). This result also confirms that for the studied event, the intensity of the radio emission was highest towards the direction of the emission.

The particular morphology of the studied type II radio burst is a consequence of the changes in shock wave geometry, namely, an only intermittently present quasi-perpendicular regime, despite the rather strong shock wave: $M_A \geq 2.0$. Mann et al. (2018) showed that the intermittent generation of radio emission can be strongly pronounced during the early stage of the wave evolution when the geometry of the wave can change rapidly.

- The synthetic spectra show that the shock associated radio emission can have contributions from more than one source on the shock wave. However, in considering the morphology of the type II emission (only one dominant drift rate) we can speculate that only one of the sources is dominant and that the radio emission originating from the additional sources is very weak. In this study, we found that the region where the source of the HF-type II is located had other smaller regions, which switched on and off to Langmuir wave activity (and therefore radio emission). The emission from these regions may be recorded as extremely intermittent and could appear co-temporal and co-spatial with the primary source of the type II burst.
- The LF-type II sources were found to be situated in a region close to the HCS, but also close to the nearby streamer (as suggested by Jebaraj et al. 2020). This work shows that the shock wave characteristics, such as the strength and the geometry, nearby HCS and streamer regions are indeed favourable with regard to efficient electron acceleration.

**Figure 32**

Shock wave association with the LF-type II radio burst. *Panel a*: modelled pressure wave with the values of M_A plotted on its surface around the start time of LF-type II radio burst. The colour-coded source regions named R1–R4 represent the LF-type II source regions observed in the time interval between 00:25 and 00:50 UT. The varying diameters of the source regions account for the large source sizes obtained from the radio triangulation results. *Panel b*: temporal evolution of the Alfvén mach number (M_A) in the selected regions which are represented by the colored median lines. The quartiles and decile values are shown only for R4. The temporal evolution of the θ_{BN} in all regions is presented in *panel c*. (Adapted from Jebaraj et al. 2021.)

While modelling showed that the shock wave during the LF- type II was mostly quasi-parallel, we found a region where the shock wave was quasi-perpendicular, namely: the region of the shock crossing the HCS. Similarly, Reiner et al. (1998) found that IP type II radio bursts can be efficiently produced when shock waves cross the HCS or stream interaction regions (SIRs) where a large number of moderately energetic electrons is present.

Another possibility discussed by Pulupa & Bale (2008) assumes that the shock wave distortions in the form of ‘cavities’ can form naturally near the HCS. When $\beta > 1$ (e.g. Robinson & Cairns 2000), the shock front distortion can be naturally formed. The self-consistent modelling of the evolution of such shocks with distortions (e.g. ripples or wavy features) is challenging and was done in 3D only seldom. The extended discussion on the employed assumptions and model uncertainties can be found in Jebaraj et al. 2021.

4.3.4 Role of the coronal environment in the formation of four shocks observed without CMEs at Earth’s Lagrangian Point L1

This section presents work published in Pick et al. (2020).

The main goal of this study was to determine the solar origin of four single shocks observed at the Lagrange point L1 and followed by storm sudden commencements (SSCs) during 2002. We look for associated coronal mass ejections (CMEs), starting from estimates of the transit time from Sun to Earth. For each CME, we investigate its association with a radio type II burst, an indicator of the presence of a shock wave. For three of the events, the type II burst is shown to propagate along the same, or a similar, direction as the fastest segment of the CME leading edge. We analyze for each event the role of the coronal environment in the CME development, the shock formation, and their propagation, to finally identify its complex evolution. The ballistic velocity of these shocks during their propagation from the corona to L1 is compared to the shock velocity at L1. Based on a detailed analysis of the shock propagation and possible interactions up to 30 solar radii, we find a coherent velocity evolution for each event, in particular for one event, the 2002 April 14 SSC, for which a previous study did not find a satisfactory CME source. For the other three events, we observe the formation of a white-light shock overlying the different sources associated with those events. The localization of the event sources over the poles, together with an origin of the shocks being due to encounters of CMEs, can explain why at L1 we observe only single shocks and not interplanetary CMEs. For more details on this study see Pick et al. (2020).

4.4 On the further improvements of EUHFORIA

In the framework of the CCSOM project number of scientific papers was published with the topic related to the improvements of the EUHFORIA model. In this section some of these publications will be briefly addressed.

4.4.1 Implementing the MULTI-VP coronal model in EUHFORIA: Test case results and comparisons with the WSA coronal mode

This section presents mostly work published in Samara et al. (2021).

4.4.1.1 Summary

In this study, we focus on improving the EUHFORIA model. As described in the previous sections, EUHFORIA consists of two parts covering two spatial domains: the solar corona and the inner heliosphere. For the first part, the semi-empirical Wang-Sheeley-Arge (WSA) model is used by default; this model employs the potential field source surface and Schatten current sheet models to provide

the necessary solar wind plasma and magnetic conditions above the solar surface, at 0.1 AU, which serve as boundary conditions for the inner heliospheric part of EUHFORIA. The background solar wind modeling with EUHFORIA (Hinterreiter et al 2019) indicated the need of improvements of the coronal model of EUHFORIA. This study presents first results of the implementation of an alternative coronal model in EUHFORIA, the so-called MULTI-VP model (Pinto & Rouillard. 2017).

After we replaced the default EUHFORIA coronal setup with the MULTI-VP model, we compared their outputs both at 0.1 AU and 1 AU, for test cases involving high speed wind streams (HSSs). We select two distinct cases in which the standard EUHFORIA setup failed to reproduce the HSS plasma and magnetic signatures at Earth to test the performance of MULTI-VP coupled with EUHFORIA-heliosphere.

In order to understand the quality of modeling with MULTI-VP in comparison with the default coronal model in EUHFORIA, we considered one HSS case during a period of low solar activity and another one during a period of high solar activity. Moreover, the modeling of the two HSSs was performed by employing magnetograms from different providers: one from the Global Oscillation Network Group (GONG) and the second from the *Wilcox* Space Observatory (WSO). This way, we were able to distinguish differences arising not only because of the different models but also because of different magnetograms.

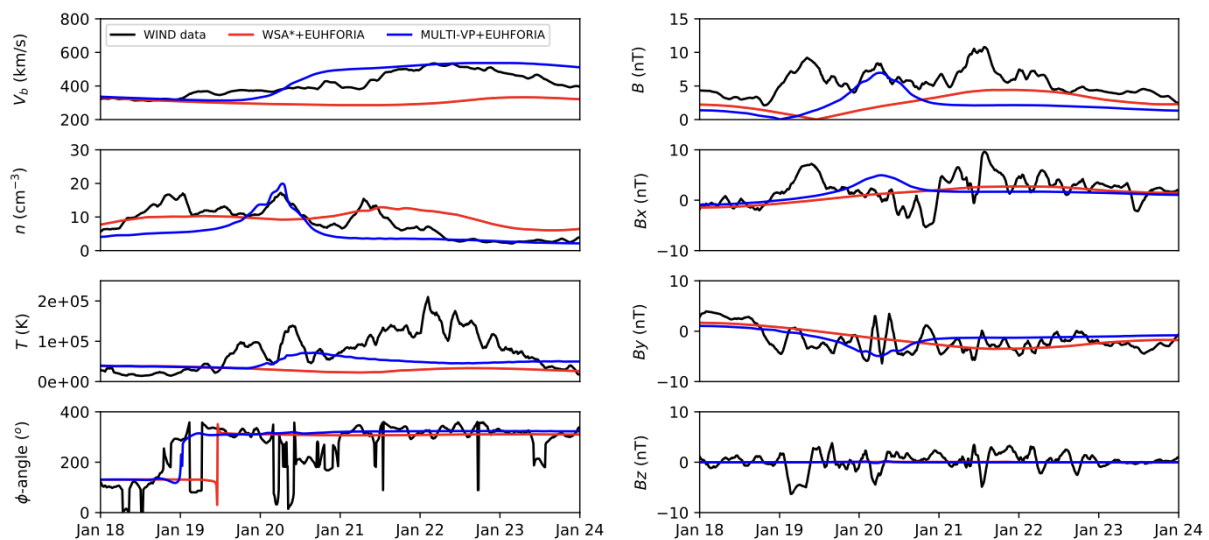


Figure 33

Plasma and magnetic parameters at 1 AU as modeled by WSA* +EUHFORIA-heliosphere (red) and MULTI-VP+EUHFORIA-heliosphere (blue) with a GONG magnetogram. The observed data as captured by WIND are depicted in black for the HSS that reached Earth on 2018-01-21.

The results of the study indicate that when employing a GONG magnetogram, the combination MULTI-VP+EUHFORIA-heliosphere reproduces the majority of HSS plasma and magnetic signatures measured at L1. On the contrary, the standard WSA+EUHFORIA-heliosphere combination does not capture the arrival of the HSS cases at L1. When employing WSO magnetograms, MULTI-VP+EUHFORIA-heliosphere reproduces the HSS that occurred during the period of high solar activity. However, it is unclear if it models the HSS during the period of low solar activity.

For the same magnetogram and periods of time, WSA+EUHFORIA-heliosphere is not able to capture the studied HSSs. The results show that the accuracy of the simulation output at Earth depends on the choice of both the coronal model and input magnetogram. Nevertheless, a more extensive statistical analysis is necessary to determine how precisely these choices affect the quality of the solar wind predictions.

The example of modeled HSS with two different set-up is presented in Fig. 33. The blue curve shows the significantly better modeling results for the MULTI-VP+EUHFORIA-heliosphere setup. Namely the results of the WSA+EUHFORIA-heliosphere setup, show that the HSS of interest was not captured at all. The same modeling results are presented in the 3D space on the Fig. 34.

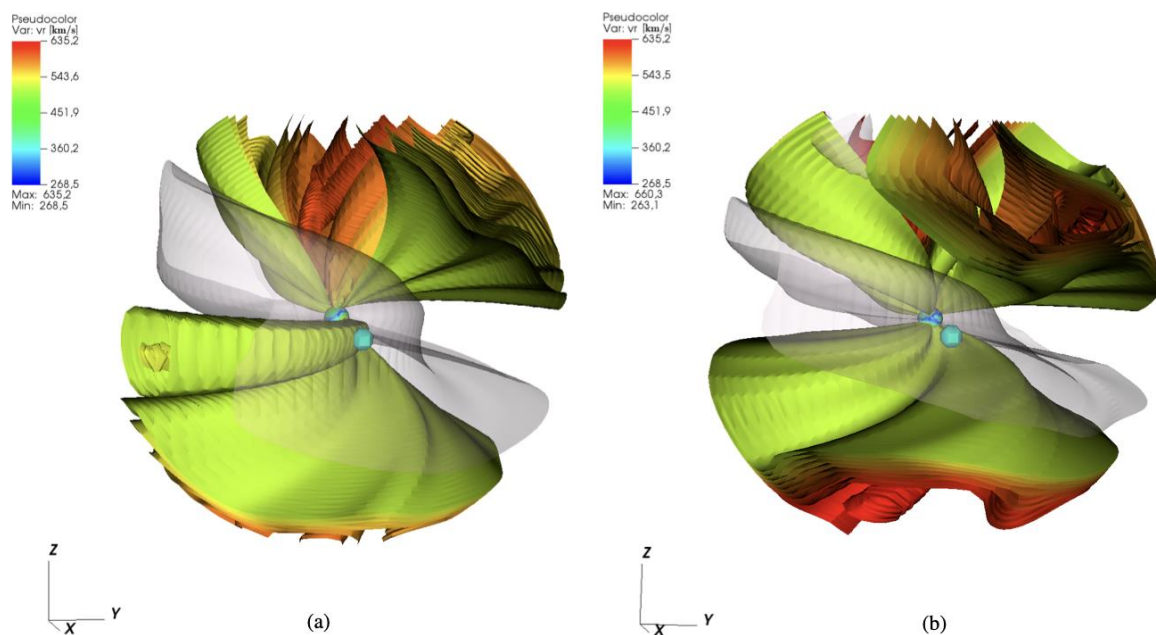


Figure 34

Contour plots of the radial solar wind velocities in 3D space as modeled with a GONG magnetogram (date: 2018-01-17T23:14, CR2199). The range of the velocities shown in the figure is between [520,600]kms⁻¹. The HCS ($B=0$) is depicted in gray, while the light blue sphere represents Earth. The sphere in the center of the figure represents the inner boundary (0.1 AU) and is color-coded based on the radial solar wind velocities at that radius, which are provided by the correspondent coronal model each time. (a) MULTI-VP+EUHFORIA. (b) WSA*+EUHFORIA.

4.4.1.2 Conclusions

In this study, we implemented for the first time an alternative coronal model in EUHFORIA, the MULTI-VP model (Pinto & Rouillard, 2017). We compared the output of the default coronal model with the output from MULTI-VP at the inner boundary of the heliospheric domain of EUHFORIA to understand the differences between the two models before they propagate to Earth. We also compared the performance of WSA*+EUHFORIA-heliosphere and MULTI-VP+EUHFORIA-heliosphere against in situ observations at Earth. In the frame of this study, we considered two different HSS cases: one during a period of low solar activity and another during a period of high solar activity. We also employed two different magnetograms, that is, GONG and WSO. Our results show that the choice of both the coronal model and magnetogram play an important role in the accuracy of the solar wind prediction. However, it is not clear which component plays the most important

role for the modeled results obtained at Earth. A statistical analysis with an appropriate number of simulations is needed to confirm our findings.

In the process of implementing MULTI-VP model in EUHFORIA, we encountered a number of elemental flows that are subcritical at 0.1 AU (typically less than 1% of the whole map and up to a few percent in the most extreme cases). The MULTI-VP model cannot assure a priori that the solar wind solutions it computes are super-fast at all angular positions at the target altitude of 0.1AU, as required for EUHFORIA. To correctly feed the MULTI-VP data into the heliospheric part of EUHFORIA, we needed to transform these speeds to super-critical such that all MHD characteristic curves are outgoing at 0.1 AU (Goedbloed et al. 2019). The correction was done by interpolating the subcritical, fast magnetosonic pixels with their closest super-critical neighbors obeying the mass-flux conservation. Once super-criticality was achieved at the boundary, we were able to study the v , n , T , B maps there. The analysis of inner boundary maps allowed us to obtain a first-order estimation regarding the differences between the models. Moreover, it helped us to understand how the two coronal models deal with different magnetograms.

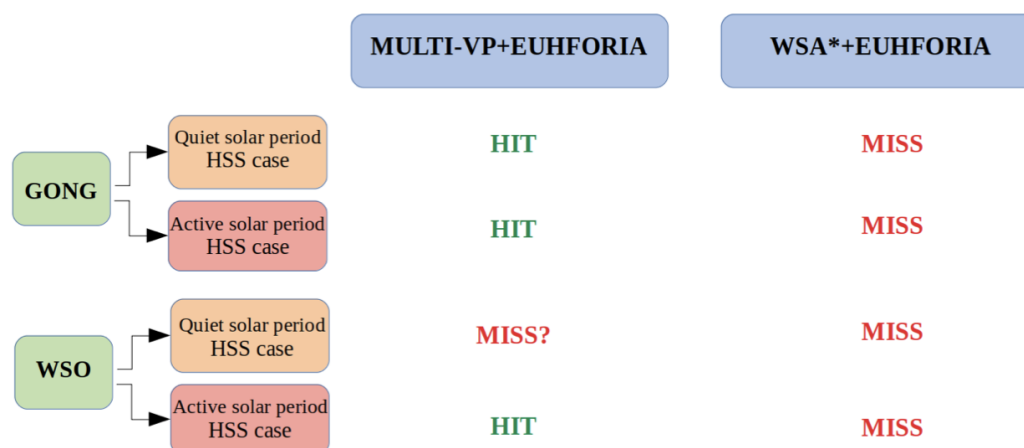


Figure 35

Schematic summary of the background solar wind modeling results at 1 AU regarding the solar wind bulk speed.

In Fig. 35, we outline our conclusions, in schematical presentation, based on the modeled bulk speed signatures at 1 AU. The results show that MULTI-VP+EUHFORIA-heliosphere is able to reproduce both HSSs cases when using GONG magnetograms and the HSS case during the active solar period, when employing a WSO magnetogram. However, it is not certain if it captures the HSS during the period of low solar activity when using the latter type of magnetogram. This is the reason we describe it as a “miss” with a question mark in Fig. 35. The WSA*+EUHFORIA-heliosphere combination, which we use as the reference model, does not reproduce any of the two test-case HSSs, regardless the magnetogram. However, these HSSs were specifically chosen on purpose, as cases that we knew a priori that were not reproduced well by the default EUHFORIA setup, to test the performance of MULTI-VP in combination with EUHFORIA-heliosphere. A bigger sample of HSSs needs to be simulated to determine if one of the models consistently outperforms the other.

The main reason that the two models provide different results at 1 AU, given the same input magnetogram, is the way they calculate the solar wind state at 0.1 AU. Even though both coronal models use the PFSS model to reconstruct the magnetic field in the low corona, they rely on different techniques to reconstruct the magnetic field higher in the corona, up to the radial distance of 0.1 AU. The default EUHFORIA setup is based on the SCS model to create a more uniform magnetic field, and on the WSA speed, which determines the solar wind plasma and magnetic parameters at 0.1 AU. The WSA wind speed essentially depends on magnetic information at two specific altitudes: the solar surface and 0.1 AU. On the other hand, MULTI-VP calculates the heating and acceleration of all wind streams at every height (see Eqs. (6)–(8) in Samara et al., 2021) and provides a uniform

magnetic field away from the Sun by applying an additional flux-tube expansion profile to them. Therefore, the differences in the numerical approach and underlying assumptions of the two models lead to distinctly different outputs. It is also important to mention that even though WSA* does not reproduce the two particular HSSs in this study, it is considered a reliable coronal model that is computationally inexpensive in comparison to MULTI-VP.

4.4.2 ICARUS, a new inner heliospheric model with a flexible grid

To improve the shock capturing and speed up the simulations we developed ICARUS a new heliospheric wind model for EUHFORIA. The ICARUS (Verbeke et al. 2022) combines radial grid stretching with solution Adaptive Mesh Refinement (AMR). We note that combining AMR strategies yields a speed-up in wall-clock time of up to 28.

This section presents mostly work published in Verbeke et al. (2022).

4.4.2.1 Summary

Simulating the propagation and predicting the arrival time of CMEs in the inner heliosphere with a full three-dimensional (3D) magnetohydrodynamic (MHD) propagation model requires a significant amount of computational time. For CME forecasting purposes, multiple runs may be required for different reasons such as ensemble modeling (uncertainty on input parameters) and error propagation. Moreover, higher resolution runs may be necessary, which also requires more CPU time, for example for the prediction of solar energetic particle acceleration and transport or in the framework of more in-depth studies about CME erosion and/or deformation during its evolution. In this section we present ICARUS, a new inner heliospheric model for the simulation of a steady background solar wind and the propagation and evolution of superposed CMEs. This novel model has been implemented within the MPI-AMRVAC framework which enables the use of stretched grids and solution adaptive mesh refinement (AMR). The usefulness and efficiency, i.e., speed-up, of these advanced features are explored. In particular, we model a background solar wind with ICARUS and then launch a simple cone CME and follow its evolution. The obtained modeling results are compared with the modeling output of EUHFORIA (Fig. 36).

For the solar background wind simulation run, we limited the mesh refinement to the area(s) of interest, in this case a corotating interaction region (CIR). For the CME evolution run, on the other hand, we apply AMR where the CME is located by the use of a tracing function. As such, the grid is coarsened again after the CME has passed.

The implemented AMR is flexible and only refines the mesh in a particular sector of the computational domain, for example around the Earth or a single CIR, and/or for a particular feature such as CIR or CME shocks. Radial grid stretching alone yields speed-ups of up to 4 and more, depending on the resolution. Combined with solution adaptive mesh refinement, the speed-ups can be much larger depending on the complexity of the simulation (e.g., number of CIRs in the background wind, number of CMEs) and on the chosen AMR criteria, thresholds and the number of refinement levels. The ICARUS model implemented in the MPI-AMRVAC framework is a new inner heliospheric 3D MHD model that uses grid stretching as well as AMR techniques. The flexibility in the grid and its resolution allows an optimization of the computational time required for CME propagation simulations for both scientific and forecasting purposes.

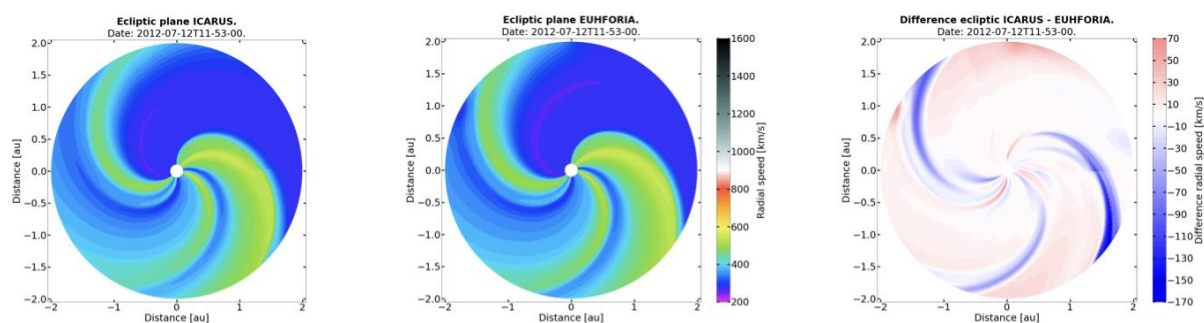


Figure 36

Comparison of the radial speed in the ecliptic plane between the ICARUS (*left panel*) and EUHFORIA (*middle panel*) models, where the *right panel* represents the difference between the two models.

4.4.2.2 Discussion and outlook

We presented a novel inner heliospheric wind and CME evolution model called ICARUS, which has been implemented within the MPI-AMRVAC framework. The usefulness and efficiency of radial grid stretching and solution adaptive mesh refinement have been explored by modeling a typical solar wind with ICARUS and then launching a simple (cone) CME and following its evolution.

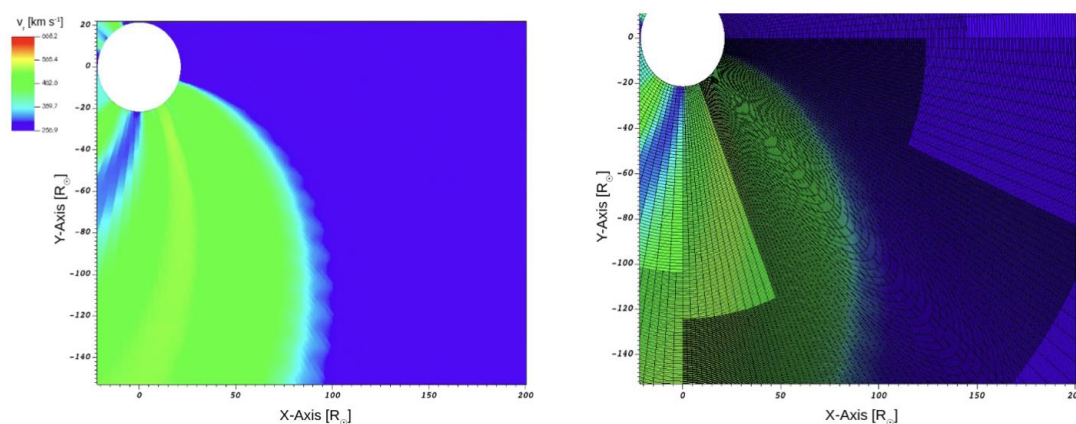


Figure 37

Simulation run with solution AMR limited to three grid levels applied to a single CIR region. The x- and y-axes are shown in R_{\odot} . Both figures are zoomed-in versions of the ecliptic plane, showing the radial speed values. The *right panel* displays the mesh grid resolution at the different AMR levels in addition to the radial speed.

We focused on the potential of radial grid stretching and two specific methods or criteria to trigger solution adaptive grid refinement. For the steady background wind simulation, we limited the mesh refinement to one of the CIRs and for the CME evolution run, we applied the refinement according to the tracing function of the CME, in order to follow it from the inner boundary toward the outer boundary as it propagates in the inner heliosphere. When the CME has passed, the grid is coarsened in order to avoid unnecessary refinement in the domain.

Radial grid stretching introduced a significant speed-up of the simulation because the load in the domain is decreased and less information is processed at each step. In addition, due to the radial grid stretching, the grid cells far away from the Sun do not have an elongated shape any more (see Figs. 37 and 38). Moreover, the radial grid stretching yielded a speed-up of about 3.5 for the high resolution grid.

Solution AMR also had a substantial effect on the wall-clock time of the simulation. The block-adaptive AMR in AMRVAC is very flexible and allows for different AMR strategies and thresholds depending on the needs. Several possible refinement conditions or criteria can be considered. In this work we applied a grid refinement based on the CME tracing function, which refines the domain where the (entire) CME is present. This enables high spatial resolution at the varying CME location, and grid coarsening after the CME has past. In the following work we will apply a CME shock mesh refinement condition. This will not only increase the resolution in the shock, but also, depending on the background wind conditions, any other shock waves in the solar wind, like the CIR shocks that form at the interaction regions of the high and slow speed streams.

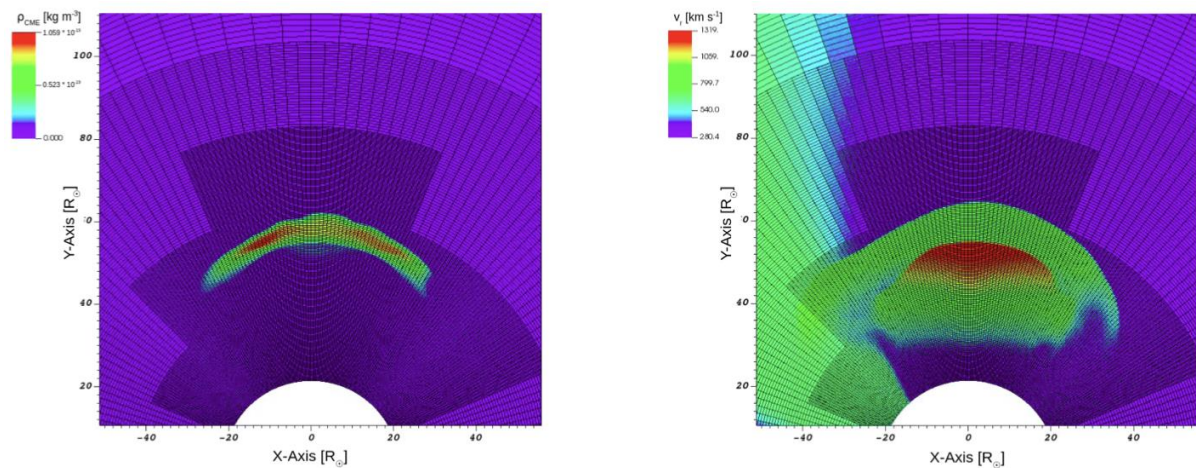


Figure 38

Example of AMR grid with three grid levels (base + two refinements) applied to a cone CME. The x- and y-axes show distance in R_{\odot} . *Left panel*: tracing function. *Right panel*: radial speed.

The simulation speed-up by introducing solution AMR was very notable, but depended on the required resolution i.e., on the number of refinement levels. Since the shock refinement criterion was fulfilled in larger portions of the computational domain, more grid cells were refined. Therefore, the simulations needed slightly more CPU and wall-clock time than those in which the refinement criterion was based on the tracing function. Depending on the requirements for the simulation, the AMR criterion (or criteria) can be adjusted.

In this study we considered the effect of radial grid stretching in the domain and the effect of imposing solution AMR on the original equidistant grid. While the stretched grid provided the highest speed-up, AMR level 3 provided results much closer to the middle and high resolution cases while still adding a considerable speed-up. As such, this setup may be preferred. However, in the followup work, we will consider the combination of radial grid stretching and AMR. Radial grid stretching, in the way we

implemented it here, decreases the number of cells in the domain and it decreases the spatial resolution at larger radial distances. However, this can be compensated for, wherever high spatial resolution is required, by combining the grid stretching with solution-adaptive grid refinement which enables very high effective spatial resolution without the high CPU costs this induces when the spatial resolution is increased everywhere in the computational domain. As a result of keeping the high spatial resolution local, only where needed, the simulation becomes much more efficient.

References in the text:

Abramenko, V., Yurchyshyn, V., & Watanabe, H. (2009). Parameters of the Magnetic Flux inside Coronal Holes. *Solar Physics*, 260 (1), 43–57. <https://doi.org/10.1007/s11207-009-9433-7>

Altschuler, M. D., & Newkirk, G. (1969). Magnetic Fields and the Structure of the Solar Corona. I: Methods of Calculating Coronal Fields. *Solar Physics*, 9 (1), 131–149. <https://doi.org/10.1007/BF00145734>

Arge, C. N., Luhmann, J. G., Odstrcil, D., Schrijver, C. J., & Li, Y. (2004). Stream structure and coronal sources of the solar wind during the May 12th, 1997 CME. *Journal of Atmospheric and Solar-Terrestrial Physics*, 66 (15-16), 1295–1309. <https://doi.org/10.1016/j.jastp.2004.03.018>

Arge, C. N., & Pizzo, V. J. (2000). Improvement in the prediction of solar wind conditions using near-real time solar magnetic field updates. *Journal of Geophysical Research (Space Physics)*, 105 (A5), 10465–10480. <https://doi.org/10.1029/1999JA000262>

Arge, C. N., Odstrcil, D., Pizzo, V. J., & Mayer, L. R. (2003). Improved Method for Specifying Solar Wind Speed Near the Sun. In M. Velli, R. Bruno, F. Malara, & B. Bucci (Eds.), *Solar wind ten* (pp. 190–193). <https://doi.org/10.1063/1.1618574>

Asvestari, E., Heinemann, S. G., Temmer, M., Pomoell, J., Kilpua, E., Magdalenic, J., & Poedts, S. (2019). Reconstructing Coronal Hole Areas With EUHFORIA and Adapted WSA Model: Optimizing the Model Parameters. *Journal of Geophysical Research (Space Physics)*, 124 (11), 8280–8297. <https://doi.org/10.1029/2019JA027173>

Asvestari, E., Pomoell, J., Kilpua, E., Good, S., Chatzistergos, T., Temmer, M., Palmerio, E., Poedts, S., & Magdalenic, J. (2021). Modelling a multi-spacecraft coronal mass ejection encounter with EUHFORIA. *Astronomy & Astrophysics*, 652, Article A27, A27. <https://doi.org/10.1051/0004-6361/202140315>

Ball, L., & Melrose, D. B. (2001). Shock Drift Acceleration of Electrons. *Publications of the Astronomical Society of Australia*, 18 (4), 361–373. <https://doi.org/10.1071/AS01047>

Bothmer, V., & Schwenn, R. (1998). The structure and origin of magnetic clouds in the solar wind. *Annales Geophysicae*, 16 (1), 1–24. <https://doi.org/10.1007/s00585-997-0001-x>

Bothmer, V. (2003). Sources of magnetic helicity over the solar cycle. In A. Wilson (Ed.), *Solar variability as an input to the earth's environment* (pp. 419–428).

Bougeret, J. L. (1985). Observations of shock formation and evolution in the solar atmosphere. *Geophysical Monograph Series (Washington, DC: American Geophysical Union)*, 35, 13. <https://doi.org/10.1029/GM035p0013>

Brchnelova, M., Zhang, F., Leitner, P., Perri, B., Lani, A., & Poedts, S. (2022). Effects of mesh topology on MHD solution features in coronal simulations. *Journal of Plasma Physics*, 88 (2), Article 905880205, 905880205. <https://doi.org/10.1017/S0022377822000241>

Burlaga, L. F., Plunkett, S. P., & St. Cyr, O. C. (2002). Successive CMEs and complex ejecta. *Journal of Geophysical Research (Space Physics)*, 107 (A10), Article 1266, 1266. <https://doi.org/10.1029/2001JA000255>

Burlaga, L. F. E. (1991). Magnetic Clouds. Physics of the inner heliosphere ii (pp. 1–22). https://doi.org/10.1007/978-3-642-75364-0_1

Burton, R. K., McPherron, R. L., & Russell, C. T. (1975). An empirical relationship between interplanetary conditions and Dst. *Journal of Geophysical Research (1896-1977)*, 80 (31), 4204. <https://doi.org/10.1029/JA080i031p04204>

Cairns, I. H., Knock, S. A., Robinson, P. A., & Kuncic, Z. (2003). Type II Solar Radio Bursts: Theory and Space Weather Implications. *Space Science Reviews*, 107 (1), 27-34. <https://doi.org/10.1023/A:1025503201687>

Cane, H. V., Richardson, I. G., & St. Cyr, O. C. (2000). Coronal mass ejections, interplanetary ejecta and geomagnetic storms. *Geophysical Research Letters*, 27 (21), 3591–3594. <https://doi.org/10.1029/2000GL000111>

Chané, E., Schmieder, B., Dasso, S., Verbeke, C., Grison, B., Démoulin, P., & Poedts, S. (2021). Over-expansion of a coronal mass ejection generates sub-Alfvénic plasma conditions in the solar wind at Earth. *Astronomy & Astrophysics*, 647, Article A149, A149. <https://doi.org/10.1051/0004-6361/202039867>

Chen, P. F., Harra, L. K., & Fang, C. (2014). Imaging and Spectroscopic Observations of a Filament Channel and the Implications for the Nature of Counter-streamings. *The Astrophysical Journal*, 784 (1), Article 50, 50. <https://doi.org/10.1088/0004-637X/784/1/50>

Cid, C., Saiz, E., & Cerrato, Y. (2008). Comment on “Interplanetary conditions leading to superintense geomagnetic storms (Dst ≤ -250 nT) during solar cycle 23” by E. Echer et al. *Geophysical Research Letters*, 35 (21), Article L21107, L21107. <https://doi.org/10.1029/2008GL034731>

Davies, J. A., Harrison, R. A., Perry, C. H., Möstl, C., Lugaz, N., Rollett, T., Davis, C. J., Crothers, S. R., Temmer, M., Eyles, C. J., & Savani, N. P. (2012). A Self-similar Expansion Model for Use in Solar Wind Transient Propagation Studies. *The Astrophysical Journal*, 750 (1), Article 23, 23. <https://doi.org/10.1088/0004-637X/750/1/23>

Devos, A., Verbeeck, C., & Robbrecht, E. (2014). Verification of space weather forecasting at the Regional Warning Center in Belgium. *Journal of Space Weather and Space Climate*, 4, Article A29, A29. <https://doi.org/10.1051/swsc/2014025>

Dumbović, M., Devos, A., Vršnak, B., Sudar, D., Rodriguez, L., Ruždjak, D., Leer, K., Vennerstrøm, S., & Veronig, A. (2015). Geoeffectiveness of Coronal Mass Ejections in the SOHO Era. *Solar Physics*, 290 (2), 579–612. <https://doi.org/10.1007/s11207-014-0613-8>

Garton, T. M., Gallagher, P. T., & Murray, S. A. (2018). Automated coronal hole identification via multi-thermal intensity segmentation. *Journal of Space Weather and Space Climate*, 8, Article A02, A02. <https://doi.org/10.1051/swsc/2017039>

Georgoulis, M. K. (2005). Turbulence In The Solar Atmosphere: Manifestations And Diagnostics Via Solar Image Processing. *Solar Physics*, 228 (1-2), 5–27. <https://doi.org/10.1007/s11207-005-2513-4>

Georgoulis, M. K. (2012). Are Solar Active Regions with Major Flares More Fractal, Multifractal, or Turbulent Than Others? *Solar Physics*, 276 (1-2), 161–181. <https://doi.org/10.1007/s11207-010-9705-2>

Gibson, S. E., & Low, B. C. (2000). Three-dimensional and twisted: An MHD interpretation of on-disk observational characteristics of coronal mass ejections. *Journal of Geophysical Research (Space Physics)*, 105 (A8), 18187–18202. <https://doi.org/10.1029/1999JA000317>

Goedbloed, J. P., Keppens, R., & Poedts, S. (2019). *Magnetohydrodynamics of Laboratory and Astrophysical Plasmas* (Cambridge: Cambridge University Press).

Gopalswamy, N., Lara, A., Lepping, R. P., Kaiser, M. L., Berdichevsky, D., & St. Cyr, O. C. (2000). Interplanetary acceleration of coronal mass ejections. *Geophysical Research Letters*, 27 (2), 145–148. <https://doi.org/10.1029/1999GL003639>

Gopalswamy, N., Xie, H., Mäkelä, P., Akiyama, S., Yashiro, S., Kaiser, M. L., Howard, R. A., & Bougeret, J. -L. (2010). Interplanetary Shocks Lacking Type II Radio Bursts. *The Astrophysical Journal*, 710 (2), 1111-1126 (2010). <https://doi.org/10.1088/0004-637X/710/2/1111>

Gopalswamy, N., Yashiro, S., Akiyama, S., & Xie, H. (2017). Estimation of Reconnection Flux Using Post-eruption Arcades and Its Relevance to Magnetic Clouds at 1 AU., *Solar Physics*, 292 (4), Article 65, 65. <https://doi.org/10.1007/s11207-017-1080-9>

Gressl, C., Veronig, A. M., Temmer, M., Odstrčil, D., Linker, J. A., Mikić, Z., & Riley, P. (2014). Comparative Study of MHD Modeling of the Background Solar Wind. *Solar Physics*, 289 (5), 1783–1801. <https://doi.org/10.1007/s11207-013-0421-6>

Heinemann, S. G., Temmer, M., Heinemann, N., Dissauer, K., Samara, E., Jerčić, V., Hofmeister, S. J., & Veronig, A. M. (2019). Statistical Analysis and Catalog of Non-polar Coronal Holes Covering the SDO-Era Using CATCH. *Solar Physics*, 294 (10), Article 144, 144. <https://doi.org/10.1007/s11207-019-1539-y>

Hinterreiter, J., Magdalenic, J., Temmer, M., Verbeke, C., Jebaraj, I. C., Samara, E., Asvestari, E., Poedts, S., Pomoell, J., Kilpua, E., Rodriguez, L., Scolini, C., & Isavnin, A. (2019). Assessing the Performance of EUHFORIA Modeling the Background Solar Wind. *Solar Physics*, 294 (12), Article 170, 170. <https://doi.org/10.1007/s11207-019-1558-8>

Hofmeister, S. J., Veronig, A. M., Poedts, S., Samara, E., & Magdalenic, J. (2020). On the Dependency between the Peak Velocity of High-speed Solar Wind Streams near Earth and the Area of Their Solar Source Coronal Holes. *The Astrophysical Journal Letters*, 897 (1), Article L17, L17. <https://doi.org/10.3847/2041-8213/ab9d19>

Holman, G. D., & Pesses, M. E. (1983). Solar Type II Radio Emission and the Shock Drift Acceleration of Electrons. *The Astrophysical Journal*, 267, 837-843. <https://doi.org/10.1086/160918>

Hosteaux, S., Chané, E., & Poedts, S. (2021). Analysis of Deformation and Erosion during CME Evolution. *Geosciences*, 11 (8), 314. <https://doi.org/10.3390/geosciences11080314>

Husidic, E., Lazar, M., Fichtner, H., Scherer, K., & Poedts, S. (2021). Transport coefficients enhanced by suprathermal particles in nonequilibrium heliospheric plasmas. *Astronomy & Astrophysics*, 654, Article A99, A99. <https://doi.org/10.1051/0004-6361/202141760>

Husidic, E., Scherer, K., Lazar, M., Fichtner, H., & Poedts, S. (2022). Toward a Realistic Evaluation of Transport Coefficients in Non-equilibrium Space Plasmas. *The Astrophysical Journal*, 927 (2), Article 159, 159. <https://doi.org/10.3847/1538-4357/ac4af4>

Huttunen, K. E. J., Koskinen, H. E. J., Pulkkinen, T. I., Pulkkinen, A., Palmroth, M., Reeves, E. G. D., & Singer, H. J. (2002). April 2000 magnetic storm: Solar wind driver and magnetospheric response. *Journal of Geophysical Research (Space Physics)*, 107 (A12), Article 1440, 1440. <https://doi.org/10.1029/2001JA009154>

Inhester, B. (2006). Stereoscopy basics for the STEREO mission. *arXiv e-prints*, Article astro-ph/0612649, astro-ph/0612649.

Isavnin, A. (2016). FRIED: A Novel Three-dimensional Model of Coronal Mass Ejections. *The Astrophysical Journal*, 833 (2), Article 267, 267. <https://doi.org/10.3847/1538-4357/833/2/267>

Jacobs, C., Roussev, I. I., Lugaz, N., & Poedts, S. (2009). The Internal Structure of Coronal Mass Ejections: Are all Regular Magnetic Clouds Flux Ropes? *The Astrophysical Journal*, 695 (2), L171–L175. <https://doi.org/10.1088/0004-637X/695/2/L171>

Jebaraj, I. C., Kouloumvakos, A., Magdalenic, J., Rouillard, A. P., Mann, G., Krupar, V., & Poedts, S. (2021). Generation of interplanetary type II radio emission. *Astronomy & Astrophysics*, 654, Article A64, A64. <https://doi.org/10.1051/0004-6361/202141695>

Jebaraj, I. C., Magdalenic, J., Podladchikova, T., Scolini, C., Pomoell, J., Veronig, A. M., Dissauer, K., Krupar, V., Kilpua, E. K. J., & Poedts, S. (2020). Using radio triangulation to understand the origin of two subsequent type II radio bursts. *Astronomy & Astrophysics*, 639, Article A56, A56. <https://doi.org/10.1051/0004-6361/201937273>

Kai, K. (1969). Radio Evidence of Directive Shock-Wave Propagation in the Solar Corona. *Solar Physics*, 10 (2), 460-464. <https://doi.org/10.1007/BF00145531>

Kilpua, E. K. J., Lumme, E., Andreeva, K., Isavnin, A., & Koskinen, H. E. J. (2015). Properties and drivers of fast interplanetary shocks near the orbit of the Earth (1995-2013). *Journal of Geophysical Research (Space Physics)*, 120 (6), 4112-4125. <https://doi.org/10.1002/2015JA021138>

Kilpua, E. K. J., Good, S. W., Palmerio, E., Asvestari, E., Lumme, E., Ala-Lahti, M., Kalliokoski, M. M. H., Morosan, D. E., Pomoell, J., Price, D. J., Magdalenic, J., Poedts, S., & Futaana, Y. (2019). Multipoint Observations of the June 2012 Interacting Interplanetary Flux Ropes. *Frontiers in Astronomy and Space Sciences*, 6, Article 50, 50. <https://doi.org/10.3389/fspas.2019.00050>

Klassen, A., Aurass, H., Klein, K., Hofmann, A., & Mann, G. (1999). Radio evidence on shock wave formation in the solar corona. *Astronomy and Astrophysics*, 343, 287-296.

Knock, S. A., Cairns, I. H., Robinson, P. A., & Kuncic, Z. (2003a). Theoretically Predicted Properties of Type II Radio Emission from an Interplanetary Foreshock. *Journal of Geophysical Research (Space Physics)*, 108 (A3), 1126. <https://doi.org/10.1029/2002JA009508>

Kouloumvakos, A., Rouillard, A. P., Wu, Y., Vainio, R., Vourlidas, A., Plotnikov, I., Afanasiev, A., & Önel, H. (2019). Connecting the Properties of Coronal Shock Waves with Those of Solar Energetic Particles. *The Astrophysical Journal*, 876 (1), Article 80, 80. <https://doi.org/10.3847/1538-4357/ab15d7>

Kouloumvakos, A., Rouillard, A., Warmuth, A., Magdalenic, J., Jebaraj, I. C., Mann, G., Vainio, R., & Monstein, C. (2021). Coronal Conditions for the Occurrence of Type II Radio Bursts. *The Astrophysical Journal*, 913 (2), Article 99, 99. <https://doi.org/10.3847/1538-4357/abf435>

Krauss-Varban, D., & Wu, C. S. (1989). Fast Fermi and Gradient Drift Acceleration of Electrons at Nearly Perpendicular Collisionless Shocks. *Journal of Geophysical Research*, 94 (A11), 15367-15372. <https://doi.org/10.1029/JA094iA11p15367>

Krupar, V., Eastwood, J. P., Kruparova, O., Santolik, O., Soucek, J., Magdalenic, J., Vourlidas, A., Maksimovic, M., Bonnin, X., Bothmer, V., Mrotzek, N., Pluta, A., Barnes, D., Davies, J. A., Martinez Oliveros, J. C., & Bale, S. D. (2016). An Analysis of Interplanetary Solar Radio Emissions Associated with a Coronal Mass Ejection. *The Astrophysical Journal Letters*, 823 (1), Article L5, L5. <https://doi.org/10.3847/2041-8205/823/1/L5>

Krupar, V., Santolik, O., Cecconi, B., Maksimovic, M., Bonnin, X., Panchenko, M., & Zaslavsky, A. (2012). Goniopolarimetric inversion using SVD: An application to type III radio bursts observed by STEREO. *Journal of Geophysical Research (Space Physics)*, 117 (A6), Article A06101, A06101. <https://doi.org/10.1029/2011JA017333>

Kuncic, Z., Cairns, I. H., Knock, S., & Robinson, P. A. (2002). A Quantitative Theory for Terrestrial Foreshock Radio Emissions. *Geophysical Research Letters*, 29 (8), 1161, 1161. <https://doi.org/10.1029/2001GL014524>

Kunkel, V., & Chen, J. (2010). Evolution of a Coronal Mass Ejection and its Magnetic Field in Interplanetary Space. *The Astrophysical Journal Letters*, 715 (2), L80–L83. <https://doi.org/10.1088/2041-8205/715/2/L80>

Kwon, R.-Y., Zhang, J., & Olmedo, O. (2014). New Insights into the Physical Nature of Coronal Mass Ejections and Associated Shock Waves within the Framework of the Three-dimensional Structure. *The Astrophysical Journal*, 794 (2), Article 148, 148.

<https://doi.org/10.1088/0004-637X/794/2/148>

Lemen, J. R., Title, A. M., Akin, D. J., Boerner, P. F., Chou, C., Drake, J. F., Duncan, D. W., Edwards, C. G., Friedlaender, F. M., Heyman, G. F., Hurlburt, N. E., Katz, N. L., Kushner, G. D., Levay, M., Lindgren, R. W., Mathur, D. P., McFeaters, E. L., Mitchell, S., Rehse, R. A., Waltham, N. (2012). The Atmospheric Imaging Assembly (AIA) on the Solar Dynamics Observatory (SDO). *Solar Physics*, 275 (1-2), 17–40.

<https://doi.org/10.1007/s11207-011-9776-8>

Linker, J. A., Caplan, R. M., Downs, C., Riley, P., Mikić, Z., Lionello, R., Henney, C. J., Arge, C. N., Liu, Y., Derosa, M. L., Yeates, A., & Owens, M. J. (2017). The Open Flux Problem. *The Astrophysical Journal*, 848 (1), Article 70, 70. <https://doi.org/10.3847/1538-4357/aa8a70>

Lionello, R., Linker, J. A., & Mikić, Z. (2009). Multispectral Emission of the Sun During the First Whole Sun Month: Magnetohydrodynamic Simulations. *The Astrophysical Journal*, 690 (1), 902–912. <https://doi.org/10.1088/0004-637X/690/1/902>

Lugaz, N., Hernandez-Charpak, J. N., Roussev, I. I., Davis, C. J., Vourlidas, A., & Davies, J. A. (2010). Determining the Azimuthal Properties of Coronal Mass Ejections from Multi-Spacecraft Remote- Sensing Observations with STEREO SECCHI. *The Astrophysical Journal*, 715 (1), 493–499. <https://doi.org/10.1088/0004-637X/715/1/493>

Magdaleníć, J., Marqué, C., Zhukov, A. N., Vršnak, B., & Veronig, A. (2012). Flare-generated Type II Burst without Associated Coronal Mass Ejection. *The Astrophysical Journal*, 746 (2), Article 152, 152. <https://doi.org/10.1088/0004-637X/746/2/152>

Magdaleníć, J., Marqué, C., Krupar, V., Mierla, M., Zhukov, A. N., Rodriguez, L., Maksimović, M., & Cecconi, B. (2014). Tracking the CME-driven Shock Wave on 2012 March 5 and Radio Triangulation of Associated Radio Emission. *The Astrophysical Journal*, 791 (2), Article 115, 115. <https://doi.org/10.1088/0004-637X/791/2/115>

Magdaleníć, J., Marqué, C., Zhukov, A. N., Vršnak, B., & Žic, T. (2010). Origin of Coronal Shock Waves Associated with Slow Coronal Mass Ejections. *The Astrophysical Journal*, 718 (1), 266–278. <https://doi.org/10.1088/0004-637X/718/1/266>

Magdaleníć, J., Vršnak, B., Pohjolainen, S., Temmer, M., Aurass, H., & Lehtinen, N. J. (2008). A Flare-Generated Shock during a Coronal Mass Ejection on 24 December 1996. *Solar Physics*, 253 (1-2), 305–317. <https://doi.org/10.1007/s11207-008-9220-x>

Magdaleníć, J., Marqué, C., Fallows, R. A., Mann, G., Vocks, C., Zucca, P., Dabrowski, B. P., Krankowski, A., & Melnik, V. (2020). Fine Structure of a Solar Type II Radio Burst Observed by LOFAR. *The Astrophysical Journal Letters*, 897 (1), Article L15, L15. <https://doi.org/10.3847/2041-8213/ab9abc>

Mandelbrot, B. B. (1983). *The fractal geometry of nature /Revised and enlarged edition/*.

Mann, G., & Klassen, A. (2005). Electron Beams Generated by Shock Waves in the Solar Corona. *Astronomy and Astrophysics*, 441 (1), 319-326. <https://doi.org/10.1051/0004-6361:20034396>

Mann, G., Melnik, V. N., Rucker, H. O., Konovalenko, A. A., & Brazhenko, A. I. (2018). Radio signatures of shock-accelerated electron beams in the solar corona. *Astronomy & Astrophysics*, 609, Article A41, A41. <https://doi.org/10.1051/0004-6361/201730546>

Mann, G., Vocks, C., Warmuth, A., Magdaleníć, J., Bisi, M., Carley, E., Dabrowski, B., Gallagher, P., Krankowski, A., Matyjasiak, B., Rotkaehl, H., & Zucca, P. (2022). Excitation of Langmuir waves at shocks and solar type II radio bursts. *Astronomy & Astrophysics*, 660, Article A71, A71. <https://doi.org/10.1051/0004-6361/202142201>

Manning, R., & Fainberg, J. (1980). A new method of measuring radio source parameters of a partially polarized distributed source from spacecraft observations. *Space Science Instrumentation*, 5, 161–181.

Manoharan, P. K., Gopalswamy, N., Yashiro, S., Lara, A., Michalek, G., & Howard, R. A. (2004). Influence of coronal mass ejection interaction on propagation of interplanetary shocks. *Journal of Geophysical Research (Space Physics)*, 109 (A6), Article A06109, A06109. <https://doi.org/10.1029/2003JA010300>

McComas, D. J., Bame, S. J., Barker, P., Feldman, W. C., Phillips, J. L., Riley, P., & Griffée, J. W. (1998). Solar Wind Electron Proton Alpha Monitor (SWEPAM) for the Advanced Composition Explorer. *Space Science Reviews*, 86, 563–612.

<https://doi.org/10.1023/A:1005040232597>

McGregor, S. L., Hughes, W. J., Arge, C. N., Owens, M. J., & Odstrcil, D. (2011). The distribution of solar wind speeds during solar minimum: Calibration for numerical solar wind modeling constraints on the source of the slow solar wind. *Journal of Geophysical Research (Space Physics)*, 116 (A3), Article A03101, A03101. <https://doi.org/10.1029/2010JA015881>

Melrose, D. B. (1980). The Emission Mechanisms for Solar Radio Bursts. *Space Science Reviews*, 26 (1), 3-38. <https://doi.org/10.1007/BF00212597>

Mierla, M., Inhester, B., Marqué, C., Rodriguez, L., Gissot, S., Zhukov, A. N., Berghmans, D., & Davila, J. (2009). On 3D Reconstruction of Coronal Mass Ejections: I. Method Description and Application to SECCHI-COR Data. *Solar Physics*, 259 (1-2), 123–141. <https://doi.org/10.1007/s11207-009-9416-8>

Millas, D., Innocenti, M. E., Laperre, B., Raeder, J., Poedts, S., & Lapenta, G. (2020). Domain of Influence analysis: implications for Data Assimilation in space weather forecasting. *Frontiers in Astronomy and Space Sciences*, 7, Article 73, 73. <https://doi.org/10.3389/fspas.2020.571286>

Millward, G., Biesecker, D., Pizzo, V., & de Koning, C. A. (2013). An operational software tool for the analysis of coronagraph images: Determining CME parameters for input into the WSA-Enlil heliospheric model. *Space Weather*, 11 (2), 57–68. <https://doi.org/10.1002/swe.20024>

Morosan, D. E., Palmerio, E., Räsänen, J. E., Kilpua, E. K. J., Magdalenic, J., Lynch, B. J., Kumari, A., Pomoell, J., & Palmroth, M. (2020). Electron acceleration and radio emission following the early interaction of two coronal mass ejections. *Astronomy & Astrophysics*, 642, Article A151, A151. <https://doi.org/10.1051/0004-6361/202038801>

Möstl, C., Farrugia, C. J., Temmer, M., Miklenic, C., Veronig, A. M., Galvin, A. B., Leitner, M., & Biernat, H. K. (2009). Linking Remote Imagery of a Coronal Mass Ejection to Its In Situ Signatures at 1 AU. *The Astrophysical Journal*, 705 (2), L180–L185. <https://doi.org/10.1088/0004-637X/705/2/L180>

Nelson, G. J., & Melrose, D. B. (1985). Type II bursts. In D. J. McLean & N. R. Labrum (Eds.), *Solar radiophysics: Studies of emission from the sun at metre wavelengths* (pp. 333–359).

Niedziela, R., Murawski, K., & Poedts, S. (2021). Chromospheric heating and generation of plasma outflows by impulsively generated two-fluid magnetoacoustic waves. *Astronomy & Astrophysics*, 652, Article A124, A124. <https://doi.org/10.1051/0004-6361/202141027>

Nieves-Chinchilla, T., Jian, L. K., Balmaceda, L., Vourlidas, A., dos Santos, L. F. G., & Szabo, A. (2019). Unraveling the Internal Magnetic Field Structure of the Earth-directed Interplanetary Coronal Mass Ejections During 1995 - 2015. *Solar Physics*, 294 (7), Article 89, 89. <https://doi.org/10.1007/s11207-019-1477-8>

Odstrcil, D., Pizzo, V. J., & Arge, C. N. (2005). Propagation of the 12 May 1997 interplanetary coronal mass ejection in evolving solar wind structures. *Journal of Geophysical Research (Space Physics)*, 110 (A2), Article A02106, A02106. <https://doi.org/10.1029/2004JA010745>

Ogilvie, K. W., Chornay, D. J., Fritzenreiter, R. J., Hunsaker, F., Keller, J., Lobell, J., Miller, G., Scudder, J. D., Sittler, J., E. C., Torbert, R. B., Bodet, D., Needell, G., Lazarus, A. J., Steinberg, J. T., Tappan, J. H., Mavretic, A., & Gergin, E. (1995). SWE, A Comprehensive Plasma Instrument for the WIND Spacecraft. *Space Science Reviews*, 71 (1-4), 55–77. <https://doi.org/10.1007/BF00751326>

Palmerio, E., Kilpua, E. K. J., James, A. W., Green, L. M., Pomoell, J., Isavnin, A., & Valori, G. (2017). Determining the Intrinsic CME Flux Rope Type Using Remote-sensing Solar Disk Observations. *Solar Physics*, 292 (2), Article 39, 39. <https://doi.org/10.1007/s11207-017-1063-x>

Palmerio, E., Scolini, C., Barnes, D., Magdalenic, J., West, M. J., Zhukov, A. N., Rodriguez, L., Mierla, M., Good, S. W., Morosan, D. E., Kilpua, E. K. J., Pomoell, J., & Poedts, S. (2019). Multipoint Study of Successive Coronal Mass Ejections Driving Moderate Disturbances at 1 au. *The Astrophysical Journal*, 878 (1), Article 37, 37.

<https://doi.org/10.3847/1538-4357/ab1850>

Pelexhata, M., Murawski, K., & Poedts, S. (2021). Solar chromosphere heating and generation of plasma outflows by impulsively generated two-fluid Alfvén waves. *Astronomy & Astrophysics*, 652, Article A114, A114. <https://doi.org/10.1051/0004-6361/202141262>

Pesnell, W. D., Thompson, B. J., & Chamberlin, P. C. (2012). The Solar Dynamics Observatory (SDO). *Solar Physics*, 275 (1-2), 3–15. <https://doi.org/10.1007/s11207-011-9841-3>

Pick, M., Magdalenic, J., Cornilleau-Wehrin, N., Grison, B., Schmieder, B., & Bocchialini, K. (2020). Role of the Coronal Environment in the Formation of Four Shocks Observed without Coronal Mass Ejections at Earth's Lagrangian Point L1. *The Astrophysical Journal*, 895 (2), Article 144, 144. <https://doi.org/10.3847/1538-4357/ab8fae>

Pinto, R. F., & Rouillard, A. P. (2017). A Multiple Flux-tube Solar Wind Model. *The Astrophysical Journal*, 838 (2), Article 89, 89. <https://doi.org/10.3847/1538-4357/aa6398>

Poedts, S., Kochanov, A., Lani, A., Scolini, C., Verbeke, C., Hosteaux, S., Chané, E., Deconinck, H., Mihalache, N., Diet, F., Heynderickx, D., De Keyser, J., De Donder, E., Crosby, N. B., Echim, M., Rodriguez, L., Vansintjan, R., Verstringe, F., Mampaey, B., . . . Luntama, J.-P. (2020a). The Virtual Space Weather Modelling Centre. *Journal of Space Weather and Space Climate*, 10, Article 14, 14. <https://doi.org/10.1051/swsc/2020012>

Poedts, S., Lani, A., Scolini, C., Verbeke, C., Wijzen, N., Lapenta, G., Laperre, B., Millas, D., Innocenti, M. E., Chané, E., Baratashvili, T., Samara, E., Van der Linden, R., Rodriguez, L., Vanlommel, P., Vainio, R., Afanasiev, A., Kilpua, E., Pomoell, J., . . . Depauw, J. (2020b). EUropean Heliospheric FORecasting Information Asset 2.0. *Journal of Space Weather and Space Climate*, 10, Article 57, 57. <https://doi.org/10.1051/swsc/2020055>

Pomoell, J., & Poedts, S. (2018). EUHFORIA: European heliospheric forecasting information asset. *Journal of Space Weather and Space Climate*, 8, Article A35, A35. <https://doi.org/10.1051/swsc/2018020>

Pulupa, M., & Bale, S. D. (2008). Structure on Interplanetary Shock Fronts: Type II Radio Burst Source Regions. *The Astrophysical Journal*, 676 (2), 1330-1337.

<https://doi.org/10.1086/526405>

Reiner, M. J., Fainberg, J., Kaiser, M. L., & Stone, R. G. (1998). Type III Radio Source Located by Ulysses/Wind Triangulation. *Journal of Geophysical Research*, 103 (A2), 1923-1932. <https://doi.org/10.1029/97JA02646>

Reiner, M. J., Goetz, K., Fainberg, J., Kaiser, M. L., Maksimovic, M., Cecconi, B., Hoang, S., Bale, S. D., & Bougeret, J. -. (2009). Multipoint Observations of Solar Type III Radio Bursts from STEREO and Wind. *Solar Physics*, 259 (1-2), 255–276. <https://doi.org/10.1007/s11207-009-9404-z>

Reiss, M. A., Hofmeister, S. J., De Visscher, R., Temmer, M., Veronig, A. M., Delouille, V., Mampaey, B., & Ahammer, H. (2015). Improvements on coronal hole detection in SDO/AIA images using supervised classification. *Journal of Space Weather and Space Climate*, 5, Article A23, A23. <https://doi.org/10.1051/swsc/2015025>

Richardson, I. G., & Cane, H. V. (2010). Near-Earth Interplanetary Coronal Mass Ejections During Solar Cycle 23 (1996 - 2009): Catalog and Summary of Properties. *Solar Physics*, 264 (1), 189–237. <https://doi.org/10.1007/s11207-010-9568-6>

Riley, P., Lionello, R., Linker, J. A., Mikic, Z., Luhmann, J., & Wijaya, J. (2011). Global MHD Modeling of the Solar Corona and Inner Heliosphere for the Whole Heliosphere Interval. *Solar Physics*, 274 (1-2), 361–377. <https://doi.org/10.1007/s11207-010-9698-x>

Riley, P., Linker, J. A., & Arge, C. N. (2015). On the role played by magnetic expansion factor in the prediction of solar wind speed. *Space Weather*, 13 (3), 154–169. <https://doi.org/10.1002/2014SW001144>

Robinson, P. A., & Cairns, I. H. (2000). Theory of Type III And Type II Solar Radio Emissions. *Washington DC American Geophysical Union Geophysical Monograph Series*, 119, 37. <https://doi.org/10.1029/GM119p0037>

Rodriguez, L., Barnes, D., Hosteaux, S., Davies, J. A., Willems, S., Pant, V., Harrison, R. A., Berghmans, D., Bothmer, V., Eastwood, J. P., Gallagher, P. T., Kilpua, E. K. J., Magdalenic, J., Mierla, M., Möstl, C., Rouillard, A. P., Odstrčil, D., & Poedts, S. (2022). Comparing the Heliospheric Cataloging, Analysis, and Techniques Service (HELCASTS) Manual and Automatic Catalogues of Coronal Mass Ejections Using Solar Terrestrial Relations Observatory/Heliospheric Imager (STEREO/HI) Data. *Solar Physics*, 297 (2), Article 23, 23. <https://doi.org/10.1007/s11207-022-01959-w>

Rodriguez, L., Mierla, M., Zhukov, A. N., West, M., & Kilpua, E. (2011). Linking Remote-Sensing and In Situ Observations of Coronal Mass Ejections Using STEREO. *Solar Physics*, 270 (2), 561–573. <https://doi.org/10.1007/s11207-011-9784-8>

Rodriguez, L., Zhukov, A. N., Cid, C., Cerrato, Y., Saiz, E., Cremades, H., Dasso, S., Menvielle, M., Aran, A., Mandrini, C., Poedts, S., & Schmieder, B. (2009). Three frontside full halo coronal mass ejections with a nontypical geomagnetic response. *Space Weather*, 7 (6), Article S06003, S06003. <https://doi.org/10.1029/2008SW000453>

Rouillard, A. P., Davies, J. A., Forsyth, R. J., Rees, A., Davis, C. J., Harrison, R. A., Lockwood, M., Bewsher, D., Crothers, S. R., Eyles, C. J., Hapgood, M., & Perry, C. H. (2008). First imaging of corotating interaction regions using the STEREO spacecraft. *Geophysical Research Letters*, 35 (10), Article L10110, L10110. <https://doi.org/10.1029/2008GL033767>

Rouillard, A. P., Plotnikov, I., Pinto, R. F., Tirole, M., Lavarra, M., Zucca, P., Vainio, R., Tylka, A. J., Vourlidas, A., De Rosa, M. L., Linker, J., Warmuth, A., Mann, G., Cohen, C. M. S., & Mewaldt, R. A. (2016). Deriving the Properties of Coronal Pressure Fronts in 3D: Application to the 2012 May 17 Ground Level Enhancement. *The Astrophysical Journal*, 833 (1), Article 45, 45. <https://doi.org/10.3847/1538-4357/833/1/45>

Saito, K. (1970). A Non-Spherical Axisymmetric Model of the Solar K Corona of the Minimum Type. *Annals of the Tokyo Astronomical Observatory*, 12 (2), 51.

Samara, E., Laperre, B., Kieokaew, R., Temmer, M., Verbeke, C., Rodriguez, L., Magdalenic, J., & Poedts, S. (2022a). Dynamic Time Warping as a Means of Assessing Solar Wind Time Series. *The Astrophysical Journal*, 927 (2), Article 187, 187. <https://doi.org/10.3847/1538-4357/ac4af6>

Samara, E., Pinto, R. F., Magdalenic, J., Wijsen, N., Jerčić, V., Scolini, C., Jebaraj, I. C., Rodriguez, L., & Poedts, S. (2021). Implementing the MULTI-VP coronal model in EUHFORIA: Test case results and comparisons with the WSA coronal model. *Astronomy & Astrophysics*, 648, Article A35, A35. <https://doi.org/10.1051/0004-6361/202039325>

Samara, E., Magdalenic, J., Rodriguez, L., Heinemann, S. G., Georgoulis, M. K., Hofmeister, S. J., & Poedts, S. (2022b). Influence of coronal hole morphology on the solar wind speed at Earth. *arXiv e-prints*, Article arXiv:2204.00368, arXiv:2204.00368.

Schatten, K. H., Wilcox, J. M., & Ness, N. F. (1969). A model of interplanetary and coronal magnetic fields. *Solar Physics*, 6 (3), 442–455. <https://doi.org/10.1007/BF00146478>

Schwenn, R. (2006). Space Weather: The Solar Perspective. *Living Reviews in Solar Physics*, 3 (1), Article 2, 2. <https://doi.org/10.12942/lrsp-2006-2>

Scolini, C., Chané, E., Pomoell, J., Rodriguez, L., & Poedts, S. (2020a). Improving Predictions of High-Latitude Coronal Mass Ejections Throughout the Heliosphere. *Space Weather*, 18 (3), Article e02246, e02246. <https://doi.org/10.1029/2019SW002246>

Scolini, C., Dasso, S., Rodriguez, L., Zhukov, A. N., & Poedts, S. (2021a). Exploring the radial evolution of interplanetary coronal mass ejections using EUHFORIA. *Astronomy & Astrophysics*, 649, Article A69, A69. <https://doi.org/10.1051/0004-6361/202040226>

Scolini, C., Rodriguez, L., Mierla, M., Pomoell, J., & Poedts, S. (2019). Observation-based modelling of magnetised coronal mass ejections with EUHFORIA. *Astronomy & Astrophysics*, 626, Article A122, A122. <https://doi.org/10.1051/0004-6361/201935053>

Scolini, C., Chané, E., Temmer, M., Kilpua, E. K. J., Dissauer, K., Veronig, A. M., Palmerio, E., Pomoell, J., Dumbović, M., Guo, J., Rodriguez, L., & Poedts, S. (2020b). CME-CME Interactions as Sources of CME Geoeffectiveness: The Formation of the Complex Ejecta and Intense Geomagnetic Storm in 2017 Early September. *The Astrophysical Journal Supplement Series*, 247 (1), Article 21, 21. <https://doi.org/10.3847/1538-4365/ab6216>

Scolini, C., Winslow, R. M., Lugaz, N., & Poedts, S. (2021b). Evolution of Interplanetary Coronal Mass Ejection Complexity: A Numerical Study through a Swarm of Simulated Spacecraft. *The Astrophysical Journal Letters*, 916 (2), Article L15, L15. <https://doi.org/10.3847/2041-8213/ac0d58>

Shergelashvili, B. M., Philishvili, E., Buitendag, S., Poedts, S., & Khodachenko, M. (2022). Categorized model of moving small-scale intensity enhancements in solar active regions. *arXiv e-prints*, Article arXiv:2203.06285, arXiv:2203.06285.

Srivastava, N., & Venkatakrishnan, P. (2004). Solar and interplanetary sources of major geomagnetic storms during 1996-2002. *Journal of Geophysical Research (Space Physics)*, 109 (A10), Article A10103, A10103. <https://doi.org/10.1029/2003JA010175>

Street, A. G., Ball, L., & Melrose, D. B. (1994). Shock Drift Acceleration and Type II Solar Radio Bursts. *Astronomical Society of Australia, Proceedings*, 11 (1), 21-24. <https://doi.org/10.1017/S1323358000019603>

Talpeanu, D.-C., Poedts, S., D’Huys, E., Mierla, M., & Richardson, I. G. (2022). Interaction of coronal mass ejections and the solar wind. A force analysis. *arXiv e-prints*, Article arXiv:2203.09393, arXiv:2203.09393.

Temmer, M., & Nitta, N. V. (2015). Interplanetary Propagation Behavior of the Fast Coronal Mass Ejection on 23 July 2012. *Solar Physics*, 290 (3), 919–932.

<https://doi.org/10.1007/s11207-014-0642-3>

Temmer, M., Rollett, T., Möstl, C., Veronig, A. M., Vršnak, B., & Odstrčil, D. (2011). Influence of the Ambient Solar Wind Flow on the Propagation Behavior of Interplanetary Coronal Mass Ejections. *The Astrophysical Journal*, 743 (2), Article 101, 101. <https://doi.org/10.1088/0004-637X/743/2/101>

Thejappa, G., MacDowall, R. J., & Bergamo, M. (2012). In situ detection of strong Langmuir turbulence processes in solar type III radio bursts. *Journal of Geophysical Research (Space Physics)*, 117 (A8), Article A08111, A08111. <https://doi.org/10.1029/2012JA017695>

Thernisien, A., Vourlidas, A., & Howard, R. A. (2009). Forward Modeling of Coronal Mass Ejections Using STEREO/SECCHI Data. *Solar Physics*, 256 (1-2), 111–130.

<https://doi.org/10.1007/s11207-009-9346-5>

Thernisien, A. F. R., Howard, R. A., & Vourlidas, A. (2006). Modeling of Flux Rope Coronal Mass Ejections. *The Astrophysical Journal*, 652 (1), 763–773. <https://doi.org/10.1086/508254>

Vennerstrom, S., Lefevre, L., Dumbović, M., Crosby, N., Malandraki, O., Patsou, I., Clette, F., Veronig, A., Vršnak, B., Leer, K., & Moretto, T. (2016). Extreme Geomagnetic Storms - 1868 - 2010. *Solar Physics*, 291 (5), 1447–1481. <https://doi.org/10.1007/s11207-016-0897-y>

Venzmer, M. S., & Bothmer, V. (2018). Solar-wind predictions for the Parker Solar Probe orbit. Near-Sun extrapolations derived from an empirical solar-wind model based on Helios and OMNI observations. *Astronomy and Astrophysics*, 611, Article A36, A36. <https://doi.org/10.1051/0004-6361/201731831>

Verbeke, C., Pomoell, J., & Poedts, S. (2019). The evolution of coronal mass ejections in the inner heliosphere: Implementing the spheromak model with EUHFORIA. *Astronomy and Astrophysics*, 627, Article A111, A111. <https://doi.org/10.1051/0004-6361/201834702>

Vorotnikov, V. S., Smith, C. W., Hu, Q., Szabo, A., Skoug, R. M., & Cohen, C. M. S. (2008). Automated shock detection and analysis algorithm for space weather application. *Space Weather*, 6 (3), 03002. <https://doi.org/10.1029/2007SW000358>

Vršnak, B., Aurass, H., Magdalenic, J., & Gopalswamy, N. (2001). Band-splitting of coronal and interplanetary type II bursts. I. Basic properties. *Astronomy and Astrophysics*, 377, 321–329. <https://doi.org/10.1051/0004-6361:20011067>

Vršnak, B., Magdalenic, J., & Zlobec, P. (2004). Band-splitting of coronal and interplanetary type II bursts. III. Physical conditions in the upper corona and interplanetary space. *Astronomy and Astrophysics*, 413, 753–763. <https://doi.org/10.1051/0004-6361:20034060>

Vršnak, B., Warmuth, A., Temmer, M., Veronig, A., Magdalenic, J., Hillaris, A., & Karlický, M. (2006). Multi-wavelength study of coronal waves associated with the CME-flare event of 3 November 2003. *Astronomy and Astrophysics*, 448 (2), 739-752. <https://doi.org/10.1051/0004-6361:20053740>

Vršnak, B., Žic, T., Falkenberg, T. V., Möstl, C., Vennerstrom, S., & Vrbanec, D. (2010). The role of aerodynamic drag in propagation of interplanetary coronal mass ejections. *Astronomy and Astrophysics*, 512, Article A43, A43. <https://doi.org/10.1051/0004-6361/200913482>

Vršnak, B., Temmer, M., & Veronig, A. M. (2007). Coronal Holes and Solar Wind High-Speed Streams:

I. Forecasting the Solar Wind Parameters. *Solar Physics*, 240 (2), 315–330. <https://doi.org/10.1007/s11207-007-0285-8>

Wagner, A., Asvestari, E., Temmer, M., Heinemann, S. G., & Pomoell, J. (2022). Validation scheme for solar coronal models: Constraints from multi-perspective observations in EUV and white light. *Astronomy & Astrophysics*, 657, Article A117, A117. <https://doi.org/10.1051/0004-6361/202141552>

Wang, Y. M., Ye, P. Z., Wang, S., Zhou, G. P., & Wang, J. X. (2002). A statistical study on the geoeffectiveness of Earth-directed coronal mass ejections from March 1997 to December 2000. *Journal of Geophysical Research (Space Physics)*, 107 (A11), Article 1340, 1340. <https://doi.org/10.1029/2002JA009244>

Wang, Y., Shen, C., Wang, S., & Ye, P. (2004). Deflection of coronal mass ejection in the interplanetary medium. *Solar Physics*, 222 (2), 329–343.

<https://doi.org/10.1023/B:SOLA.0000043576.21942.aa>

Warmuth, A., Vršnak, B., Magdalenić, J., Hanslmeier, A., & Otruba, W. (2004). A multiwavelength study of solar flare waves. I. Observations and basic properties. *Astronomy and Astrophysics*, 418 (3), 1101-1115. <https://doi.org/10.1051/0004-6361:20034332>

Wiegmann, T., Petrie, G. J. D., & Riley, P. (2017). Coronal Magnetic Field Models. *Space Science Reviews*, 210 (1-4), 249–274. <https://doi.org/10.1007/s11214-015-0178-3>

Wiegmann, T., Thalmann, J. K., & Solanki, S. K. (2014). The magnetic field in the solar atmosphere. *The Astronomy and Astrophysics Review*, 22, Article 78, 78. <https://doi.org/10.1007/s00159-014-0078-7>

Wild, J. P., & McCready, L. L. (1950). Observations of the Spectrum of High-Intensity Solar Radiation at Metre Wavelengths. I. The Apparatus and Spectral Types of Solar Burst Observed. *Australian Journal of Scientific Research A*, 3 (3), 387 - 398. <https://doi.org/10.1071/CH9500387>

Yordanova, E., Dumbovic, M., Temmer, M., Scolini, C., Magdalenić, J., Thompson, W. J., Sorriso-Valvo, L., Dimmock, A. P., & Rosenqvist, L. (2021). Comparative study of halo CME arrival predictions. *EGU General Assembly Conference Abstracts*, Article EGU21-14187, EGU21–14187. <https://doi.org/10.5194/egusphere-egu21-14187>

Zhang, J., Dere, K. P., Howard, R. A., & Bothmer, V. (2003). Identification of Solar Sources of Major Geomagnetic Storms between 1996 and 2000. *The Astrophysical Journal*, 582 (1), 520–533. <https://doi.org/10.1086/344611>

Zhang, P., Zucca, P., Sridhar, S. S., Wang, C., Bisi, M. M., Dabrowski, B., Krankowski, A., Mann, G., Magdalenić, J., Morosan, D. E., & Vocks, C. (2020). Interferometric imaging with LOFAR remote baselines of the fine structures of a solar type-IIIb radio burst. *Astronomy & Astrophysics*, 639, Article A115, A115. <https://doi.org/10.1051/0004-6361/202037733>

Zhukov, A. N., & Auchère, F. (2004). On the nature of EIT waves, EUV dimmings and their link to CMEs. *Astronomy and Astrophysics*, 427 (2), 705-716. <https://doi.10.1051/0004-6361:20040351>

Zucca, P., Morosan, D. E., Rouillard, A. P., Fallows, R., Gallagher, P. T., Magdalenić, J., Klein, K.-L., Mann, G., Vocks, C., Carley, E. P., Bisi, M. M., Kontar, E. P., Rothkaehl, H., Dabrowski, B., Krankowski, A., Anderson, J., Asgekar, A., Bell, M. E., Bentum, M. J., Best, P., Blaauw, R., Breitling, F., Zarka, P. (2018). Shock location and CME 3D reconstruction of a solar type II radio burst with LOFAR. *Astronomy & Astrophysics*, 615, Article A89, A89. <https://doi.org/10.1051/0004-6361/201732308>

Zuccarello, F. P., Bemporad, A., Jacobs, C., Mierla, M., Poedts, S., & Zuccarello, F. (2012). The Role of Streamers in the Deflection of Coronal Mass Ejections: Comparison between STEREO Three-dimensional Reconstructions and Numerical Simulations. *The Astrophysical Journal*, 744 (1), Article 66, 66. <https://doi.org/10.1088/0004-637X/744/1/66>

5. DISSEMINATION AND VALORISATION

The Dissemination and valorisation of the project results was focused to presenting the project products (e.g. lists of events studied and modelled in the CCSOM is presently used in the H2020 project EUHFORIA2.0, modelling results of specific time intervals) and science to external scientists and the users (e.g. space weather forecasting centres, satellite operators, etc.).

Within the project dissemination we have:

- Set up dedicated EUHFORIA project website with information about EUHFORIA, list of events used to validate models, etc.
- Contributed to the STCE (Solar Terrestrial Centre of Excellence) Newsletter when the milestones or some other exciting result was obtained,
- We provided the support to the EUHFORIA consortium members to present project results at conferences and workshops.

In the framework of the CCSOM project significant number of invited talks, presentations and posters was presented at different international conferences.

The studies that were conducted in the framework of CCSOM were presented, by project members, at all together around 50 invited talks and lectures and around 70 oral and poster presentations at different international conferences.

We list here some of the conferences at which the CCSOM project work was presented:

- EGU General Assembly: EGU 2018, 2019, 2020, 2021,2022
- Exploiting magnetograms in preparation for Solar Orbiter and Parker Solar Probe; MADAWG meeting, 2018
- European Space Weather Week: ESWW14 in 2017, ESWW15 in 2018, ESWW16 in 2019, ESWW17 in 2020, ESWW18 in 2021.
- European Solar Physics Meeting: ESPM 15 in 2017, ESPM 16 in 2021
- Numerical techniques in MHD simulations, 2017
- FLARECAST science workshop Observatoire de Paris, 2017
- Solar Wind 15, 2018
- The 45th European Physical Society Conference on Plasma Physics, 2018
- The 2nd China-Europe Solar Physics Meeting – CESPM, 2019
- The 5th Asia-Pacific Conference on Plasma Physics, e-Conference, 2021.
- The Royal Astronomical Society Specialist Discussion Meetings, 2022

Together with the biweekly teleconferences of all partners, weekly meetings of some project members were taking place when needed Every 6 to 7 month the CCSOM project meetings, held in-person, were organized. The meetings usually lasted 1-2 days and they were mostly taking place after the international conferences in which project members were participating. The follow-up committee members were occasionally participating in the regular teleconferences, and in several occasions also at the in-person meetings.

6. PUBLICATIONS

Direct output of the project were also more than 40 scientific publications in the refereed journals.

List of publications of the CCSOM project:

1. Asvestari, E., Heinemann, S. G., Temmer, M., Pomoell, J., Kilpua, E., Magdalenic, J., & Poedts, S. (2019), Reconstructing Coronal Hole Areas With EUHFORIA and Adapted WSA Model: Optimizing the Model Parameters., *Journal of Geophysical Research: Space Physics*, Volume 124, Issue 11, pp. 8280-829, <https://doi.org/10.1029/2019JA027173>
2. Hinterreiter, J., Magdalenic, J., Temmer, M., Verbeke, C., Jebaraj, I. C., Samara, E., Asvestari, E., Poedts, S., Pomoell, J., Kilpua, E., Rodriguez, L., Scolini, C., & Isavnin, A. (2019). Assessing the Performance of EUHFORIA Modeling the Background Solar Wind., *Solar Physics*, Volume 294, Issue 12, id.170, <https://doi.org/10.1007/s11207-019-1558-8>
3. Kilpua, E. K. J., Good, S. W., Palmerio, E., Asvestari, E., Lumme, E., Ala-Lahti, M., Kalliokoski, M. M. H., Morosan, D. E., Pomoell, J., Price, D. J., Magdalenic, J., Poedts, S., & Futaana, Y. (2019). Multipoint Observations of the June 2012 Interacting Interplanetary Flux Ropes., *Frontiers in Astronomy and Space Sciences*, Volume 6, id.50 <https://doi.org/10.3389/fspas.2019.00050>
4. Palmerio, E., Scolini, C., Barnes, D., Magdalenic, J., West, M. J., Zhukov, A. N., Rodriguez, L., Mierla, M., Good, S. W., Morosan, D. E., Kilpua, E. K. J., Pomoell, J., & Poedts, S. (2019)., Multipoint Study of Successive Coronal Mass Ejections Driving Moderate Disturbances at 1 au., *The Astrophysical Journal*, Volume 878, Issue 1, article id. 37, 15 pp. <https://doi.org/10.3847/1538-4357/ab1850>
5. Scolini, C., Rodriguez, L., Mierla, M., Pomoell, J., & Poedts, S. (2019)., Observation-based modelling of magnetised coronal mass ejections with EUHFORIA., *Astronomy & Astrophysics*, Volume 626, id.A122, 25 pp. <https://doi.org/10.1051/0004-6361/201935053>
6. Verbeke, C., Pomoell, J., & Poedts, S. (2019)., The evolution of coronal mass ejections in the inner heliosphere: Implementing the spheromak model with EUHFORIA., *Astronomy & Astrophysics*, Volume 627, id.A111, 15 pp. <https://doi.org/10.1051/0004-6361/201834702>
7. Hofmeister, S. J., Veronig, A. M., Poedts, S., Samara, E., & Magdalenic, J. (2020)., On the Dependency between the Peak Velocity of High-speed Solar Wind Streams near Earth and the Area of Their Solar Source Coronal Holes., 897 (1), *The Astrophysical Journal Letters*, Volume 897, Issue 1, id.L17 <https://doi.org/10.3847/2041-8213/ab9d19>

8. Jebaraj, I. C., Magdaleníć, J., Podladchikova, T., Scolini, C., Pomoell, J., Veronig, A. M., Dissauer, K., Krupar, V., Kilpua, E. K. J., & Poedts, S. (2020). Using radio triangulation to understand the origin of two subsequent type II radio bursts., *639, Astronomy & Astrophysics, Volume 639, id.A56, 16 pp.*
<https://doi.org/10.1051/0004-6361/201937273>
9. Magdaleníć, J., Marque, C., Fallows, R. A., Mann, G., Vocks, C., Zucca, P., Dabrowski, B. P., Krankowski, A., & Melnik, V. (2020)., Fine Structure of a Solar Type II Radio Burst Observed by LOFAR., *The Astrophysical Journal Letters, Volume 897, Issue 1, id.L15, 8 pp.*
<https://doi.org/10.3847/2041-8213/ab9abc>
10. Millas, D., Innocenti, M. E., Laperre, B., Raeder, J., Poedts, S., & Lapenta, G. (2020)., Domain of Influence analysis: implications for Data Assimilation in space weather forecasting., *Frontiers in Astronomy and Space Sciences, 7, id.73.*
<https://doi.org/10.3389/fspas.2020.571286>
11. Morosan, D. E., Palmerio, E., Rasanen, J. E., Kilpua, E. K. J., Magdaleníć, J., Lynch, B. J., Kumari, A., Pomoell, J., & Palmroth, M. (2020)., Electron acceleration and radio emission following the early interaction of two coronal mass ejections., *Astronomy & Astrophysics, Volume 642, id.A151, 13 pp.*
<https://doi.org/10.1051/0004-6361/202038801>
12. Pick, M., Magdaleníć, J., Cornilleau-Wehrlin, N., Grison, B., Schmieder, B., & Bocchialini, K. (2020). Role of the Coronal Environment in the Formation of Four Shocks Observed without Coronal Mass Ejections at Earth's Lagrangian Point L1., *The Astrophysical Journal, Volume 895, Issue 2, id.144, 15 pp.*
<https://doi.org/10.3847/1538-4357/ab8fae>
13. Poedts, S., Kochanov, A., Lani, A., Scolini, C., Verbeke, C., Hosteaux, S., Chan' e, E., Deconinck, H., Mihalache, N., Diet, F., Heynderickx, D., De Keyser, J., De Donder, E., Crosby, N. B., Echim, M., Rodriguez, L., Vansintjan, R., Verstringe, F., Mampaey, B., Luntama, J.-P. (2020a)., The Virtual Space Weather Modelling Centre., *Journal of Space Weather and Space Climate, Volume 10, id.14, 23 pp.*
<https://doi.org/10.1051/swsc/2020012>
14. Poedts, S., Lani, A., Scolini, C., Verbeke, C., Wijssen, N., Lapenta, G., Laperre, B., Millas, D., Innocenti, M. E., Chane, E., Baratashvili, T., Samara, E., Van der Linden, R., Rodriguez, L., Vanlommel, P., Vainio, R., Afanasiev, A., Kilpua, E., Pomoell, J., Depauw, J. (2020b)., EUropean Heliospheric FORecasting Information Asset 2.0., *Journal of Space Weather and Space Climate, Volume 10, id.57, 14 pp.*
<https://doi.org/10.1051/swsc/2020055>

15. Scolini, C., Chane, E., Pomoell, J., Rodriguez, L., & Poedts, S. (2020a)., Improving Predictions of High-Latitude Coronal Mass Ejections Throughout the Heliosphere., *Space Weather, Volume 18, Issue 3, article id. e02246*
<https://doi.org/10.1029/2019SW002246>
16. Scolini, C., Chane, E., Temmer, M., Kilpua, E. K. J., Dissauer, K., Veronig, A. M., Palmerio, E., Pomoell, J., Dumbovic, M., Guo, J., Rodriguez, L., & Poedts, S. (2020b)., CME-CME Interactions as Sources of CME Geoeffectiveness: The Formation of the Complex Ejecta and Intense Geomagnetic Storm in 2017 Early September., *The Astrophysical Journal Supplement Series, Volume 247, Issue 1, id.21, 27 pp.*
<https://doi.org/10.3847/1538-4365/ab6216>
17. Zhang, P., Zucca, P., Sridhar, S. S., Wang, C., Bisi, M. M., Dabrowski, B., Krankowski, A., Mann, G., Magdalenic, J., Morosan, D. E., & Vocks, C. (2020)., Interferometric imaging with LOFAR remote baselines of the fine structures of a solar type-IIIb radio burst., *Astronomy & Astrophysics, Volume 639, id.A115, 5 pp.*
<https://doi.org/10.1051/0004-6361/202037733>
18. Asvestari, E., Pomoell, J., Kilpua, E., Good, S., Chatzistergos, T., Temmer, M., Palmerio, E., Poedts, S., & Magdalenic, J. (2021)., Modelling a multi-spacecraft coronal mass ejection encounter with EUHFORIA., *Astronomy & Astrophysics, Volume 652, id.A27, 18 pp.*
<https://doi.org/10.1051/0004-6361/202140315>
19. Chane, E., Schmieder, B., Dasso, S., Verbeke, C., Grison, B., Demoulin, P., & Poedts, S. (2021)., Overexpansion of a coronal mass ejection generates sub-Alfvénic plasma conditions in the solar wind at Earth., *Astronomy & Astrophysics, Volume 647, id.A149, 12 pp.*
<https://doi.org/10.1051/0004-6361/202039867>
20. Hosteaux, S., Chane, E., & Poedts, S. (2021)., Analysis of Deformation and Erosion during CME Evolution., *Geosciences, The Special Issue Latest Advances in Space Weather Research, 11 (8), 314.*
<https://doi.org/10.3390/geosciences11080314>
21. Husidic, E., Lazar, M., Fichtner, H., Scherer, K., & Poedts, S. (2021)., Transport coefficients enhanced by suprathermal particles in nonequilibrium heliospheric plasmas., *Astronomy & Astrophysics, Volume 654, id.A99, 10 pp.*
<https://doi.org/10.1051/0004-6361/202141760>
22. Jebaraj, I. C., Kouloumvakos, A., Magdalenic, J., Rouillard, A. P., Mann, G., Krupar, V., & Poedts, S. (2021)., Generation of interplanetary type II radio emission.,

- Astronomy & Astrophysics, Volume 654, id.A64, 15 pp.
<https://doi.org/10.1051/0004-6361/202141695>
23. Kouloumvakos, A., Rouillard, A., Warmuth, A., Magdalenić, J., Jebaraj, I. C., Mann, G., Vainio, R., & Monstein, C. (2021)., Coronal Conditions for the Occurrence of Type II Radio Bursts., *The Astrophysical Journal*, Volume 913, Issue 2, id.99, 12 pp.
<https://doi.org/10.3847/1538-4357/abf435>
24. Niedziela, R., Murawski, K., & Poedts, S. (2021)., Chromospheric heating and generation of plasma outflows by impulsively generated two-fluid magnetoacoustic waves., *Astronomy & Astrophysics*, Volume 652, id.A124, 10 pp.
<https://doi.org/10.1051/0004-6361/202141027>
25. Pelekhata, M., Murawski, K., & Poedts, S. (2021)., Solar chromosphere heating and generation of plasma outflows by impulsively generated two-fluid Alfvén waves., *Astronomy & Astrophysics*, Volume 652, id.A114, 8 pp.
<https://doi.org/10.1051/0004-6361/202141262>
26. Samara, E., Pinto, R. F., Magdalenić, J., Wijsen, N., Jercic, V., Scolini, C., Jebaraj, I. C., Rodriguez, L., & Poedts, S. (2021)., Implementing the MULTI-VP coronal model in EUHFORIA: Test case results and comparisons with the WSA coronal model., *Astronomy & Astrophysics*, Volume 648, id.A35, 15 pp.
<https://doi.org/10.1051/0004-6361/202039325>
27. Scolini, C., Winslow, R. M., Lugaz, N., & Poedts, S. (2021)., Evolution of Interplanetary Coronal Mass Ejection Complexity: A Numerical Study through a Swarm of Simulated Spacecraft., *The Astrophysical Journal Letters*, Volume 916, Issue 2, id.L15, 14 pp.
<https://doi.org/10.3847/2041-8213/ac0d58>
28. Shaaban, S. M., Lazar, M., Lopez, R. A., Yoon, P. H., & Poedts, S. (2021)., Advanced Interpretation of Waves and Instabilities in Space Plasmas. In M. Lazar & H. Fichtner (Eds.), *Kappa distributions; from observational evidences via controversial predictions to a consistent theory of nonequilibrium plasmas* (pp. 185–218).
https://doi.org/10.1007/978-3-030-82623-9_10
29. Brchnelova, M., Zhang, F., Leitner, P., Perri, B., Lani, A., & Poedts, S. (2022)., Effects of mesh topology on MHD solution features in coronal simulations., *Journal of Plasma Physics*, Volume 88, Issue 2, article id.905880205
<https://doi.org/10.1017/S0022377822000241>

30. Husidic, E., Scherer, K., Lazar, M., Fichtner, H., & Poedts, S. (2022). Toward a Realistic Evaluation of Transport Coefficients in Non-equilibrium Space Plasmas., *The Astrophysical Journal, Volume 927, Issue 2, id.159, 10 pp.*
<https://doi.org/10.3847/1538-4357/ac4af4>
31. Mann, G., Vocks, C., Warmuth, A., Magdalenic, J., Bisi, M., Carley, E., Dabrowski, B., Gallagher, P., Krankowski, A., Matyjasiak, B., Rotkaehl, H., & Zucca, P. (2022). Excitation of Langmuir waves at shocks and solar type II radio bursts., *Astronomy & Astrophysics, Volume 660, id.A71, 8 pp.*
<https://doi.org/10.1051/0004-6361/202142201>
32. Rodriguez, L., Barnes, D., Hosteaux, S., Davies, J. A., Willems, S., Pant, V., Harrison, R. A., Berghmans, D., Bothmer, V., Eastwood, J. P., Gallagher, P. T., Kilpua, E. K. J., Magdalenic, J., Mierla, M., Mostl, C., Rouillard, A. P., Odstrcil, D., & Poedts, S. (2022)., Comparing the Helio- spheric Cataloging, Analysis, and Techniques Service (HELCATS) Manual and Automatic Catalogues of Coronal Mass Ejections Using Solar Terrestrial Relations Observatory/Heliospheric Imager (STEREO/HI) Data., *Solar Physics, Volume 297, Issue 2, article id.23*
<https://doi.org/10.1007/s11207-022- 01959-w>
33. Samara, E., Laperre, B., Kieokaew, R., Temmer, M., Verbeke, C., Rodriguez, L., Magdalenic, J., & Poedts, S. (2022a)., Dynamic Time Warping as a Means of Assessing Solar Wind Time Series., *The Astrophysical Journal, Volume 927, Issue 2, id.187, 19 pp.*
<https://doi.org/10.3847/1538-4357/ac4af6>
34. Samara, E., Magdalenic, J., Rodriguez, L., Heinemann, S. G., Georgoulis, M. K., Hofmeister, S. J., & Poedts, S. (2022b)., Influence of coronal hole morphology on the solar wind speed at Earth., *Astronomy & Astrophysics, Volume 662, id.A68, 19 pp.* [10.1051/0004-6361/202142793](https://doi.org/10.1051/0004-6361/202142793)
35. Shergelashvili, B. M., Philishvili, E., Buitendag, S., Poedts, S., & Khodachenko, M. (2022)., Categorization model of moving small-scale intensity enhancements in solar active regions., *Astronomy & Astrophysics, Volume 662, id.A30, 10 pp.*
[10.1051/0004-6361/202142547](https://doi.org/10.1051/0004-6361/202142547)
36. Verbeke, C., Baratashvili, T., & Poedts, S. (2022). ICARUS, a new inner heliospheric model with a flexible grid., *Astronomy & Astrophysics, Volume 662, id.A50, 11 pp.*
<https://doi.org/10.1051/0004-6361/202141981>
37. Wagner, A., Asvestari, E., Temmer, M., Heinemann, S. G., & Pomoell, J. (2022)., Validation scheme for solar coronal models: Constraints from multi-perspective observations in EUV and white light., *Astronomy & Astrophysics, Volume 657, id.A117, 12 pp.*
<https://doi.org/10.1051/0004-6361/202141552>

38. osteaux, S., Rodriguez, L., Poedts, S., (2022)., Analysis of Voyager 1 and Voyager 2 in situ CME observations, *Advances in Space Research*, in press
<https://doi.org/10.1016/j.asr.2022.03.005>
39. Talpeanu, D. C., Poedts, S., D’Huys, E., Mierla, M., & Richardson, I. G. (2022)., Interaction of coronal mass ejections and the solar wind. A force analysis., *Astronomy & Astrophysics*, in press,
<https://doi.org/10.1051/0004-6361/202243150>
40. Verbeke, C., Schmieder, B., Démoulin, P., Dasso, S., Grison, B., Samara, E., Scolini, C. Poedts, S. (2022)., Over-expansion of coronal mass ejections modelled using 3D MHD EUHFORIA simulations, *Advances in Space Research*, in press,
<https://doi.org/10.1016/j.asr.2022.06.013>
41. Maharana, A., Isavnin, A., Scolini, C., Wijzen, N., Rodriguez, L., Mierla, M., Magdalenic, J., Poedts, S. (2022)., Implementation and validation of the FRi3D flux rope model in EUHFORIA, *Advances in Space Research*, in press,
<https://doi.org/10.1016/j.asr.2022.05.056>
42. Perri, B., Leitner, P., Brchneľova, M., Baratashvili, T., Kuźma, B., Zhang, F., Lani, A., Poedts, S., (2022)., COCONUT, a novel fast-converging MHD model for solar corona simulations: I. Benchmarking and optimization of polytropic solutions, *Astrophysical Journal*, in press

7. ACKNOWLEDGEMENTS

The follow-up committee of CCSOM was composed of four scientists. Dr Consuelo Cid (University of Alcala, Spain), Prof. Richard Harrison and Dr Jackie Davies (STFC Rutherford Appleton Laboratory, UK) and Dr Bojan Vršnak (Hvar Observatory, Croatia). In particular, Dr Bojan Vršnak and Dr Consuelo Cid were participating on some of the project meetings and provided valuable comments and suggestions on how to improve the studies that were done in the framework of the CCSOM. Additionally, several other scientists participated in the CCSOM related studies, as can be visible from the project publication. Dr Rui Pinto provided a lot of assistance in implementation of the MULTI-VP model in EUHFORIA, and he also joined to one of the in-person project meetings.